

AD-A101 173

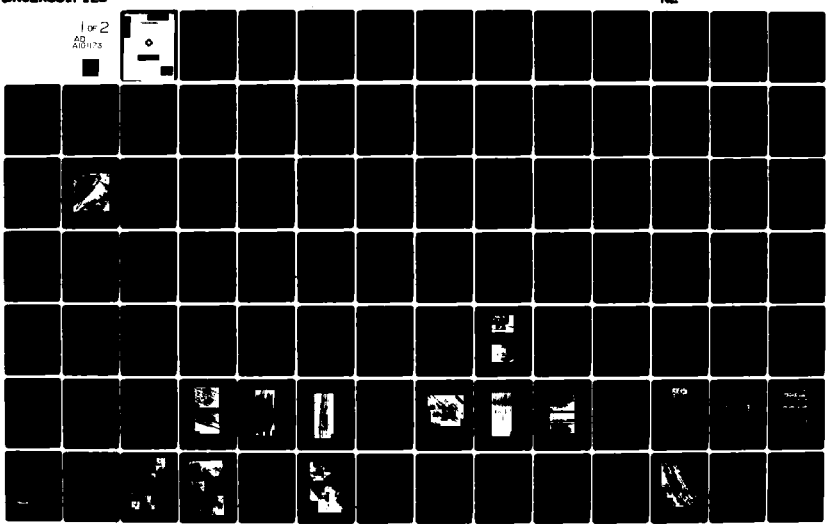
MASSACHUSETTS INST OF TECH CAMBRIDGE LAB FOR MFG AND ETC F/8 11/6
THE EFFECTS OF ION IMPLANTATION ON FRICTION AND WEAR OF METALS.(U)
MAY 81 N P SUN, S R SHEPARD

NO0014-80-C-0255

ML

UNCLASSIFIED

1 of 2
AD
A10173



AD-A169116

LEL

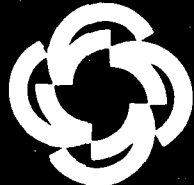
Ch

**The Effects of Ion Implantation
on Friction and Wear of Metals**

Progress Report to
The Office of Naval Research

Contract No. N00014-80-C-0255

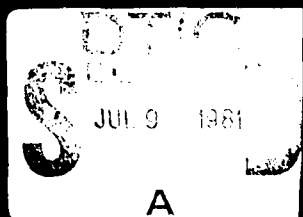
Nam P. Suh
Sharon R. Shepard



This document has been approved
for public release and sale. Its
distribution is unlimited.

Laboratory for Manufacturing and Productivity
School of Engineering
Massachusetts Institute of Technology
Cambridge, Massachusetts 02139

May 1981



THE EFFECTS OF ION IMPLANTATION
ON FRICTION AND WEAR OF METALS

Progress Report

to

The Office of Naval Research
Contract No. N00014-80-C-0255

Nam P. Suh

Sharon R. Shepard

Laboratory for Manufacturing and Productivity
School of Engineering
Massachusetts Institute of Technology
Cambridge, Massachusetts 02139

May 1981

Reproduction in whole or in part is
permitted for any purpose of the
United States Government

Approved for public release; distribution unlimited.

unclassified

SECURITY CLASSIFICATION OF THIS PAGE (When Data Entered)

REPORT DOCUMENTATION PAGE		READ INSTRUCTIONS BEFORE COMPLETING FORM
1. REPORT NUMBER 10	2. GOVT ACCESSION NO. 15 AD-A101173	3. RECIPIENT'S CATALOG NUMBER ----
4. TITLE (and Subtitle) 10 THE EFFECTS OF ION IMPLANTATION ON FRICTION AND WEAR OF METALS.	5. TYPE OF REPORT & PERIOD COVERED F Jan 1980 - Apr 1981	6. PERFORMING ORG. REPORT NUMBER ----
7. AUTHOR(s) 10 Nam P. Suh and Sharon R. Shepard	8. CONTRACT OR GRANT NUMBER(s) 15 N00014-80-C-0255	9. PERFORMING ORGANIZATION NAME AND ADDRESS Laboratory for Manufacturing and Productivity Massachusetts Institute of Technology 77 Massachusetts Avenue Cambridge, MA 02139
10. CONTROLLING OFFICE NAME AND ADDRESS Department of the Navy Office of Naval Research Arlington, Virginia 22217	11. REPORT DATE 15 May 1981	10. PROGRAM ELEMENT, PROJECT, TASK AREA & WORK UNIT NUMBERS ----
12. MONITORING AGENCY NAME & ADDRESS (if different from Controlling Office) Office of Naval Research M.I.T. Resident Representative Room E19-628 Cambridge, MA 02139	13. NUMBER OF PAGES 15	14. SECURITY CLASS. (of this report) unclassified
		15a. DECLASSIFICATION DOWNGRADING SCHEDULE ----
16. DISTRIBUTION STATEMENT (of this Report) unlimited	17. This document has been approved for public release and sale; its distribution is unlimited.	
18. SUPPLEMENTARY NOTES ----	19. KEY WORDS (Continue on reverse side if necessary and identify by block number) ion implantation, plowing, subsurface deformation, delamination wear, friction, stress distribution, asperity	
20. ABSTRACT (Continue on reverse side if necessary and identify by block number) The effect of ion implantation on the friction and wear behavior of metals was investigated. Experiments were conducted with iron, titanium, and copper implanted with nitrogen ions, iron implanted with aluminum ions, and copper implanted with zinc ions. The significant reduction in friction and wear of the iron and titanium systems is attributed to a hard layer formed during the ion implantation process. This hard layer minimizes plowing and subsurface deformation and hence reduces the delamination.		

410877

unclassified

SECURITY CLASSIFICATION OF THIS PAGE (When Data Entered)

(block 20 continued)

wear process, i.e. crack nucleation, crack propagation, and the formation of delamination wear sheets.

A finite element model of an elastic semi-infinite solid under the contact of a stationary rigid asperity showed that the hard layer does not change the subsurface stress distribution by supporting the load, but rather that this thin layer decreases the plowing component of friction. The model predicts that this decrease in the friction coefficient in turn, substantially reduces subsurface deformation and thus wear.

The implanted copper specimens which did not appear to have a hard surface layer showed little improvement in their tribological behavior over the unimplanted copper. N^+ implanted into iron was compared with ion nitrided iron. Under dry sliding conditions with high loads ion nitriding appears to be superior to ion implantation. However, at lower loads and under lubricated conditions ion implantation is more advantageous due to its superior surface finish.

unclassified

SECURITY CLASSIFICATION OF THIS PAGE (When Data Entered)

THE EFFECTS OF ION IMPLANTATION ON
FRICTION AND WEAR OF METALS

ABSTRACT

The effect of ion implantation on the friction and wear behavior of metals was investigated. Experiments were conducted with iron, titanium, and copper implanted with nitrogen ions, iron implanted with aluminum ions, and copper implanted with zinc ions. The significant reduction in friction and wear of the iron and titanium systems is attributed to a hard layer formed during the ion implantation process. This hard layer minimizes plowing and subsurface deformation and hence reduces the delamination wear process, i.e. crack nucleation, crack propagation, and the formation of delamination wear sheets.

A finite element model of an elastic semi-infinite solid under the contact of a stationary rigid asperity showed that the hard layer does not change the subsurface stress distribution by supporting the load, but rather that this thin layer decreases the plowing component of friction. The model predicts that this decrease in the friction coefficient in turn, substantially reduces subsurface deformation and thus wear.

The implanted copper specimens which did not appear to have a hard surface layer showed little improvement in their tribological behavior over the unimplanted copper. N^+ implanted into iron was compared with ion nitrided iron. Under dry sliding conditions with high loads ion nitriding appears to be superior to ion implantation. However, at lower loads and under lubricated conditions ion implantation is more advantageous due to its superior surface finish.

Accession No.	
NETS GRAIL	<input checked="" type="checkbox"/>
REF TAB	<input type="checkbox"/>
Unannounced	<input type="checkbox"/>
Identification	
Classification	
Availability Code	
Author and/or Editor	
Date	

A

ACKNOWLEDGEMENTS

This work was supported by the Office of Naval Research. We would like to express our appreciation to Commander Harold P. Martin for his personal support of this work.

Also, various people from both industry and the government have been very helpful. In particular, we would like to thank Dr. James Hirvonen and Dr. Irwin Singer, from NRL; Joe Aliprando, from General Electric; Mike Feralli, from Lord Corporation; Mr. Vernon Westcott, from Foxboro/Trans-Sonics Inc.; and Dr. Don Potter, from the University of Connecticut.

TABLE OF CONTENTS

<u>Chapter</u>		<u>Page Number</u>
	Title Page	1
	Abstract	2
	Acknowledgements	4
	Table of Contents	7
	List of Figures	9
	List of Tables	16
1.	Introduction	17
2.	Friction and Wear Theories	22
2.1	Adhesive Wear	22
2.2	Delamination Theory of Wear	25
2.3	Theories of Friction	30
3.	Ion Implantation	35
3.1	Range Calculations	35
3.2	Ion Implantation Equipment	40
3.3	Benefits and Drawbacks	43
3.4	Literature Survey	47
3.4.1	Friction	47
3.4.2	Wear	52
3.4.3	Hardness	55
3.4.4	Concluding Remarks	58
4.	Friction and Wear of Ion-Implanted Metals	60
4.1	Experimental Procedure	60
4.1.1	Sample Preparation	60
4.1.2	Ion Implantation	61
4.1.3	Friction and Wear Measurements	62
4.2	Experimental Results	64
4.2.1	Wear	68
4.2.2	Subsurface Deformation	79
4.2.3	Chemical Analysis of the Al ⁺ Implanted Iron Surface	87

<u>Chapter</u>		<u>Page Number</u>
5.	Hypothesized Mechanisms of Friction and Wear of Metals	90
5.1	Friction	90
5.2	Wear: Subsurface Deformation	96
6.	Discussion of Experimental Results	122
6.1	Friction Coefficient and Wear	122
7.	A Comparison Between Ion Nitriding and Ion Implantation	133
7.1	Introductory Remarks	133
7.2	Advantages and Disadvantages of Ion Nitriding	133
7.3	Experimental Procedure	134
7.4	Experimental Results and Discussion	134
7.5	Concluding Remarks	139
8.	Conclusions and Recommendations	141
8.1	Major Conclusions	141
8.2	Recommendations for Future Work	143
	References	144
	Appendices	151
A.	Sample Material and Preparation	151
A.1	Chemical Composition and Processing Methods	151
A.2	Sample Sectioning and Mounting	153
B.	Estimation of Wear Volume Using Talysurf Trace	155
C.	FEM Solution	157
D.	Subsurface Stress Distributions	161
E.	Micrographs of Worn Surfaces	176

LIST OF FIGURES

<u>Figure Number</u>	<u>Page Number</u>
2.1.1 Adhesive wear model.	23
2.2.1 Delamination wear process.	26
2.2.2 Delamination wear sheet on wear track of iron solid solution.	28
2.2.3 Weight loss as a function of sliding distance for OFHC copper.	29
2.3.1 Regimes of frictional force vs. distance slid.	32
3.1.1 The behavior of the nuclear and electronic contributions to the specific energy loss dE/dx as a function of ion velocity.	37
3.1.2 Typical Gaussian distribution.	39
3.2.1 General layout of commercial type ion-implanter.	41
3.2.2 Schematic of the implantation process.	42
3.3.1 Implantation profile for a range of accelerating voltages.	45
4.1.1 Friction and wear testing apparatus.	63
4.1.2 Pin-on-disk tribotester.	63
4.2.1 Change in friction coefficient with sliding distance of unimplanted iron, Al^+ implanted iron, and N^+ implanted iron systems.	65
4.2.2 Change in friction coefficient with sliding distance of unimplanted Cu, Zn^+ implanted Cu, and N^+ implanted Cu systems.	66
4.2.3 Change in friction coefficient with sliding distance of unimplanted Ti, and N^+ implanted Ti systems.	67
4.2.4 Typical profiles of worn disk surfaces of unimplanted Fe, N^+ implanted Fe, and Al^+ implanted Fe.	69

4.2.5	Typical profile of a worn unimplanted Ti disk surface.	70
4.2.6	Typical profile of a worn disk surface of unimplanted Cu, Zn^+ implanted Cu, and N^+ implanted Cu.	71
4.2.7	Typical wear track of Al^+ implanted Fe disk; shallow plowing grooves.	72
4.2.8	Wear track of N^+ implanted Fe disk; deep plowing grooves.	73
4.2.9	Wear track of N^+ implanted Fe disk; severe plastic deformation of a thin layer.	74
4.2.10	Typical wear scar on an unimplanted Fe pin after 1 revolution of sliding.	76
4.2.11	Typical wear track of an unimplanted Fe disk after 1 revolution of sliding.	77
4.2.12	Typical wear track of N^+ implanted Ti disk.	78
4.2.13	Typical wear track on an unimplanted Ti disk.	80
4.2.14	Typical wear track of an unimplanted Cu disk.	81
4.2.15	Typical wear track of a N^+ implanted Cu disk.	82
4.2.16	Subsurface deformation of a typical worn N^+ implanted Cu specimen.	83
4.2.17	Subsurface deformation of a typical worn unimplanted iron specimen.	85
4.2.18	Subsurface deformation of a typical worn unimplanted Ti specimen.	86
4.2.19	Subsurface deformation of a typical worn Al^+ implanted Fe specimen.	88
5.1.1	Schematic representation of wear particle formation during sliding on an initially smooth surface.	92
5.1.2	Wear particle formation on the surface of an Al^+ implanted Fe pin after 5 cm of sliding on a lubricated Al^+ implanted disk.	94

5.2.1	Model of a contact between a stationary rigid asperity and a sliding isotropic linear elastic semi-infinite solid.	98
5.2.2	The steady state σ_{xx} component of the state of stress at different depths normalized with respect to the maximum applied normal stress, for $a=20\mu\text{m}$, $\mu=.1$, $E_1/E_2=2.5$ and $d=.2\mu\text{m}$.	100
5.2.3	The steady state σ_{yy} component of the state of stress at different depths normalized with respect to the maximum applied normal stress, for $a=20\mu\text{m}$, $\mu=.1$, $E_1/E_2=2.5$, and $d=.2\mu\text{m}$.	101
5.2.4	The steady state τ_{xy} component of the state of stress at different depths normalized with respect to the maximum applied normal stress, for $a=20\mu\text{m}$, $\mu=.1$, $E_1/E_2=2.5$, and $d=.2\mu\text{m}$.	102
5.2.5	The steady state τ_{\max} component of the state of stress at different depths normalized with respect to the maximum applied normal stress, for $a=20\mu\text{m}$, $\mu=.1$, $E_1/E_2=2.5$, and $d=.2\mu\text{m}$.	103
5.2.6	The steady state σ_{xx} component of the state of stress at different depths normalized with respect to the maximum applied normal stress, for $a=20\mu\text{m}$, $\mu=.1$, $E_1/E_2=2.5$, and $d=1\mu\text{m}$.	105
5.2.7	The steady state σ_{yy} component of the state of stress at different depths normalized with respect to the maximum applied normal stress, for $a=20\mu\text{m}$, $\mu=.1$, $E_1/E_2=2.5$, and $d=1\mu\text{m}$.	106
5.2.8	The steady state τ_{xy} component of the state of stress at different depths normalized with respect to the maximum applied normal stress, for $a=20\mu\text{m}$, $\mu=.1$, $E_1/E_2=2.5$, and $d=1\mu\text{m}$.	107
5.2.9	The steady state τ_{\max} component of the state of stress at different depths normalized with respect to the maximum applied normal stress, for $a=20\mu\text{m}$, $\mu=.1$, $E_1/E_2=2.5$, and $d=1\mu\text{m}$.	108
5.2.10	The steady state τ_{xy} component of the state of stress at different depths normalized with respect to the maximum applied normal stress, for $a=20\mu\text{m}$, $\mu=.1$, $E_1/E_2=1$, and $d=.2\mu\text{m}$.	109

5.2.11 The steady state τ_{\max} component of the state of stress at different depths normalized with respect to the maximum applied normal stress, for $a=20\mu\text{m}$, $\mu=.1$, $E_1/E_2=1$, and $d=.2\mu\text{m}$. 110

5.2.12 The steady state τ_{xy} component of the state of stress at different depths normalized with respect to the maximum applied normal stress, for $a=20\mu\text{m}$, $\mu=.47$, $E_1/E_2=2.5$, and $d=.2\mu\text{m}$. 112

5.2.13 The steady state τ_{\max} component of the state of stress at different depths normalized with respect to the maximum applied normal stress, for $a=20\mu\text{m}$, $\mu=.47$, $E_1/E_2=2.5$, and $d=.2\mu\text{m}$. 113

5.2.14 The steady state τ_{xy} component of the state of stress at different depths normalized with respect to the maximum applied normal stress, for $p=1/2p_0$, $a=20\mu\text{m}$, $\mu=.1$, $E_1/E_2=2.5$, and $d=.2\mu\text{m}$. 114

5.2.15 The steady state τ_{\max} component of the state of stress at different depths normalized with respect to the maximum applied normal stress, for $p=1/2p_0$, $a=20\mu\text{m}$, $\mu=.1$, $E_1/E_2=2.5$, and $d=.2\mu\text{m}$. 115

5.2.16 The steady state τ_{xy} component of the state of stress at different depths normalized with respect to the maximum applied normal stress, for $p=3/4p_0$, $a=20\mu\text{m}$, $\mu=.1$, $E_1/E_2=2.5$, and $d=.2\mu\text{m}$. 116

5.2.17 The steady state τ_{\max} component of the state of stress at different depths normalized with respect to the maximum applied normal stress, for $p=3/4p_0$, $a=20\mu\text{m}$, $\mu=.1$, $E_1/E_2=2.5$, and $d=.2\mu\text{m}$. 117

5.2.18 The steady state τ_{\max} component of the state of stress at different depths normalized with respect to the maximum applied normal stress, for $p=1/2p_0$, $a=20\mu\text{m}$, $\mu=.1$, $E_1/E_2=1$. 119

5.2.19 The steady state τ_{\max} component of the state of stress at different depths normalized with respect to the maximum applied normal stress, for $p=3/4p_0$, $a=20\mu\text{m}$, $E_1/E_2=1$, and $\mu=.1$. 120

6.1.1	Typical N^+ implanted titanium pin surface.	123
6.1.2	Typical N^+ implanted Fe pin surface after 25 cm of sliding.	124
6.1.3	Predicted depth profiles of some implanted metals.	126
6.1.4	Typical Al^+ implanted Fe specimen wear groove.	129
6.1.5	Model of contact between a rigid asperity and an Al^+ implanted Fe surface.	130
7.4.1	Change in friction coefficient with sliding distance of unimplanted Fe, ion nitrided Fe, and N^+ implanted Fe systems.	135
7.4.2	Typical wear track of an ion nitrided Fe disk.	137
7.4.3	Typical wear scar on an ion nitrided Fe pin.	138
A.2.1	The principle of Taper Sectioning.	154
B.1	A typical surface profile of a wear track.	156
C.1	Finite Element grid used to represent a hard thin layer on a soft bulk material.	158
C.2	Typical 2-D elements including nodal point configuration.	159
C.3	Schematic for weighted average technique.	159
D.1	The steady state σ_{xx} component of the state of stress at different depths normalized with respect to the maximum applied normal stress, for $a=20\mu m$, $\mu=.1$, $E_1/E_2=1$.	162
D.2	The steady state σ_{yy} component of the state of stress at different depths normalized with respect to the maximum applied normal stress, for $a=20\mu m$, $\mu=.1$, $E_1/E_2=1$.	163
D.3	The steady state σ_{xx} component of the state of stress at different depths normalized with respect to the maximum applied normal stress, for $a=20\mu m$, $\mu=.47$, $E_1/E_2=2.5$, and $d=.2\mu m$.	164
D.4	The steady state σ_{yy} component of the state of stress at different depths normalized with respect to the maximum applied normal stress, for $a=20\mu m$, $\mu=.47$, $E_1/E_2=2.5$, and $d=.2\mu m$.	165

D.5	The steady state σ_{xx} component of the state of stress at different depths normalized with respect to the maximum applied normal stress, for $p=1/2p_0$, $a=20\mu\text{m}$, $\mu=.1$, $E_1/E_2=2.5$, $d=.2\mu\text{m}$.	166
D.6	The steady state σ_{yy} component of the state of stress at different depths normalized with respect to the maximum applied normal stress, for $p=1/2p_0$, $a=20\mu\text{m}$, $\mu=.1$, $E_1/E_2=2.5$, $d=.2\mu\text{m}$.	167
D.7	The steady state σ_{xx} component of the state of stress at different depths normalized with respect to the maximum applied normal stress, for $p=3/4p_0$, $a=20\mu\text{m}$, $\mu=.1$, $E_1/E_2=2.5$, $d=.2\mu\text{m}$.	168
D.8	The steady state σ_{yy} component of the state of stress at different depths normalized with respect to the maximum applied normal stress, for $p=3/4p_0$, $a=20\mu\text{m}$, $\mu=.1$, $E_1/E_2=2.5$, $d=.2\mu\text{m}$.	169
D.9	The steady state σ_{xx} component of the state of stress at different depths normalized with respect to the maximum applied normal stress, for $p=1/2p_0$, $a=20\mu\text{m}$, $\mu=.1$, $E_1/E_2=1$.	170
D.10	The steady state σ_{yy} component of the state of stress at different depths normalized with respect to the maximum applied normal stress, for $p=1/2p_0$, $a=20\mu\text{m}$, $\mu=.1$, $E_1/E_2=1$.	171
D.11	The steady state τ_{xy} component of the state of stress at different depths normalized with respect to the maximum applied normal stress, for $p=1/2p_0$, $a=20\mu\text{m}$, $\mu=.1$, $E_1/E_2=1$.	172
D.12	The steady state σ_{xx} component of the state of stress at different depths normalized with respect to the maximum applied normal stress, for $p=3/4p_0$, $a=20\mu\text{m}$, $\mu=.1$, $E_1/E_2=1$.	173
D.13	The steady state σ_{yy} component of the state of stress at different depths normalized with respect to the maximum applied normal stress, for $p=3/4p_0$, $a=20\mu\text{m}$, $\mu=.1$, $E_1/E_2=1$.	174
D.14	The steady state τ_{xy} component of the state of stress at different depths normalized with respect to the maximum applied normal stress, for $p=3/4p_0$, $a=20\mu\text{m}$, $\mu=.1$, $E_1/E_2=1$.	175

E.1 Typical wear scar on an Al⁺ implanted Fe pin 176
after 5 cm of sliding on an Al⁺ implanted
Fe disk.

E.2 Typical wear scar on an unimplanted Fe pin 177
after 5 cm of sliding.

E.3 Typical wear scar on a N⁺ implanted Fe pin. 178

E.4 Typical wear track on an unimplanted Fe disk. 179

LIST OF TABLES

<u>Table Number</u>		<u>Page Number</u>
3.4.1	Effect of Ion Implantation on Friction Coefficient	48
3.4.2	Effect of Ion Implantation on Wear	53
3.4.3	Effect of Ion Implantation on Hardness	56
A.1.1	Chemical Analysis of High Purity Iron	152

1. INTRODUCTION

If a surface treatment were developed which would reduce friction and wear between sliding surfaces, both energy and cost would be saved. In the United States alone, several billion dollars are spent each year to replace worn out pistons, bearings, cutting tools, and the like. It is apparent that a superior wear resistant surface would not only have a large economic impact, but, also would open up new opportunities in design and manufacturing. Surface treatments presently being used on a commercial basis to alter the tribological properties of metals include ion nitriding, vacuum coating, and chemical vapor deposition processes. Recently, ion implantation has shown promise as a method of improving not only friction and wear properties, but also fatigue, corrosion, and oxidation properties of metals. Ion implantation is a process by which high energy ions strike and penetrate a solid target at the end of a vacuum chamber.

In the past decade, numerous investigators have shown that ion implantation improves wear. However, tribological properties of implanted metals have not been clearly established. A basic understanding of chemical and mechanical modifications of the implanted surface is a pre-requisite for understanding how ion implantation affects

the friction and wear behavior of metals. Small amounts of alloying elements can significantly modify the surface chemistry [1] and affect the friction and wear of the surface. Through the understanding of the effects of ion implantation on chemical and physical behavior, the mechanisms of friction and wear can be established to provide the basis for optimizing the implantation process. It is in this area of fundamental understanding that present knowledge is deficient.

In chapter 2, the theories of friction and wear, specifically the classical adhesion theory and the more recent delamination theory are described. The review discusses the deficiencies of the adhesion model and explains how the delamination theory accounts for these deficiencies. Specifically, the delamination model explains the dependency of the wear rate and friction coefficient on sliding distance. The principles of this theory indicate that the implications of ion implantation may be important in lowering friction and prolonging mild forms of wear.

Relevant literature and some background information on the basic process and equipment is reviewed in Chapter 3. In the past, changes in the friction coefficient and decreases in the wear rate were observed for a wide variety of ion-substrate combinations including careful examination of the chemical and mechanical nature of the implanted

surface. Despite the efforts of these investigators, fundamental research is still needed in order to understand the many implications of ion implantation. Various hypotheses, including increased hardness, oxide formation, and changes in the chemical nature of the surface, have been advanced. They attempted to explain how this process, affecting such a thin layer, can produce such drastic changes in the tribological behavior of metals. However, many of these hypotheses are not supported by experimental evidence or by fundamental mechanics of materials. For example, if the hardness is increased or if the chemical properties of the surface are changed in such a thin layer, then how do these effects interact with the friction and wear mechanisms? This question remains unanswered, and has prompted the work summarized in this report.

Experimental procedure and results are reported in Chapter 4. The experimental procedure is given in detail so that the results of different investigations can be accurately compared. Numerous articles written on ion implantation do not give sufficient detail of the experimental procedure to make their results valuable to other investigators. The variation between experimental programs has been pointed out to caution the reader when interpreting and comparing results. Briefly, the experimental results of this investigation show that of the ion-substrate systems investigated, only the Al^+/Fe , N^+/Fe

and N^+ /Ti systems showed an improvement in the friction and wear properties over the unmodified surface. N^+ and Zn^+ implanted into copper did not enhance the tribological behavior of the surface.

Using the experimental results as a guide, a model of the mechanisms of friction and wear of ion-implanted metals, based on the delamination theory, is postulated in Chapter 5. The relationship between hardness, surface chemistry, and plowing is introduced. It is interesting that the role of a thin hard layer is not one of supporting the forces, as is the case with a thick hard layer, but one of reducing plowing. Under the experimental conditions used in conducting the tests, the plowing component is the major component of the friction force. Hence, a reduction in plowing implies a reduction in the friction coefficient. A finite element model of the subsurface deformation for an isotropic linear elastic semi-infinite solid under the contact of a stationary, rigid asperity, shows that the friction coefficient has the most influence on reducing wear for a metal substrate with a hard thin layer near the surface. Thus the reduction in the friction of ion-implanted metals is accompanied by a reduction in the wear rate.

In Chapter 6, the experimental results are discussed. In the past, examination of the specimen surface was of primary interest. The importance of observing both the slider and specimen is discussed. It is not sufficient to examine just the specimen surface since the geometry and contact forces differ significantly between the disk and pin. The chapter concludes with a proposed model of friction and wear behavior of the Al⁺ implanted iron system, which accounts for the continued wear resistance of the specimen surface at depths much greater than that of the implanted layer.

A common question is whether ion implantation compares favorably with other surface treatment processes as a method of reducing wear. If ion implantation cannot enhance the tribological properties of metals to the extent that other processes can, then it may have no practical application. This has prompted the work discussed in Chapter 7. Conventional ion nitriding is compared against the implantation process. Finally, conclusions and recommendations, based on the results of this investigation, are summarized in Chapter 8.

2. FRICTION AND WEAR THEORIES

The basic friction and wear theories are reviewed, since it is only through the understanding of these theories that a model for the wear of ion-implanted metals can be postulated.

2.1 Adhesive Wear

Wear has been typically classified into the following categories [2]: adhesive wear, abrasive wear, corrosive wear, and surface fatigue wear. The most common of these is adhesive wear, which occurs whenever two bodies slide over each other. When a junction from one of the surfaces comes in contact with a junction from the opposing surface, there is a probability (small but finite) that shearing will not occur at the interface, but within one of the materials when this contact is broken. This material may transfer to the opposing surface or may come off as a loose particle (see Figure 2.1.1).

Some of the earliest work in wear theory was conducted by Archard [3] in 1953 when he developed quantitative laws of adhesive wear. He proposed that the wear volume of fragmented particles is given by:

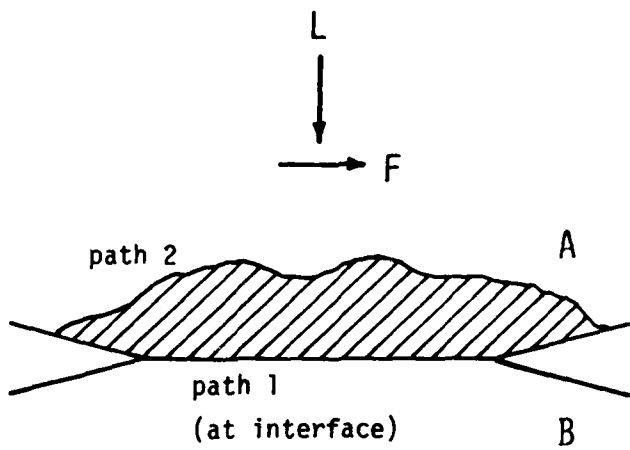


Figure 2.1.1 Adhesive wear model. If the shear strength of the junction is higher than the bulk strength of the weaker material A, shear will take place in material A (path 2) instead of at the interface (path 1). [reference 2]

$$V = \frac{kLX}{3P}$$

Where:

k = wear coefficient

L = normal load

P = hardness of the softer material

X = sliding distance

The wear coefficient, k , is dimensionless and can be considered as the probability of forming a loose wear particle during the transfer of particles between two bodies. It is often used to compare relative wear resistance between materials. Yet, the dependency of k on such parameters as cleanliness, and mechanical and chemical properties, is not clear. This model assumes circular junctions and hemispherical fragments which gives rise to the factor of 3 in the denominator.

In the past decade Rabinowicz [4] has investigated the effects of surface energy and other chemical properties on adhesive wear and has used these results to help predict the wear coefficient which has had great practical application. Recently, researchers have begun to challenge the validity of the basic adhesive model since it does not consider the mechanics of deformation and fracture [5]. This has given rise to the delamination theory of wear.

2.2 Delamination Theory Of Wear

The delamination theory of wear was proposed because the observed behavior of sliding surfaces can not be explained using the adhesive theory of wear. According to the delamination theory, wear particles are formed by the following mechanisms under sliding conditions [6] (Figure 2.2.1):

1. When two sliding surfaces contact, the tangential and normal forces are transmitted at the point of contact by adhesion and deformation of asperities. The softer material becomes smooth after repeated traversals due to the deformation and fracture of the soft asperities by the harder surface.
2. Upon repeated traversals the subsurface of the softer material undergoes plastic deformation.
3. This subsurface deformation continues until voids are nucleated below the surface. These voids do not nucleate at the surface since the triaxial state of compressive stress, which opposes void nucleation, is maximum at the surface. At a depth where the compressive stresses becomes smaller than the deformation induced stresses, void nucleation becomes possible. This usually occurs at a distance approximately equal to the width of the contact.
4. Once cracks are created (or exist before sliding due to

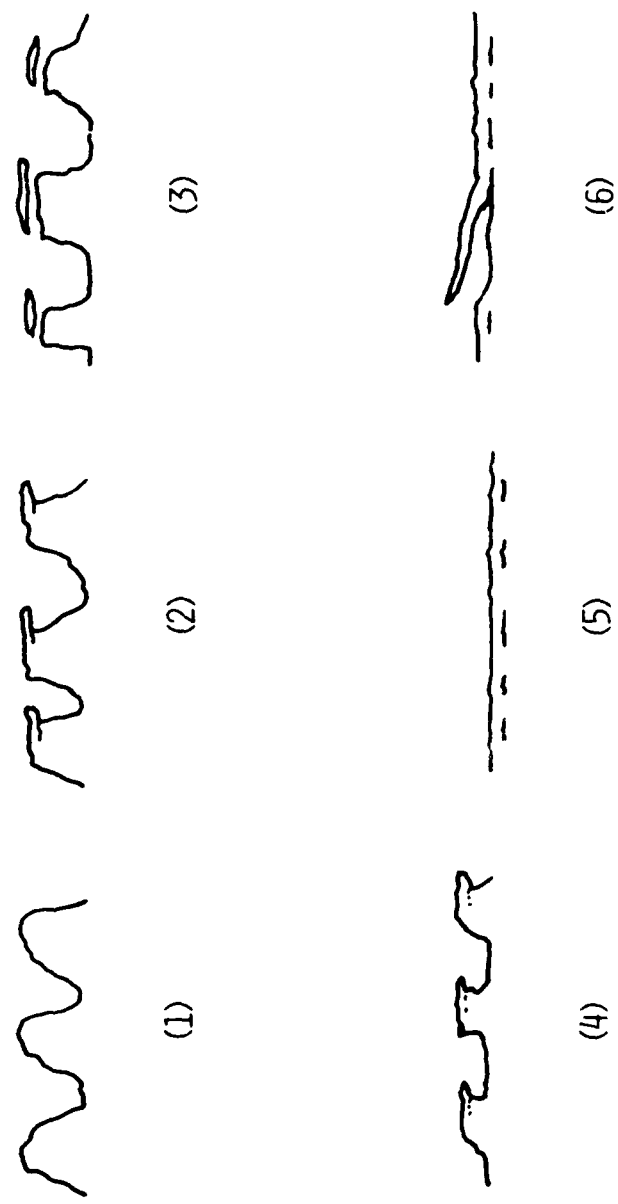


Figure 2.2.1 Delamination wear process. [reference 5]

processing methods) further loading causes the cracks to propagate, generally parallel to the surface. These cracks eventually join surrounding cracks. Note that the cracks may not extend if the conditions for propagation are not satisfied, i.e. sufficient subsurface deformation and small tangential traction.

5. The cracks eventually propagate to the surface once they become unstable and form a delamination wear particle. Figure 2.2.2 illustrates a wear sheet formed in an iron solid solution.

From the above description it is evident that the major factor affecting the delamination wear process is the state of stress beneath the surface.

Before concluding the discussion on the delamination process, it is worth noting that the wear rate is dependent on sliding distance. Figure 2.2.3 shows the weight loss of O.F.H.C. copper as a function of sliding distance. There is not a linear dependence between the worn volume and sliding distance, as predicted by the adhesion theory [7-9]. During the initial stages of wear, the rough surface becomes smooth by the process of asperity deformation. The wear rate remains at a plateau until the subsurface becomes sufficiently deformed to form the delamination wear sheets. The time duration of this no-wear-region depends on the rate of crack nucleation and crack propagation. These in turn

SLIDING DIRECTION



Figure 2.2.2 Delamination wear sheet on wear track of iron solid solution. [reference 5]

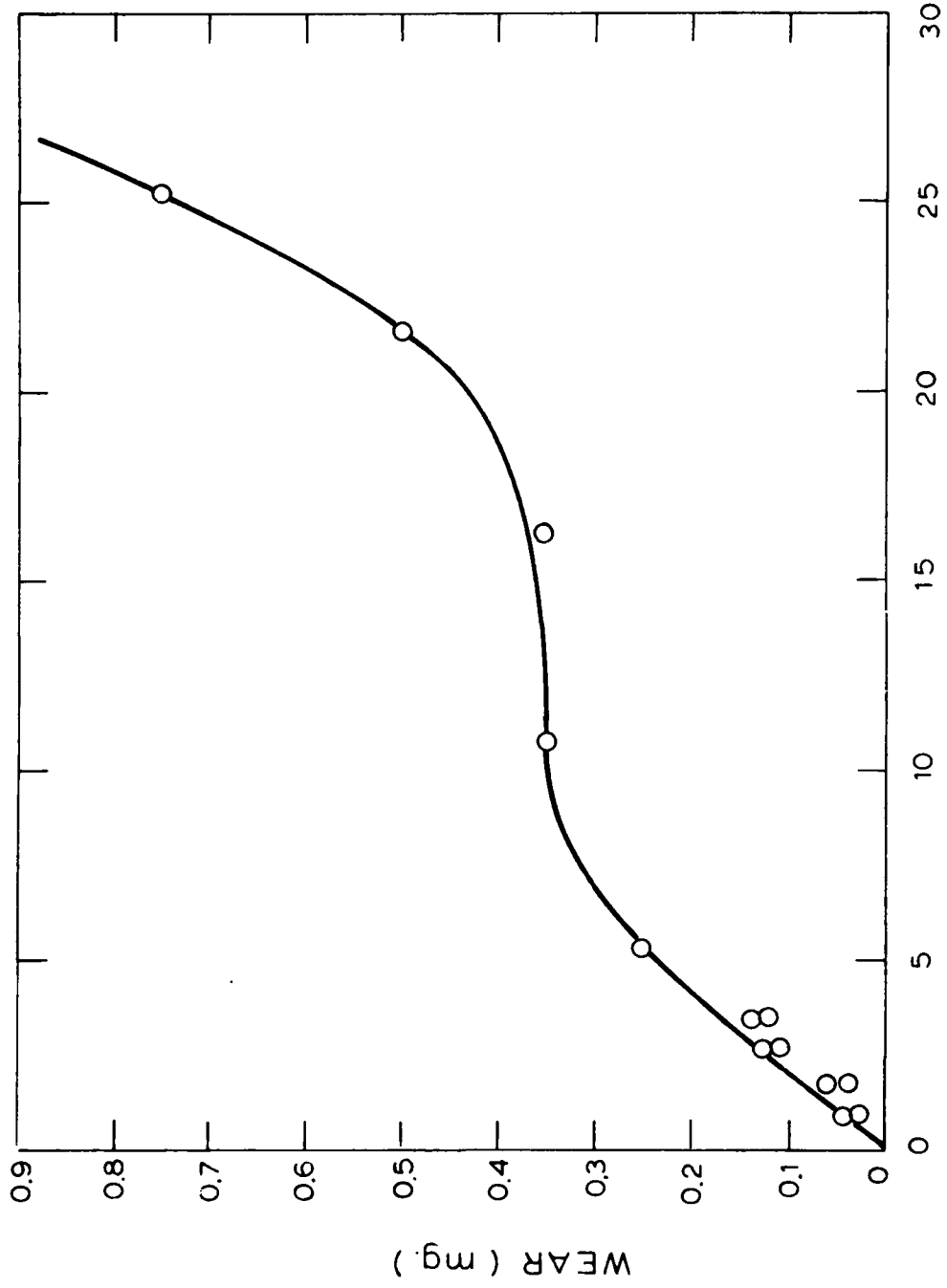


Figure 2.2.3 Weight loss as a function of sliding distance for OFHC copper sliding under a load of 1.15 kg in argon. [reference 5]

are controlled by the surface traction and microstructure [5]. Note that the wear rate would initially be zero if the specimen and slider surfaces are smooth, as is the case for the implanted pins and disks used in this investigation. Thus ion implantation, as we will see in Chapters 3 and 4, appears to have the ability to alter the mechanical and/or chemical properties of the surface so as to prolong this wear plateau.

2.3 Theories of Friction

The predominant friction model over the past several decades is complementary to the adhesive wear model. Accordingly, the force required to shear the junction between two contacting bodies gives rise to the friction coefficient. For uncontaminated metals sliding together, the friction coefficient is given by:

$$\mu = \frac{S}{P}$$

Where:

S= bulk shear strength of the softer material

P= hardness of the softer material

According to this model the friction coefficient is predicted to be 1/6 for most combinations of materials. In practice, however, the friction coefficient varies widely.

To account for this variation, modifications have been made to this basic model. For example, Rabinowicz [4] has looked at the effect of mutual solubility and surface energy.

Even with modifications, the friction theory ignores the change in the friction coefficient as a function of sliding distance. Thus Suh et al. [10] has proposed a model similar to the delamination theory to predict the friction coefficient. He postulates that the friction force is composed of three components: that due to the deformation of asperities, that due to plowing, and that due to adhesion between contacting materials. Note that this theory does not ignore the adhesion theory, as evident by the dependence on adhesion, but it does change the emphasis.

The time dependency of the friction coefficient has been divided into six stages as follows (see Figure 2.3.1):

Regime 1 The friction force is primarily due to the deformation and fracture of asperities. The adhesion component is

a minor part of the friction coefficient and hence,

does not significantly depend on the material combination.

Regime 2 The friction force increases slightly due to the increasing role of adhesion. If the surface is

lubricated well, this regime may be eliminated. The friction force will increase if particles become

entrapped between the sliding surfaces.

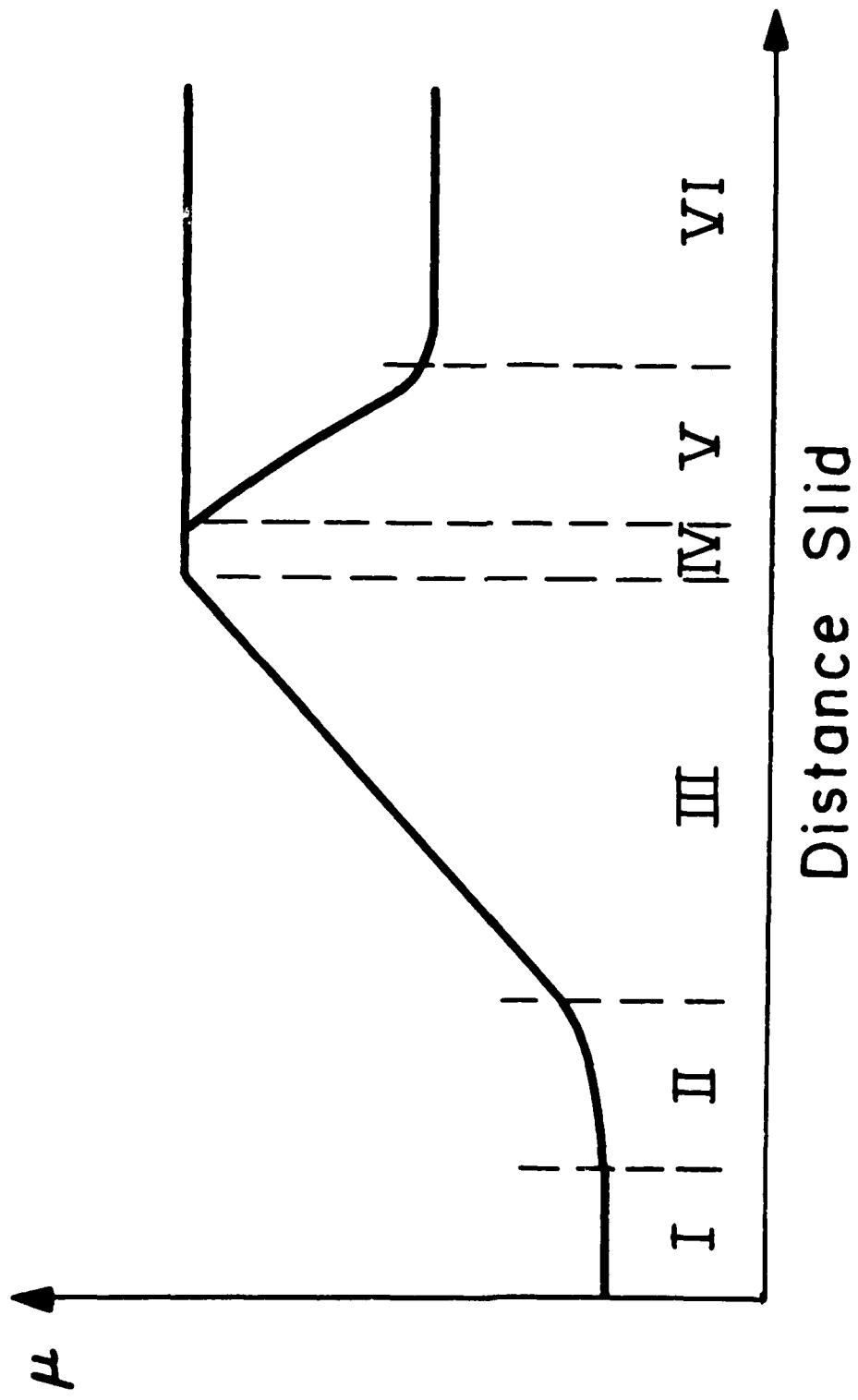


Figure 2.3.1 Regimes of frictional force vs. distance slid.
[reference 10]

Regime 3 All three components of the friction force become important. The friction coefficient increases rapidly due to the increase in the number of entrapped wear particles. If the sliding surfaces are of equal hardness then the wear particles will penetrate each surface equally, resulting in a high plowing component. The wear particles formed will include both delamination particles and those resulting from asperity deformation and fracture. The adhesion component increases due to an increase in clean interfacial areas.

Regime 4 The friction force levels off at this stage. This is the steady state friction coefficient for like metals and for combinations where stages 5 and 6 do not occur. In this regime the number of entrapped particles remains constant, i.e. the number of newly entrapped particles equal the number of entrapped particles leaving the interface. Adhesion and asperity deformation continue to play an important role.

Regime 5 In the case where a very hard slider is slid against a soft counterface, the hard surface becomes smooth due to asperity removal. The friction force decreases since the loose wear particles can no longer embed themselves into the hard surface and plow the softer material.

Regime 6 The surface finish on the hard surface reaches a

minimum roughness. The surface of the softer material then becomes smooth although not as smooth as the hard surface since newly forming delamination particles continuously leave the surface rough. If the softer material remains stationary and the harder surface is rotated, regimes 4 and 5 do not exist.

Suh [10] cites some experimental evidence of these stages.

Ion implantation may be used to prolong stage 2 before the onset of high friction and wear of stage 3.

3. ION IMPLANTATION

Ion implantation is a process by which ions are accelerated across a high potential to strike a solid target at the end of a vacuum tube. At low ion fluences, the ions are distributed in a more or less Gaussian distribution to depths usually ranging from $.02 \mu\text{m}$ to $.4 \mu\text{m}$. At higher fluences, such effects as sputtering and inward migration of atoms may alter or limit the depth of penetration. Virtually any element can be implanted into any substrate.

Interest in ion implantation grew rapidly during the 1960's because of its ability to modify the electrical properties of semiconductors. Initially there were doubts about the applicability of this process due to inadequate equipment and theory. Through advancements made in the design of accelerators and refinements made in implantation theory, ion implantation eventually replaced conventional diffusion processes. It has the advantage of superior controllability and reproducibility, and now is used in the production of pocket calculators and integrated circuits. Ion implantation into metals to change surface properties has only recently been investigated.

3.1 Range Calculations

In order to control the effects of ion implantation, the mechanisms which control energy loss and subsequently depth distribution must be understood. The theory most widely used to predict the range estimates is that described by Lindhard, Scharff, and Schiott (LSS) [11]. Numerous range-energy tables have been tabulated for a variety of ion-substrate combinations using this theory [12-15].

Briefly, the major energy loss processes in ion implantation include that due to direct collisions between the ion and a screened nucleus, and that due to the excitation of electrons bound in the solid. Thus the energy loss equation is

$$\frac{dE}{dx}_{\text{loss}} = \frac{dE}{dx}_{\text{nuclear}} + \frac{dE}{dx}_{\text{electronic}}$$

In the energy range of 5-500 keV the major contribution to energy loss is due to the nuclear interactions [12]. However, at higher energies electronic energies play a more important role (Figure 3.1.1).

The ions will eventually come to rest in a more or less Gaussian distribution when the energies are on the order of 20 eV [14]. The total distance traveled by the ion is defined as the total range, and the distance traveled parallel to the incident beam is the projected range. Since the ion is scattered at various angles the projected range

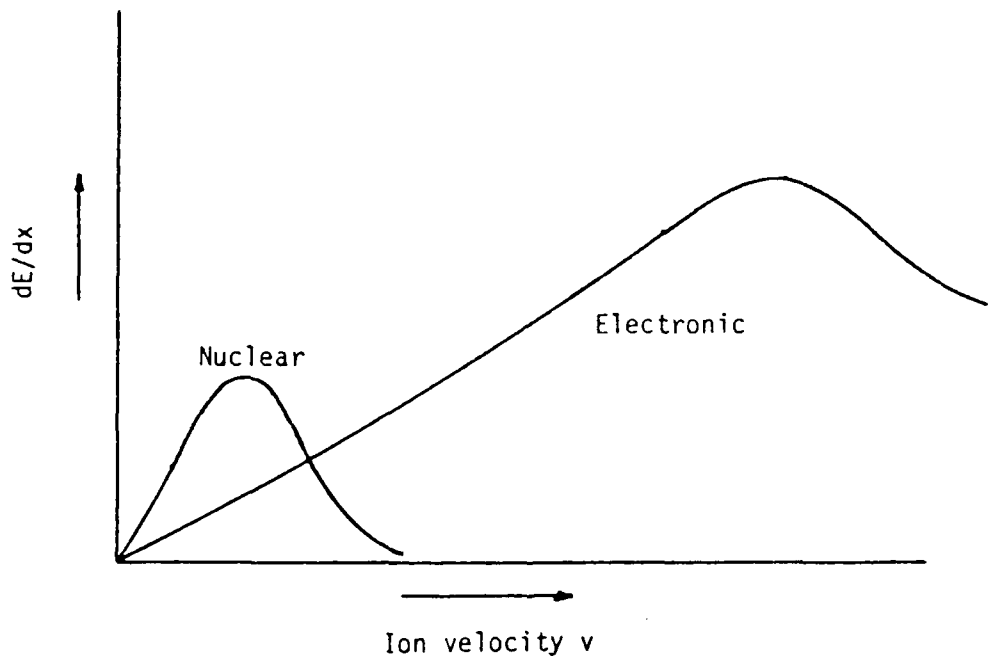


Figure 3.1.1 The behavior of the nuclear and electronic contributions to the specific energy loss dE/dx as a function of ion velocity v . [reference 16]

is always less than the total range. Figure 3.1.2 shows a typical Gaussian distribution defining the above parameters.

The LSS theory provides an approximate relationship between the total and projected range.

$$\frac{R_{\text{total}}}{R_p} \sim 1 + \frac{M_2}{3M_1}$$

and

$$R_{\text{total}} = \frac{.6(z_1^{2/3} + z_2^{2/3})^{1/2}}{z_1 z_2} \frac{(M_1 + M_2) M_2}{M_1} \frac{E}{D} 10^{-6}$$

where:

M_1, M_2 = atomic masses of the ion and atom respectively

z_1, z_2 = atomic numbers of the ion and atom respectively

E = accelerating voltage

D = target density

The spread in the range is described by the range straggling (ΔR_p) .

A useful estimate of the average concentration is described by:

$$\bar{N}_x = \frac{N_D}{2.5 \Delta R_p}$$

where N_D = ion dose expressed in ions per unit area.

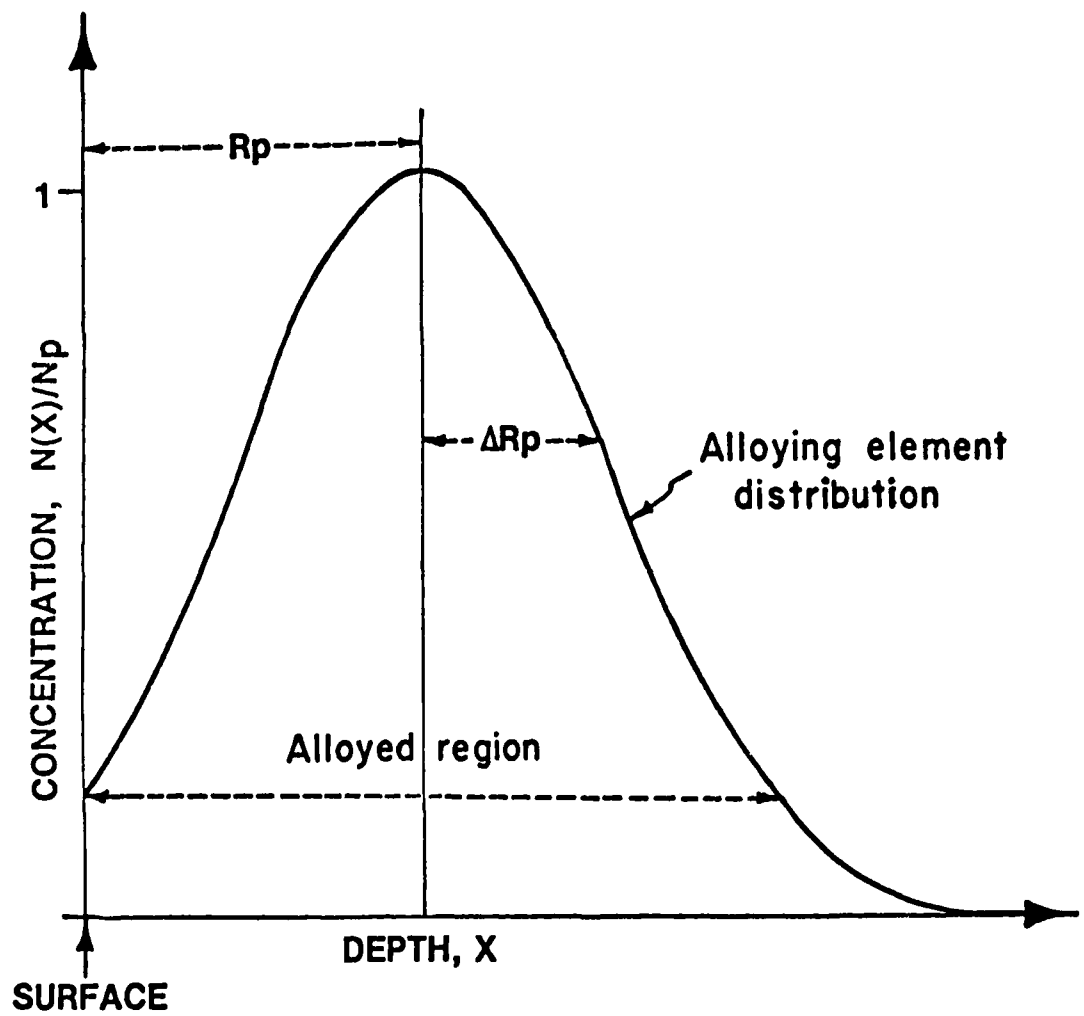


Figure 3.1.2 Typical Gaussian distribution for low-energy ions implanted into an amorphous material.
[reference 17]

The concentration of ions as a function of depth can be expressed by:

$$(N_x) \sim \frac{N_D}{2.5\Delta R_p} \exp \frac{-(x - R_p)^2}{\Delta R_p^2}$$

Various experimental techniques used to measure depth profiles include ion backscattering, auger analysis, ESCA, and nuclear reaction analysis. Literature on the effects of channeling, sputtering and radiation damage is available [12].

3.2 Ion Implantation Equipment

Figure 3.2.1 shows the layout of a production-type ion implanter used commercially in the semiconductor industry. Recently some of these implanters have been modified to accommodate metals.

A schematic of the implantation process is shown in Figure 3.2.2. A gas containing the desired ions (boron in this case) is injected into the high voltage end of the system. Electrons produced from a heated filament are accelerated back and forth between the two end plates by an anode and these electrons collide with the gas atoms, ionizing them. The ions are then extracted using a negative potential between the end plate and an extractor, and are accelerated due to the difference in potential between the

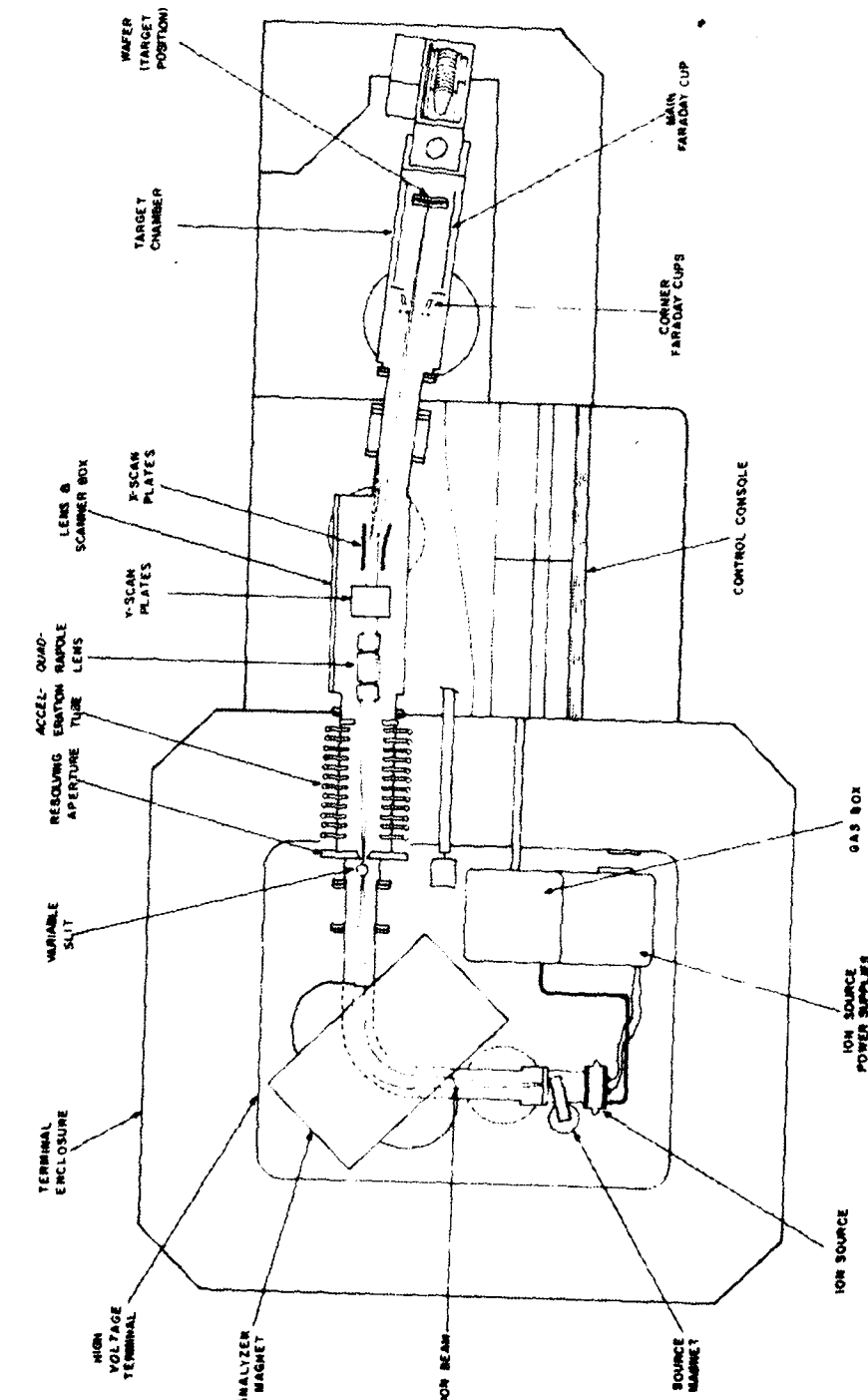


Figure 3.2.1 General layout of commercial type ion-implanter
 (Courtesy of Varian/Fextron).

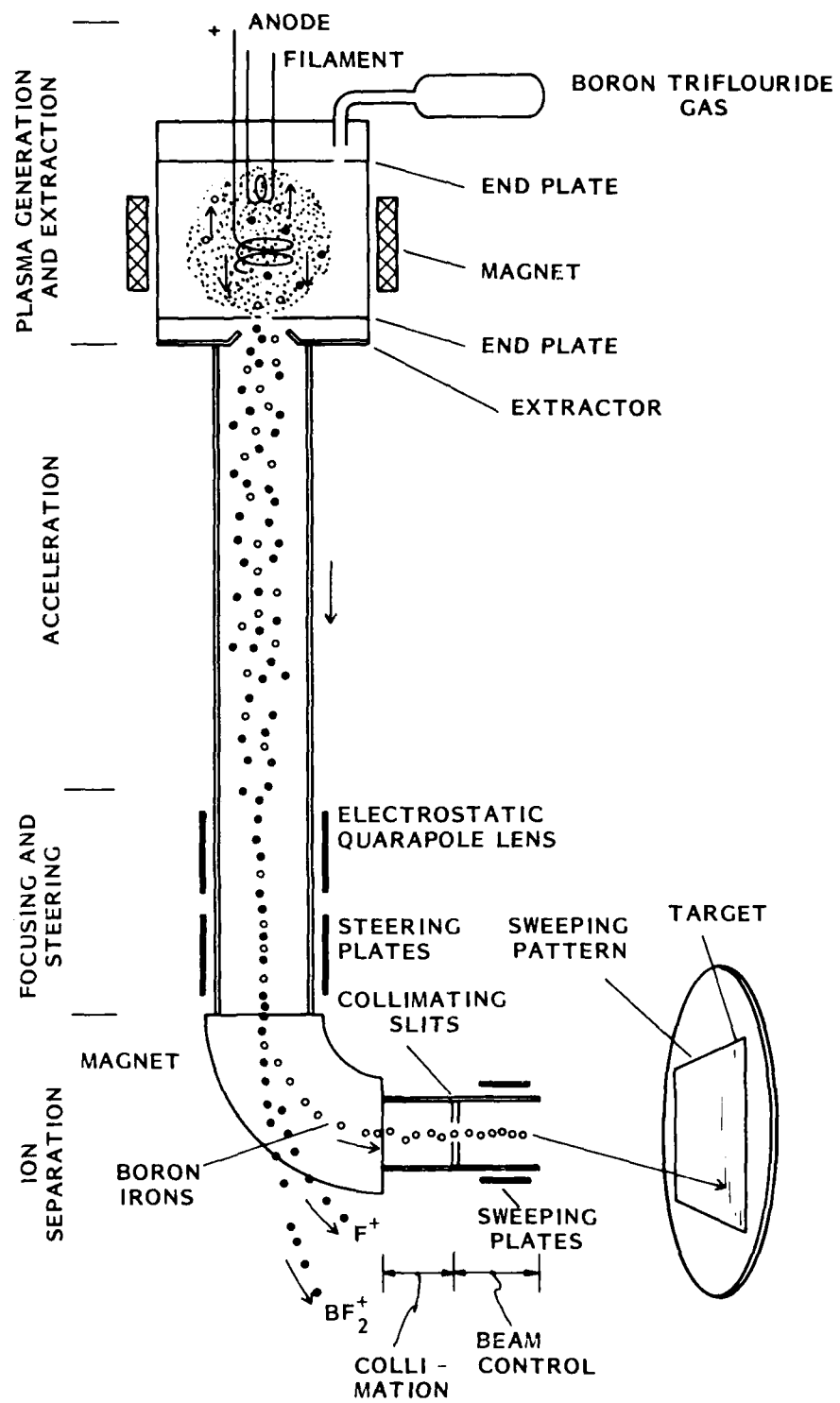


Figure 3.2.2 Schematic of the implantation process.
 [reference 18]

two ends of the column. The boron ions are sorted by bending the beam in a magnetic field. The beam is then collimated and focused on the target. The beam is either scanned across the target or held stationary as the target is moved across the beam [18]. The concentration versus depth profile is controlled by varying the accelerating voltage and dose.

Before metal parts can be processed on a commercial basis, machines need to be designed for this purpose. Presently, at Harwell, there is a commercial prototype that can process metal components up to 8 feet long. However, no such implanters are made on a commercial basis. Two major advantages in the design of metal implanters compared with semiconductor implanters are 1) the flexibility in doping uniformity and, 2) the beam purity requirements. These allow more freedom to the machine designers. Clearly, more work in machine design must be conducted if implanted metals are to have any commercial application.

3.3 Benefits and Drawbacks

Some of the advantages of ion implantation include those created by the chemical and mechanical properties of the surface which can lead to changes in friction and wear, oxidation, and corrosion properties. Other advantages of implantation are as follows:

1. There is no discernable dimensional change during ion implantation thus parts can be implanted following final machining.
2. Poor adhesion common with coatings is not a problem since the resulting implanted layer is a graded structure that lacks an interface between the implanted material and the host material.
3. Problems prevalent in conventional alloying such as the lack of mutual solubility between elements having extremely different melting points, ionic sizes, or electronegativities are eliminated. Hence, it is possible to incorporate elements that may not be added in conventional alloying processes.
4. Implantation can be carried out at low temperatures. This allows parts that have already been heat-treated to be implanted without altering the bulk microstructure.
5. Single isotopes can be implanted. This can be beneficial when implanting radioactive material.
6. Ion implantation offers better quality control than conventional diffusion processes.
7. There is no sacrifice of the bulk material.
8. The depth versus concentration distribution is controllable. Hence, the effect of varying alloy concentration can be readily examined.

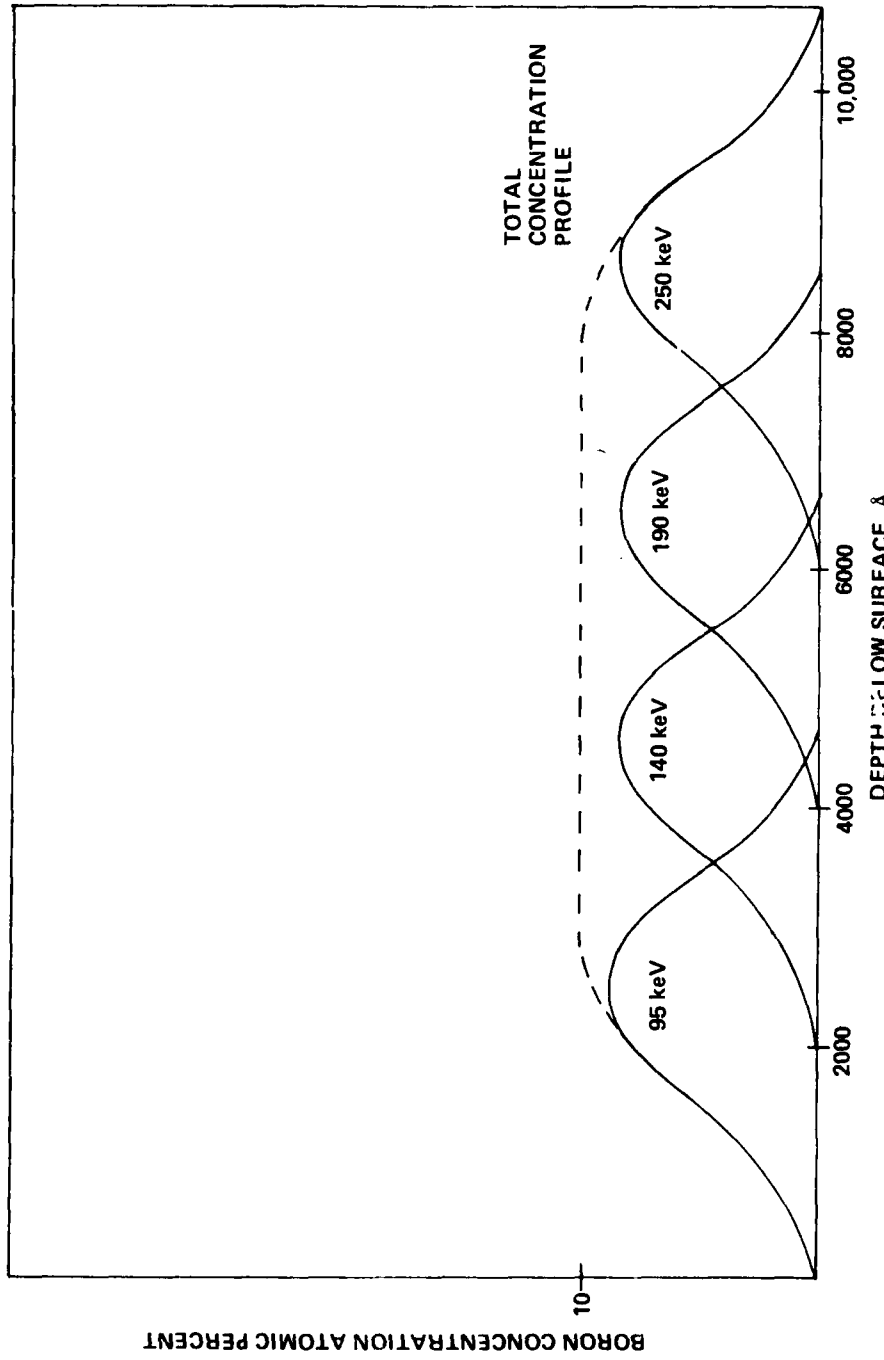


Figure 3.3.1 Implantation profile for a range of accelerating voltages (courtesy of Draper Lab.).

Although implantation appears to be an attractive process, it does have some limitations:

1. It is an expensive process, at present, compared with the diffusion process. Using present equipment, a part can cost anywhere between \$400 to \$2500 to implant depending on the dose, ion to be implanted, substrate, and beam current. If concrete evidence is revealed about its beneficial effects on modifying the mechanical and chemical properties of metals, then it is likely that the cost of processing will decrease as advances are made in machine design. Hirvonen [19] predicts a cost of $\$0.15/cm^2$ for an assumed operating cost of $\$35/hr$ and a dose of $10^{17} \text{ ions/cm}^2$.
2. It is a line-of-sight process, hence any sharp contours or intricate shapes may not be able to be implanted with present equipment.
3. The depth of penetration of the ions is shallow, usually ranging between $.02 \mu\text{m}$ to $.4 \mu\text{m}$. Hence, it appears that its effects on friction and wear may be limited to light loads and/or lubricated conditions. The depth of the alloyed region can, however be increased by using a range of accelerating voltages as shown in Figure 3.3.1. This would inevitably increase the cost of processing.
4. The maximum concentration of implantation is limited to

approximately 50% due to sputtering effects.

Despite these drawbacks, if ion implantation is shown to compare favorably with other surface treatments, technological advances will make ion implantation a competitive commercial process.

3.4 Literature Survey

Since the purpose of this report is to deal specifically with friction and wear of implanted metals, work conducted on the effects of ion implantation on oxidation and corrosion, [20-38] and fatigue [39-47] will not be discussed. Readers are referred to the numerous articles written on the subject. A brief review of the friction and wear literature will be described and critical questions concerning the work will be raised. For a more detailed review of the literature, refer to the numerous review articles [19, 34, 40] that have been published on the subject.

3.4.1 Friction

Implantation of a variety of metallic and non-metallic ions into numerous metals was found to change the friction coefficient in most cases. A summary of various investigations is found in Table 3.4.1.

Table 3.4.1 Effect of Ion Implantation on Friction Coefficient

Investigator	Material	Implanted Ions	Accelerating Voltage (kev)	Dose ^a (ions/cm ²)	Environment	Lubrication (kg)	Load	Initial μ	after Implant. μ	% Change	Remarks
Hartley et al. (ref. 49-53)	En 352	Kr ⁺	150-400	2.8x10 ¹⁶	air	White Spirit	2	.24	.24	0%	
	"	Sn ⁺	"	"	"	"	"	.24	.09	-62%	
	"	In ⁺	"	"	"	"	"	.31	.31	3.3%	
	"	As ⁺	"	"	"	"	"	.30	.22	18%	
	"	Pb ⁺	"	6.3x10 ¹⁶	"	"	"	.26	.26	4.3%	
	"	Mo ⁺	"	2.8x10 ¹⁶	"	"	"	.23	.33	-8%	k decreases w/ increasing dose
	"	S ⁺	"	6.1x10 ¹⁶	"	"	"	.26	.24	-5%	
	"	Mo ⁺ + S ⁺	"	5.6x10 ¹⁶	"	"	"	.20	.19	-2%	Mo ⁺ + S ⁺
Pavlov et al. (ref. 54)	Steel	Ar ⁺	40	9x10 ¹⁷	air	-	-	-	-	300%	
Suri et al. (ref. 55)	Al	B ⁺	-	10 ¹⁷	air	Not Used	.4	1.0	1.25	25%	Static Coef. of friction; 440C
	"	N ⁺	-	"	"	"	"	1.0	1.25	25%	
	Ti	B ⁺	-	"	"	"	"	.75	.85	1.3%	Stainless Rider
	"	N ⁺	-	"	"	"	"	.75	.90	20%	
	304SS	B ⁺	-	"	"	"	"	.60	.65	-8%	
	"	N ⁺	-	"	"	"	"	.65	.18	-73%	
	Al	B ⁺	-	"	"	"	"	1.0	1.20	20%	Dynamic Coef. of friction; 440C
	"	N ⁺	-	"	"	"	"	1.0	1.17	17%	
	Ti	B ⁺	-	"	"	"	"	.70	.70	0%	
	"	N ⁺	-	"	"	"	"	.70	.87	24%	
	304SS	B ⁺	-	"	"	"	"	.42	.39	-10%	
	"	N ⁺	-	"	"	"	"	.42	.17	-60%	
	Al	B ⁺	-	"	"	Kerosene	"	.22	.225	2.3%	
	"	N ⁺	-	"	"	"	"	.22	.30	36%	
	Ti	B ⁺	-	"	"	"	"	.70	.85	21%	
	"	N ⁺	-	"	"	"	"	.70	.82	17%	
	304SS	B ⁺	-	"	"	"	"	.15	.15	0%	
	"	N ⁺	-	"	"	"	"	.15	.15	0%	
Singer et al. (ref. 56)	S2100	Ti ⁺	190	5x10 ¹⁷	air	Not Used	1	.62	.38	-39%	
	"	"	"	16x10 ¹⁶	"	"	"	.62	.88	42%	
	"	"	"	5x10 ¹⁶	"	"	"	.62	.94	52%	
Hayashi et al. (ref. 32)	Si	Mo ⁺ , 10 ¹⁵	10 ¹⁵	10 ¹⁶	air	Not Used	-	-	change of .3	0%	
	"	50	10 ¹⁶	"	"	"	"	-	change of .22		
	"	100	"	"	"	"	"	-	change of .18		
	"	150	"	"	"	"	"	-	change of .8		
	"	50	5x10 ¹⁶	"	"	"	"	-	change of .5		
	"	100	"	"	"	"	"	-	change of .4		
	"	150	"	"	"	"	"	-	change of .19		

Hartley and co-workers [49-53] conducted much of the earlier work in friction and wear of implanted metals. They found that implantation of inert gases, i.e. Ar^+ and Kr^+ , do not change the friction coefficient. Hence implantation does not always result in a change in the friction force. One of the first clues that implantation may cause a change in the chemical nature of the surface was observed when molybdenum and sulfur ions were implanted into steel to a ratio of 1:2. The friction coefficient was substantially less than that of the unimplanted steel and that of steel with either molybdenum or sulfur ions implanted alone. Hartley speculates that this result is due to the formation of MoS_2 . However, a detailed investigation to confirm this has not been conducted. Since these experiments, research has been conducted on physics of implantation and on the chemical properties of the implanted surface [46,56-62]. Little of this work, however, has been carried out in conjunction with friction and wear tests.

Several investigators [50,32,56] have examined the effect of dose on the friction coefficient. They found that as the dose is increased, the relative change in friction becomes larger. The largest change in friction occurs at approximately 10^{17} ions/cm² for most ion-substrate combinations. Due to this dose dependency, the friction coefficient is meaningless unless the dose is specified. Because of this phenomenon, data that appear to disagree may

not be in conflict at all. For example, Hartley found that Ar^+ has no effect on the friction coefficient. Conversely, Pavlov [54] observed a 300% change in the friction coefficient with Ar^+ implanted to fluences of 9×10^{17} ions/cm². At fluences lower than 9×10^{17} ions/cm², Ar^+ may indeed have no effect on the friction coefficient. The importance of specifying the parameters under which the data is collected should not be underestimated. Often investigators neglect to give an adequate description of experimental procedure.

Hirvonen [40] has reviewed the work conducted at ONR. He confirmed some of the earlier observations of other investigators. In these tests, however, a ball-on-cylinder or a cylinder-on-cylinder tribotester was used instead of a pin-on-disk type tester.

Suri, Nammagadda, and Bunshah [55] conducted friction and wear tests with B^+ and N^+ implanted into various materials under unlubricated and lubricated conditions. They found that when implanted 304SS tests were lubricated, the change in the friction coefficient was not as substantial as in the unlubricated tests. This indicates that implantation can change the adhesion component of friction. Under lubricated conditions, metal to metal contact is minimized, hence adhesion plays a minor role. Under unlubricated conditions, however, the adhesion

component may be large. In contrast, N^+ implanted into aluminum and B^+ implanted into titanium showed a more substantial change in the friction force under lubricated conditions. A possible explanation is that under dry sliding conditions, the contact load is substantially increased, hence the thin implanted layer may be worn away after a short sliding distance. Also, the adhesion component may be increased.

Hayashi et al. [32] examined the effect of varying the accelerating voltage on friction with S45C carbon steel implanted with Ni^+ and Cr^+ . They found that for a lower accelerating voltage, the change in friction of the implanted surface becomes larger, and explain this phenomenon by citing the dependency of friction on ion concentration of the implanted layer.

To summarize the basic points on the friction of implanted metals:

1. Implantation does not invariably reduce friction.
2. Frictional properties introduced by implantation appear to depend on the nature of the implanted ion.
3. Frictional change for many implanted surfaces becomes more pronounced as the dose is increased.

Some of the mechanisms suggesting how ion implantation reduces the friction coefficient include:

- Oxide formation
- Chemical change, specifically alloying effects, of the surface
- Change in hardness due to the development of internal stress fields in the surface layer.

This by no means exhausts the subject of ion implantation and its effects on friction, but it does give a flavor for the state of the art. It is apparent, that despite work conducted to date, the mechanisms of friction for implanted metals are not understood well.

3.4.2 Wear

Various investigators have shown that ion implantation has a significant effect on the wear properties of metals. The most common types of tribotesters used for wear tests are pin-on-disk and cylinder-on-cylinder geometries. In many of these tests an unimplanted pin was slid against an implanted disk. Hirvonen et al. [63] found that for N^+ implanted into steel disks, the wear rate was the same whether implanted or unimplanted pins were used. They found, however, that the sliding member must be implanted for reduced wear even when the pin is implanted. Table 3.4.2 lists the results of various wear investigations.

Table 3.4.2 Effect of Ion Implantation on Wear

Investigator	Material	Implanted Ions	Accelerating Voltage (keV)	Dose (ions/cm^2)	Environment Lubrication	Load/Force (kgf)	Tribotester	Initial k after wear	Reduction in wear rate
Hartley et al. (ref. 4-53)	Steel	N^+	35	10^{18}	air	White Spirit	10N	3×10^{-6}	-
	"	"	"	"	"	"	10^{-5}	10^{-6}	-
	"	"	"	"	"	"	10^{-5}	10^{-6}	-
	En40B	"	30	10^{17}	air	"	"	-	30x
	"	"	"	10^{16}	air	"	"	-	-
	"	"	"	10^{18}	air	"	"	-	-
	Steel	B^+	40	5.6×10^{16}	"	"	"	3×10^{-5}	6×10^{-6}
	"	"	"	"	"	"	"	7×10^{-5}	6×10^{-6}
	"	"	"	"	"	"	"	11×10^{-5}	6×10^{-6}
	Mo^+	"	400	2.8×10^{16}	"	"	"	10^{-5}	6×10^{-5}
	Steel	"	"	"	"	"	"	10^{-5}	6×10^{-5}
	"	"	"	"	"	"	"	3×10^{-6}	6.5×10^{-5}
	Cu	B^+	40	10^{17}	"	Not Used	5N	10^{-6}	5×10^{-6}
	"	"	"	"	"	"	"	3×10^{-6}	4×10^{-6}
	"	"	"	"	"	"	"	3×10^{-6}	2×10^{-5}
Pavlov et al. (ref. 54)	Al	$\text{N}^+, \text{C}^+, \text{Ar}^+$	-	-	-	-	-	-	10x
Suri et al. (ref. 55)	Al	B^+	-	10^{17}	air	Kerosene	$.4 \text{kg}$	pin-on-disk	2.5×10^{-4}
	"	"	-	10^0	"	Not Used	"	2.5×10^{-5}	4.5×10^{-4}
	"	N^+	-	"	"	Kerosene	"	4×10^{-6}	-
	"	"	-	"	"	Not Used	"	2.5×10^{-5}	6×10^{-6}
	Ti	B^+	-	"	"	Kerosene	"	"	2.5×10^{-4}
	"	"	-	"	"	Not Used	"	3.5×10^{-4}	4×10^{-4}
	"	N^+	-	"	"	Not Used	"	3.5×10^{-4}	4.5×10^{-4}
	304SS	B^+	-	"	"	Kerosene	"	1.3×10^{-5}	1.1×10^{-5}
	"	"	-	"	"	Not Used	"	1.4×10^{-3}	1.2×10^{-3}
	"	N^+	-	"	"	Kerosene	"	1.3×10^{-3}	-
	"	"	-	"	"	Not Used	"	1.4×10^{-3}	7×10^{-3}
Hirvonen (ref. 40)	416SS	N^+	40	10^{17}	-	Used	2kg	cyl-on-cyl	$100x$
	"	Ar^+	"	"	"	"	"	"	$0x$
	304SS	C^+	"	"	"	"	"	"	$20-100x$
	52100	N^+	"	"	"	"	"	"	$2x$
Lo Russo et al. (ref. 45)	-	N^+, N_2^+	30	6×10^{16}	-	Not Used	2kg	bail-on-cyl	$3x$
Hayashi et al. (ref. 32)	Si^{45}C	N^+	-	10^{17}	air	Not Used	1kgf	-	$10x$

- = Not mentioned in literature

k = wear coefficient

Suri et al. [55] found that the reduction in the wear parameter is considerably larger for most ion-substrate combinations under lubricated conditions than for unlubricated conditions. This may be attributed to the much higher wear rates (20x) under dry sliding conditions, and consequently the implanted layer is worn away after shorter sliding distances. A direct comparison between lubricated and unlubricated tests is meaningless since the mechanisms of wear are much different in each case. In the first hours of lubricated testing (mild wear) the wear particle formation is mainly attributed to asperity deformation and removal, whereas in dry sliding (severe wear) the wear is governed by the delamination process.

Numerous investigators found that the increased wear resistance of implanted metals persisted beyond the depth of the implanted layer by several orders of magnitude. Lo Russo et al. [45], for example, observed a continued reduction in the wear rate of N^+ implanted into 38NCD4 steel even after the removal of several μm of material. Using nuclear reaction analysis, he found 20% of the implanted N^+ dose remained after the removal of 5 μm of material. This effect has been attributed to the inward diffusion of the implanted ion due to an increase in surface temperature, although the temperature rise during sliding was not calculated or measured. For the sliding velocities used, the flash temperature is only on the order of several

hundred degrees Faranheit [2]. Hence it seems unlikely that the ions would migrate 10x-100x the depth of the implanted layer during the wear test even under unlubricated conditions. A possible explanation for this increased wear resistance at depths much greater than the implanted layer is presented in Chapter 6. Briefly, the implanted layer may be pushed down to depths greater than the implanted layer during sliding, instead of the material actually being removed. The path created by a sled being moved over snow is a good analogy.

Again as with the friction coefficient, the wear rate has a dose dependency. Hence, correlation and interpretation of results between various investigators is difficult.

3.4.3 Hardness

On numerous occasions, the increase in the wear resistance and change in the friction coefficient has been attributed to the increase in hardness of the implanted surface layer. Because this is so frequently observed a separate review on the effect of ion implantation on hardness and in turn of hardness on the friction and wear properties seems appropriate. Table 3.4.3 summarizes some of the experimental results dealing with the hardness of the implanted layer.

Table 3.4.3 Effect of Ion Implantation on Hardness

Investigator	Material	Implanted Ions	Accelerating Voltage (kev)	Dose (Ions/cm ²)	Load (kgf)	Initial Hardness (kg/mm ²)	Final Hardness (kg/mm ²)	Improvement %	Penetration technique (PT)	Remarks
Kanaya et al. (ref. 6a)	SCM steel	N ⁺	2.4	10 ¹⁷	-	300	400	33%		
Gavovich et al. (ref. 65)	Steel	N ⁺	2-15	-	-	-	-	300%	"	"
Takaki et al. (ref. 66)	Pure Fe	Ar ⁺	"	10 ¹⁵	-	-	-	0%	"	"
Pavlov et al. (ref. 54)	Steel	Ar ⁺	40	9x10 ¹⁷	-	400	600	50%	"	"
Fremlin & Askouri (ref. 67)	WC-CO(H) (N)	He ⁺	3200	1.6x10 ¹⁷	20	1900	2500	31%	"	"
Kant (ref. 44)	Be	B ⁺	90-250	1.2x10 ¹⁷	.005	490	950	98%	"	"
	"	"	"	1.7x10 ¹⁷	.002	570	1520	166%	"	"
	"	"	"	"	.001	540	ND	-	"	"
	"	"	"	"	.005	460	1150	150%	Post 437°C	
	"	"	"	"	.002	330	1830	455%	anneal (1 hr.)	
	"	"	"	"	.001	740	ND	-	(PT)	
	"	"	"	"	.005	400	ND	-	Post 650°C	
	"	"	"	"	.002	310	ND	-	anneal (1 hr.)	
	"	"	"	"	.001	730	ND	-	(PT)	
Suri et al. (ref. 55)	Al	B ⁺	-	10 ¹⁷	.015	100	128	28%		
	"	N ⁺	-	"	"	100	131	31%		
Ti	B ⁺	-	-	"	"	229	330	44%	"	"
"	N ⁺	-	-	"	"	229	297	30%	"	"
364SS	B ⁺	-	-	"	"	296	411	39%	"	"
"	N ⁺	-	-	"	"	296	632	114%	"	"
Boister & Singer (ref. 68)	304SS	N ⁺	80	10 ¹⁷	-	-	-	-	Harder	Abrasive
	C-Steel	N ²⁺	80	"	-	-	-	-	Harder	Wear
	304SS	Ti ⁺	190	"	-	-	-	-	Harder	Technique

ND= No depression

- = Not mentioned in literature

The results obtained using penetration techniques give only a relative increase in hardness because the depth of the implanted layer is usually less than .1 μm . Penetration techniques sample too deeply into the surface. To obtain accurate results with this method, the layer should be at least ten times the depth of penetration. Many investigators feel, however, that under light loads, the results give a measure of relative hardness.

Bolster and Singer [68] have used an abrasive wear technique similar to that developed by Rabinowicz [69] to determine the relative hardness of implanted layers as thin as 25 nm. They found a substantial increase in hardness for N^+ implanted steels, which was accompanied by an increase in the wear resistance by a factor of 100. In this case the hardness decreased to the bulk value at a depth equal to the initial implantation depth. Conversely, N^+ implanted into 304SS wore faster than the unimplanted surface. They attribute this to possible interference with transformation hardening. The observed higher wear rate persisted for depths greater than the implantation depth.

The increase in hardness of the near surface region formed during implantation is not questioned here. However, the information available in the present literature does not explain the mechanism by which hardness is increased or how the increase in hardness, of such a thin layer, affects the

friction coefficient and wear rate. A change in the chemical nature of the surface has been widely observed. Using Auger analysis, ESCA, nuclear reaction analysis, TEM, and the like, various hard compounds have been observed in the implanted layer. Hence some investigators propose that the increase in hardness is attributable to the formation of various hard phases. Others propose that the hardness is increased when the implanted ions occupy substitutional and interstitial sites in the host lattice. Thus substitutional and interstitial hardening is the prevalent hardening mechanism. Last, there are still those who believe that radiation damage increases the hardness by displacing atoms creating vacancies and thus multiplying dislocations. This latter theory is subject to question since some implanted ions have no measurable effect on hardness, friction, or wear.

Although the above theories may explain the mechanisms of hardening, they lack a model and/or evidence that explains how the increase in hardness of the implanted layer can reduce the friction force and wear rate. This information is critical since the increase in hardness of metals can promote crack nucleation and thus wear.

3.4.4 Concluding Remarks

Ion implantation has been shown with numerous ion-substrate combinations to improve the wear properties, to change the friction coefficient, and to increase the hardness of the near surface region of the metal. Although the chemical and mechanical properties of the implanted surface have been investigated, mechanisms describing the effect of ion implantation on friction and wear of metals have not been formulated.

4. FRICTION AND WEAR OF ION-IMPLANTED METALS

4.1 Experimental Procedure

4.1.1 Sample Preparation

Pin-on-disk friction and wear tests were conducted using 3.8 cm to 4.5 cm diameter wear disks, and .635 cm hemispherically tipped pins made from 99.999% pure iron, O.F.H.C. copper, and commercially pure titanium. Both sides of each disk were mechanically polished through 600 grit abrasive paper and subsequently polished with 1.0 μm and .3 μm alumina powder. The ends of the pins were also polished with 1.0 μm and .3 μm alumina. Both pins and disks were freon vapor degreased, rinsed in isopropyl alcohol, dried, annealed in a vacuum furnace at 1073 K for 1 hour, and stored in a vacuum desiccator prior to implantation.

The wear tracks of the implanted and unimplanted disks were sectioned and observed for subsurface deformation. Specimens were nickel plated, and a pie shape section was cut from the worn disk. This section was then mounted in bakelite, giving a tapered section [70] intersecting the wear track at approximately 60 degrees (see Appendix A). This mounting configuration aids in the prevention of surface and subsurface damage which may occur during sample

preparation. Comments by Torrance [71] regarding earlier metallographic procedures used by Jahanmir [5] in preparing micrographs to support the delamination theory were considered when developing this approach. The specimens were then polished using the same procedure described for the friction and wear specimens. They were subsequently freon vapor degreased, rinsed in isopropyl alcohol, dried, etched, and then stored in isopropyl alcohol prior to observation under the SEM. A more detailed description of sample preparation and material can be found in Appendix A.

4.1.2 Ion Implantation

Prior to implantation, the samples were degreased and cleaned with isopropyl alcohol. Implantation of the disks and pins were done either in a Model 200-CF5 Varian/Extrion implanter or a modified Model 200-20A2F Varian/Extrion implanter. The disks and pins were clamped against a freon or water cooled heat sink that kept the samples below 373 K. Both the pins and disks were implanted to a fluence of 10^{17} ions/cm² in a target chamber which was held at about 5×10^{-7} torr. The ion beam was scanned over the specimen surface to give a uniform current density between 4.3 $\mu\text{A}/\text{cm}^2$ to 6.2 $\mu\text{A}/\text{cm}^2$.

The ion-substrate testing combinations are as follows: N^+ into iron, titanium, and copper; Zn^+ into copper; and Al^+ into iron. Although precautions were taken to prevent oxidation of the samples prior to and following implantation, it is inevitable that some oxidation took place at these times. It has not been clarified if the ions were implanted into an oxide layer or if the oxide layer was sputtered off during implantation.

4.1.3 Friction and Wear Measurements

The implanted and unimplanted specimens were tested using the pin-on-disk set-up shown in Figures 4.1.1 and 4.1.2. The specimen (disk) was rotated and the slider (pin) was held stationary in a holder attached to a strain ring. The tangential force was continuously measured by the strain gages and recorder. The recorder was calibrated and balanced prior to all tests.

All tests were conducted at approximately 293 K in an controlled humidity environment. Samples were lubricated with mineral oil, and tested for a duration of 5 hours at a sliding velocity ranging from .5 m/min to 2 m/min (40 rev/min) with a normal load of 400 g unless specified otherwise. Although the sliding velocity varied slightly, Baumvol et al. [33] found the wear rate and friction coefficient to be independent of both sliding velocity

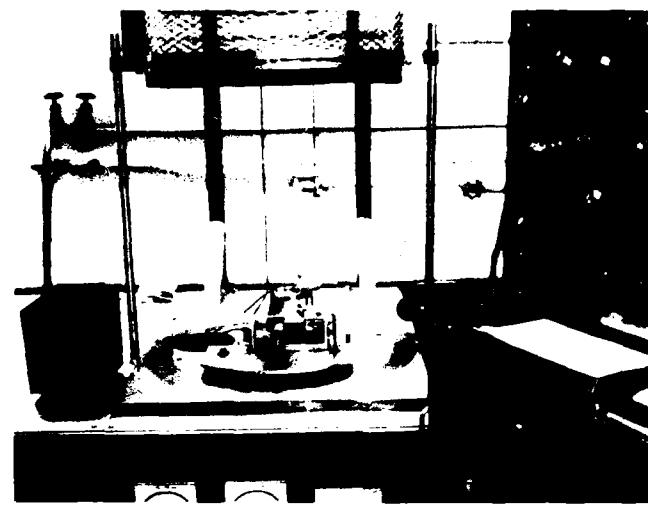


Figure 4.1.1 Friction and wear testing apparatus.

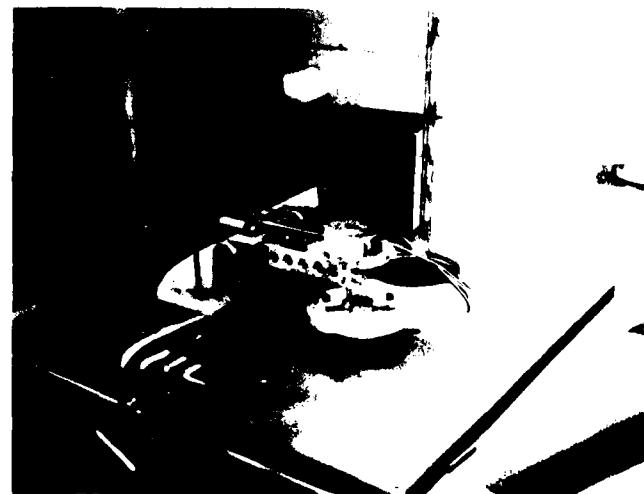


Figure 4.1.2 Pin-on-disk tribotester.

(between 40-60 cm/sec) and the track diameter (between .76-2.24 cm). Every test combination was conducted a minimum of three times and the treatment of the pin surface was the same as the disk surface for all cases.

At the end of the tests, the lubricant and any loose particles were rinsed off in isopropyl alcohol. The track was not scrubbed with tissues in order to avoid damaging the worn surface. The pins and disks were vapor degreased and wear volume was determined. Because of very low wear rates, specimen weight loss could not be used as a measure of wear volume. Therefore, wear volume was estimated from a Talysurf profilometer trace taken perpendicular to the sliding direction for each test. Appendix B gives a detailed description of this method of wear measurement. Wear scars on both the pins and disks were examined using optical and scanning electron microscopy.

4.2 Experimental Results

The friction coefficient of the iron, copper, and titanium system versus sliding distance are shown in Figures 4.2.1, 4.2.2, and 4.2.3, respectively. In the case of N^+ implanted iron, the friction coefficient, $\mu_{N,Fe}$, is almost half that of the unimplanted surface. Similarly, the Al^+ implanted iron reduces the friction coefficient from .128 to .035. After a sliding distance of approximately 200 m the

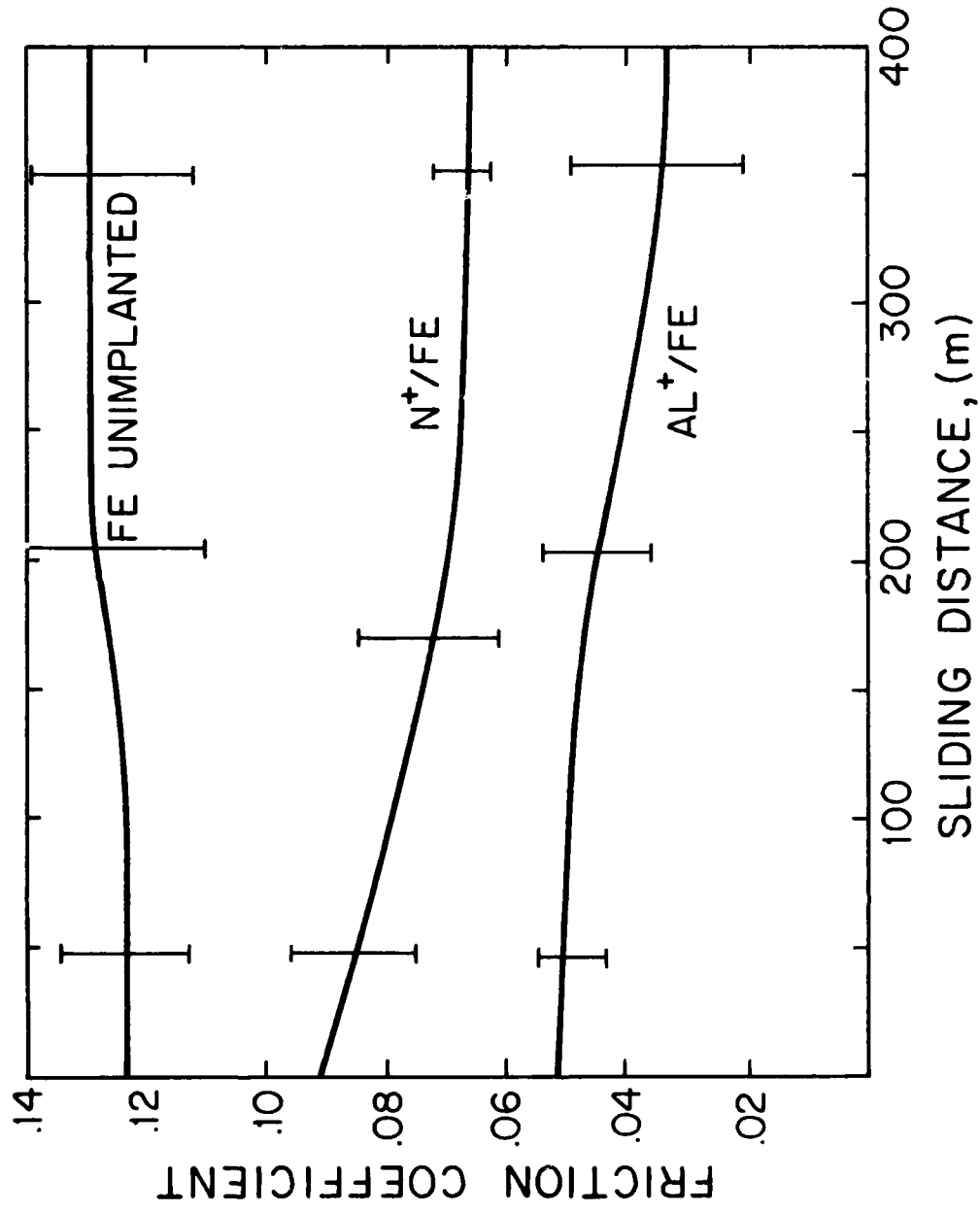


Figure 4.2.1 Change in friction coefficient with sliding distance of unimplanted iron, Al^+ implanted iron, and N^+ implanted iron systems. (lubricated tests in air; load=400g)

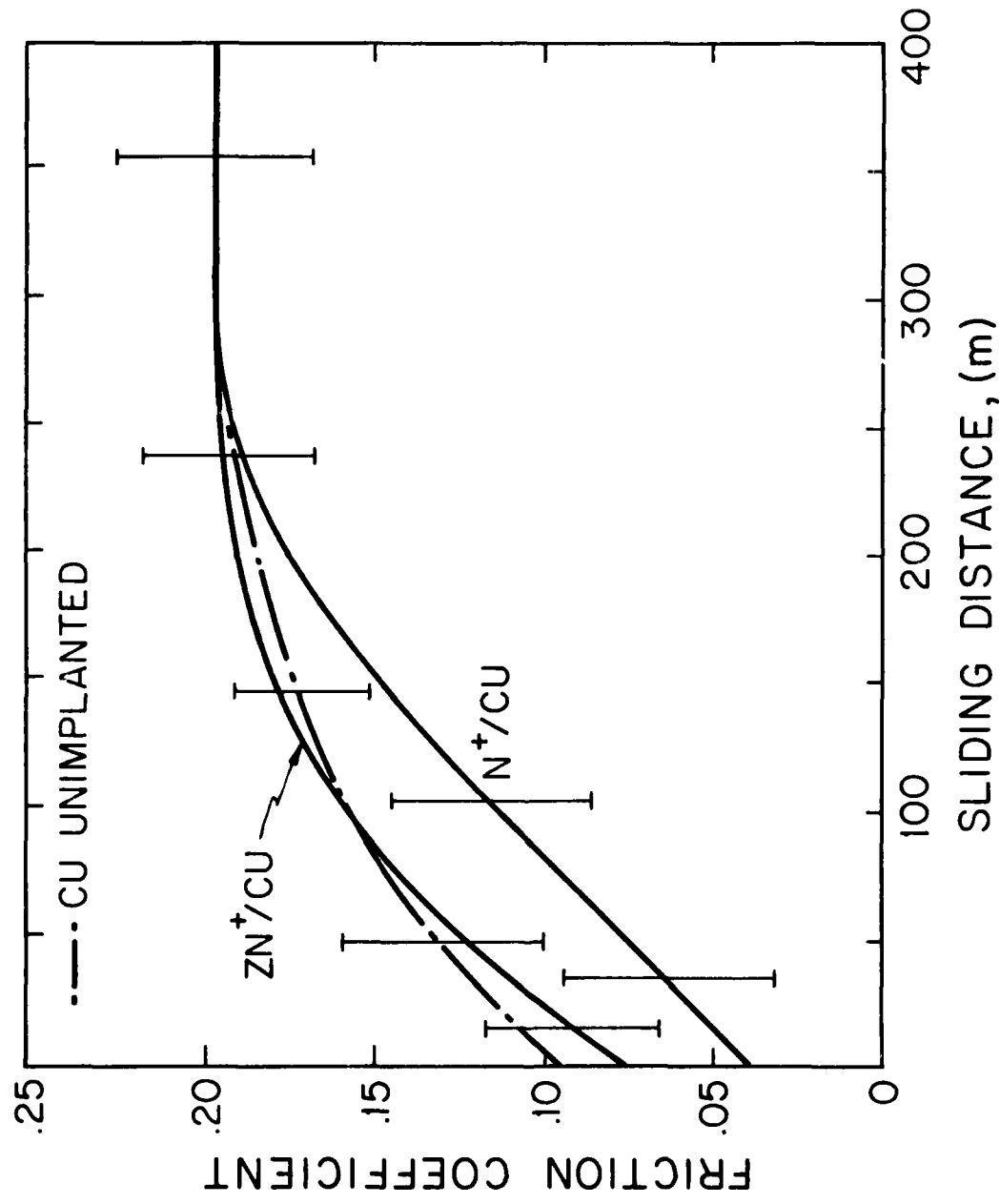


Figure 4.2.2 Change in friction coefficient with sliding distance of unimplanted Cu, Zn^+ implanted Cu, and N^+ implanted Cu systems. (lubricated tests in air; load=400g)

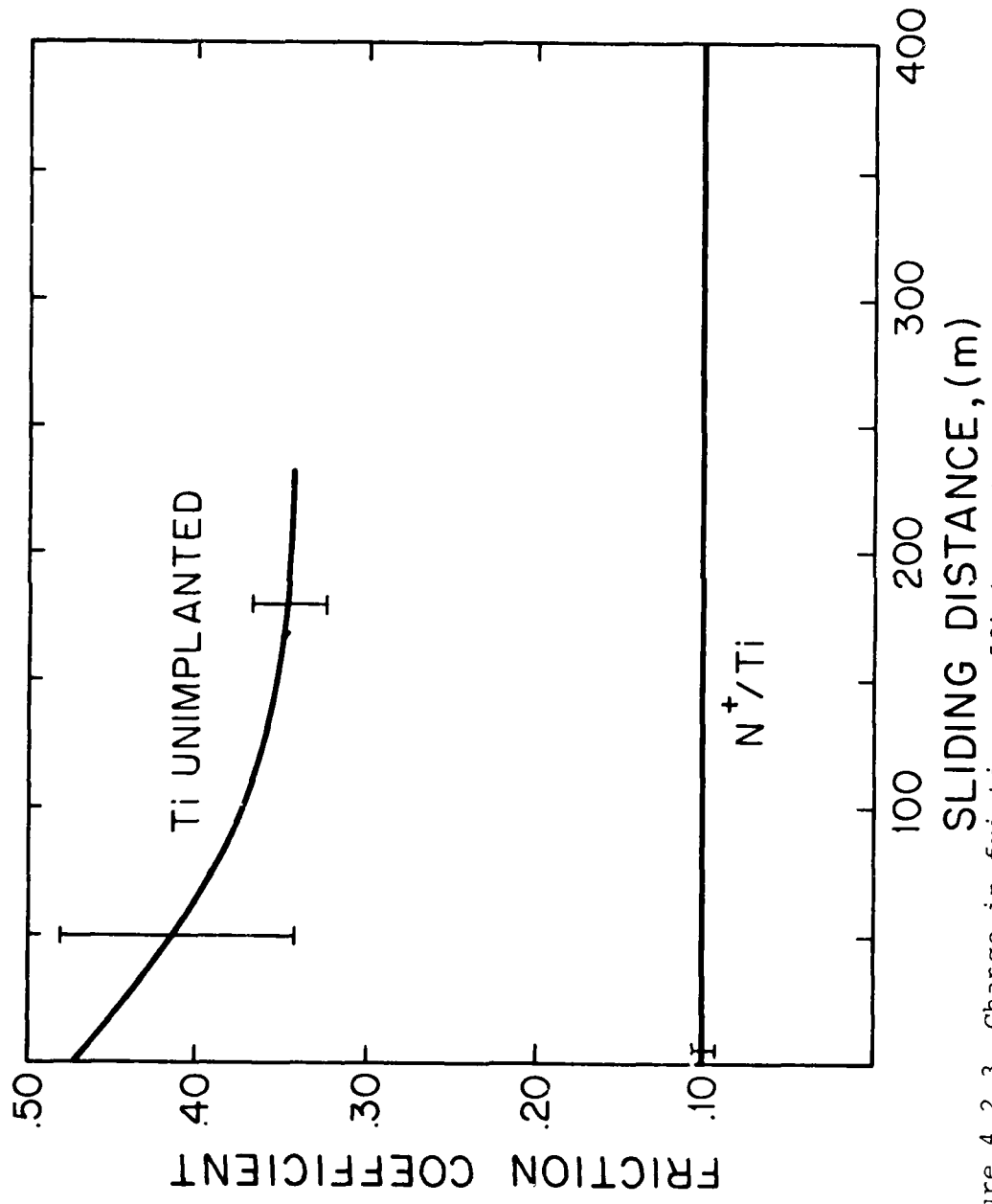


Figure 4.2.3 Change in friction coefficient with sliding distance of unimplanted titanium, and N^+ implanted titanium systems. (lubricated tests in air, Load=400g)

friction coefficient of the implanted surface decreased, while that of the unimplanted surface increased. In the titanium system, the N^+ implanted surface again had a substantially lower friction coefficient, ($\mu_{N,Ti} = .1$), than the unimplanted surface ($\mu_{Ti} = .47$). The reduction in this case is more substantial than in the Al^+ implanted iron system.

Unlike the iron and titanium systems, nitrogen implanted into copper had little effect on the friction coefficient. An initial friction coefficient of .09 increased to that of the unimplanted material after a sliding distance of roughly 100 m. The effect of the Zn^+ implantation into the copper was negligible and μ_{Cu} and $\mu_{Zn,Cu}$ ranged from .06 to .2.

4.2.1 Wear

Selected surface profiles of the unimplanted and implanted specimens are shown in Figures 4.2.4, 4.2.5, and 4.2.6. In the case of iron implanted with N^+ and Al^+ , the wear of the disk was not measurable. However, on the Al^+ implanted disk wide shallow plowing grooves were observed (Figure 4.2.7). Similarly, the N^+ implanted iron occasionally exhibited deep plowing marks (Figure 4.2.8), although "smearing" of material on the surface was more common (Figure 4.2.9). The color of this severely

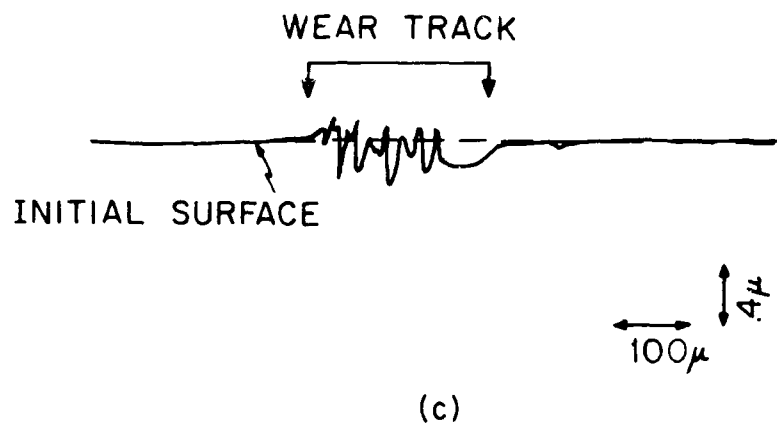
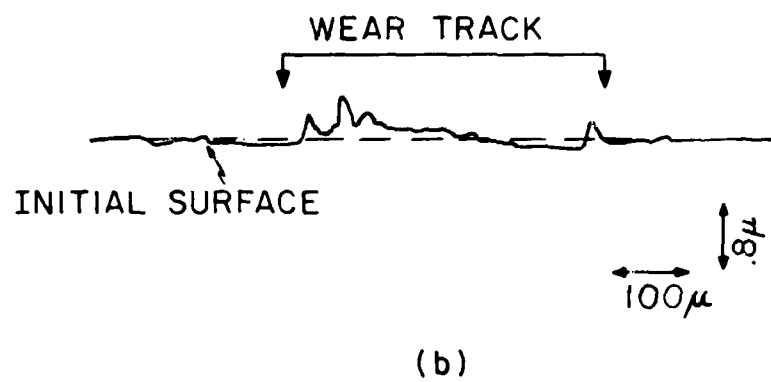
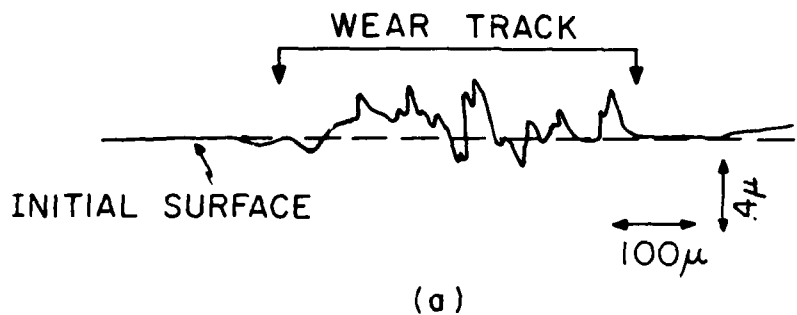


Figure 4.2.4 Typical profiles of worn disk surfaces of a) unimplanted Fe, b) N⁺ implanted Fe, and c) Al⁺ implanted Fe. (lubricated in air; load=400g; 12,000 rev.)

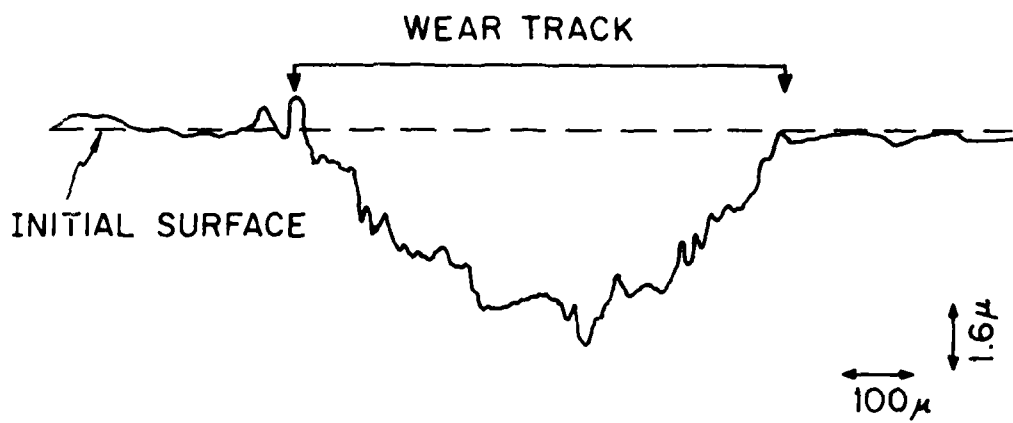


Figure 4.2.5 Typical profile of a worn unimplanted titanium disk surface. (lubricated test in air; load=400g; 2,400 rev.)

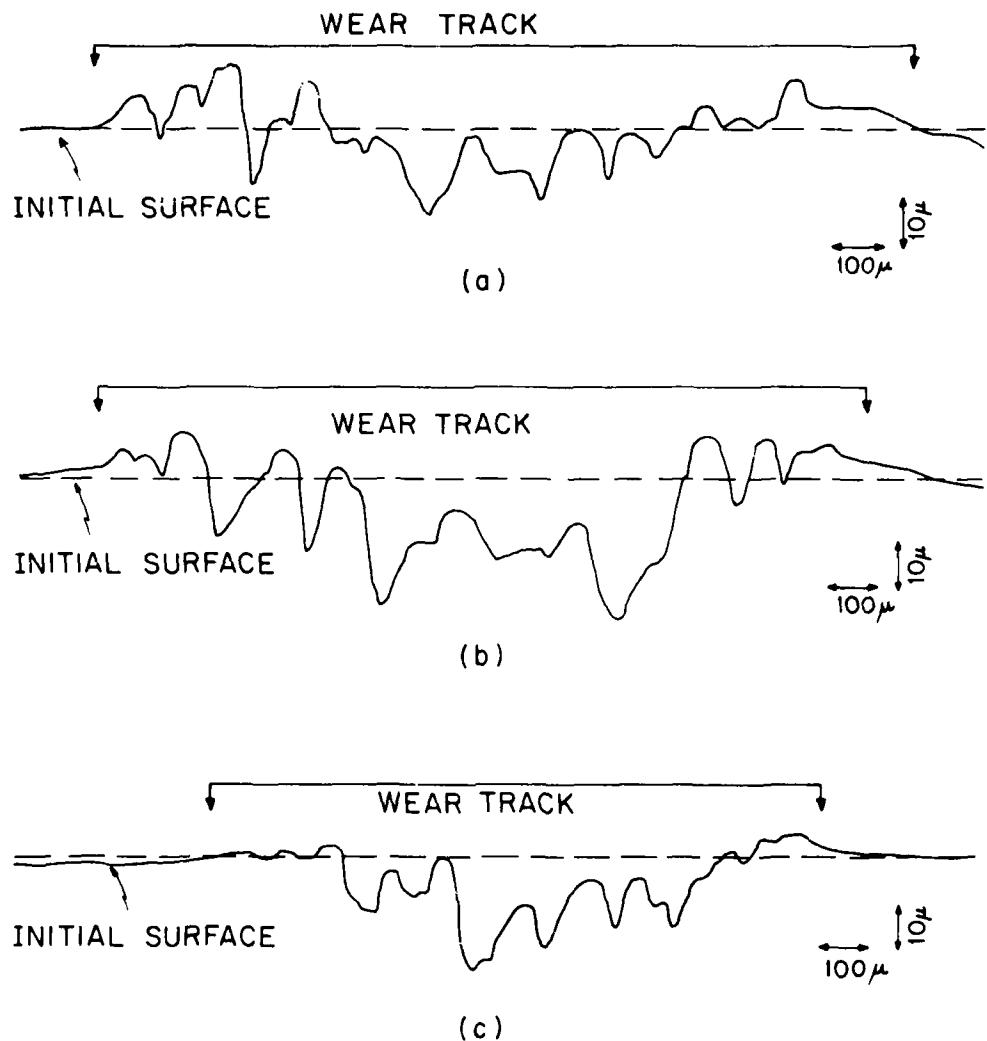


Figure 4.2.6 Typical profiles of worn disk surfaces of a) unimplanted Cu, b) Zn^+ implanted Cu, and c) N^+ implanted Cu. (lubricated tests in air; load=400g; 12,000 rev.)

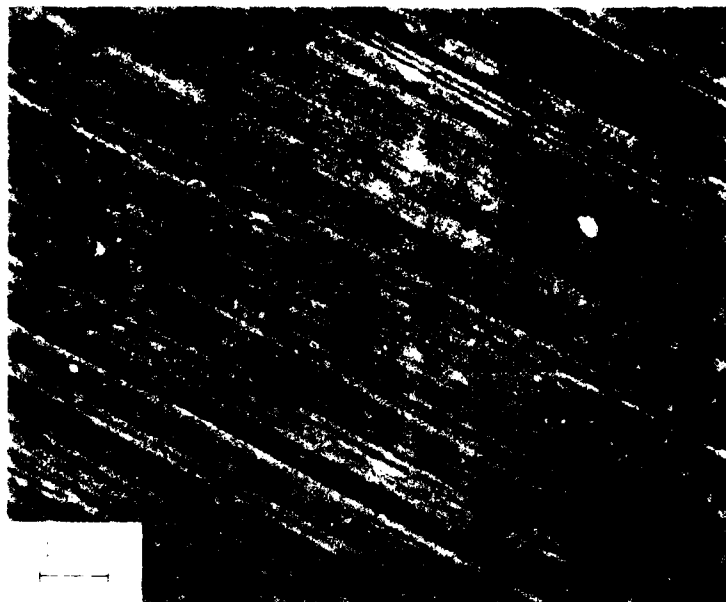


Figure 4.2.7 Typical wear track of Al^+ implanted iron disk; shallow plowing grooves. (lubricated tests in air; load=400g; 12,000 rev.)



Figure 4.2.8 Wear track of M^* in the $100\text{--}1000\text{--}1000\text{--}1000$ grooves.
 (lubricated test in air, $100\text{--}1000\text{--}1000\text{--}1000$ rev.)



Figure 4.2.9 Wear track of N^+ implanted iron disk; severe plastic deformation of a thin layer. (Lubricated test in air; load=400 α ; 12,000 rev.)

plastically deformed layer was lighter than the undisturbed surface, indicating a change in the chemical nature of the layer. The Al^+ implanted iron pin surface wore at the same rate as the unimplanted pin. Only the N^+ implanted iron pin showed a significant decrease in the wear rate. Note that the pin was more severely deformed than the disk since the pin is continuously loaded whereas the disk undergoes cyclic loading.

In contrast to the implanted iron specimens, the unimplanted disk wore at a rate of $7.92 \times 10^{-17} \text{ m}^3/\text{s}$, ($k = 1.04 \times 10^{-10}$)[†]. Even after one revolution of sliding the pin began to wear and numerous plowing grooves were formed on the disk surface (Figures 4.2.10 and 4.2.11)

Titanium implanted with nitrogen showed the greatest improvement in wear resistance. Plowing was undetectable on the surface of the disk using a profilometer. However, when foreign particles or embedded wear particles were present, occasional plowing grooves were visible with the aid of the SEM (Figure 4.2.12). The pins did exhibit small wear scars, but, the scarred area on these pins was almost 15 times smaller than that observed on any other system. Also the scarred surface of the pin was worn smooth with the

[†] The wear coefficient reported is normalized with respect to hardness. That is, the bulk hardness is used in the calculation of k . The actual hardness of such a thin layer is difficult to measure accurately. Only relative hardness values can be obtained.

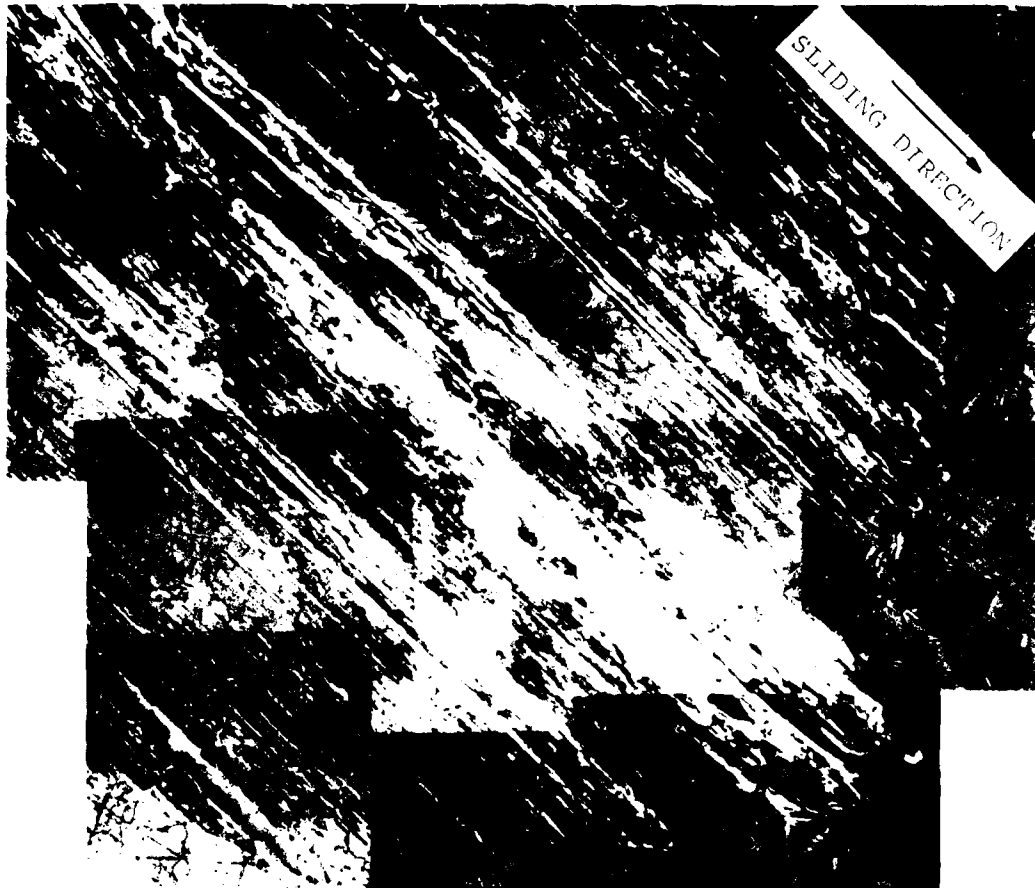


Figure 4.2.10 Typical wear scar on an unimplanted iron pin after 1 revolution of sliding (3 cm). (lubr. test in air; load=400g)



Figure 4.2.11 Typical wear track of an unimplanted iron disk after 1 revolution of sliding. (lubricated test in air; load=400g)

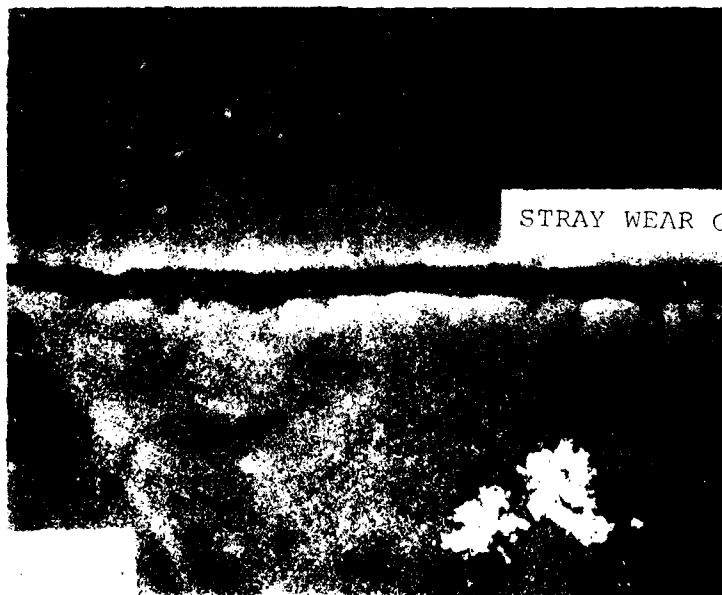


Figure 4.2.12 Typical wear track of N^+ implanted titanium disk. (lubricated test in air; load=400g; 12,000 rev. of sliding)

exception of the surface around the perimeter of the scarred area. In contrast, the unimplanted titanium wore at a rate of $2.8 \times 10^{-14} \text{ m}^3/\text{s}$ ($k=2.2 \times 10^{-7}$). Figure 4.2.13 shows a typical wear track after 12,000 revolutions of sliding.

Like the friction coefficient, the wear rate of Zn implanted copper was not significantly reduced. The implanted disk wore at a rate of $1.64 \times 10^{-14} \text{ m}^3/\text{s}$, ($k=8 \times 10^{-9}$), whereas the unimplanted disk wore at a rate of $8.62 \times 10^{-15} \text{ m}^3/\text{s}$ ($k=4 \times 10^{-9}$), (Figure 4.2.14). The N^+ implanted copper showed reduced wear during the first 200 m of sliding. However, at greater sliding distances, the wear rate approached that of the unimplanted copper (Figure 4.2.15). Other micrographs of the worn pins and disks of various implanted and unimplanted surfaces are shown in Appendix E.

4.2.2 Subsurface Deformation

There was severe plastic deformation below the wear track of both implanted and unimplanted copper specimens. Figure 4.2.16 shows the subsurface for a typical wear groove on the N^+ implanted copper specimen. Similar grooves were observed for the Zn^+ implanted and unimplanted copper wear tracks. Grain size is slightly smaller in the deformed region. In addition, the grains along the worn grooves are elongated and aligned in the direction of sliding, while

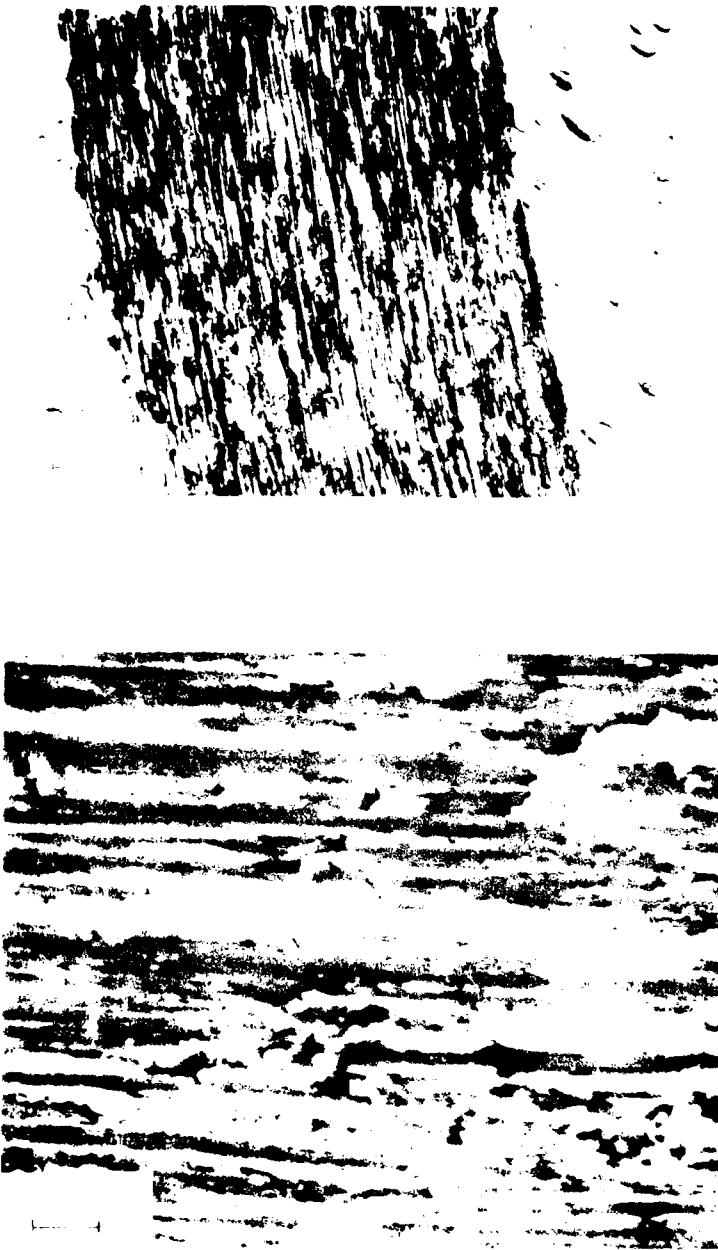


Figure 4.2.13 Typical wear track on an unimplanted titanium disk. (lubricated test in air; load=400 α ; 2,400 rev. of sliding)



Figure 4.2.14 Typical wear track of an unimplanted copper disk. (lubricated test in air; load=400g; 12,000 rev. of sliding)



Figure 4.2.15 Typical wear track of a N^+ implanted copper disk. (lubricated test in air; load=400g; 12,000 rev. of sliding)

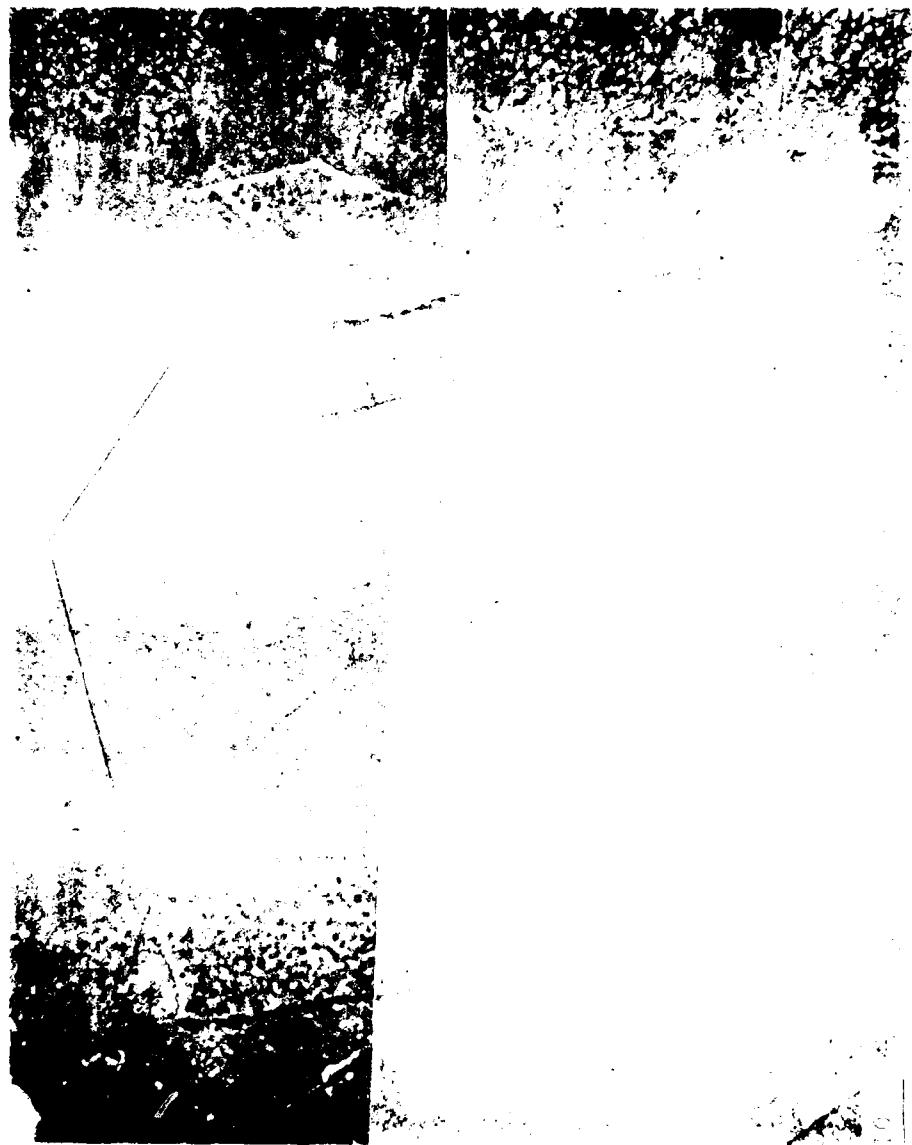


Figure 4.2.16. Sputter etched surface of a 1000 hr. aged, 1000°C. heat treated copper
specimen. (Specimen No. 1000-1, 1/2 in. dia. rev.)

grain boundaries in wear grooves are undetectable due to the severity of the deformation. The grain boundaries are only disturbed very close to the visible wear scar. At only 1 μm below the surface the grains meet at approximately a 120° angle as do annealed, unstressed metals.

The unimplanted iron and titanium specimens showed subsurface deformation similar to that of the copper samples except that the grains did not align themselves along the wear grooves. Figure 4.2.17 shows typical wear grooves for unimplanted iron. Although the grains are not elongated, the grain shape is changed slightly near the edge of the wear track. In this region there is a variation in the 120° angle between adjoining grains. Also, there is a significant change in the size of the grains close to the surface. Slightly below the surface, and often above the depth of the wear groove, the size of the grains returns to the grain size in the undisturbed material.

The subsurface of an unimplanted titanium specimen after only 2,400 passes is shown in Figure 4.2.18. The wear grooves are deepest and most severe in this sample and accordingly subsurface deformation was severe. In contrast, there was no measurable distortion in the grains of the N^+ implanted titanium and iron specimens, nor in Al^+ implanted iron specimens. However, this does not eliminate the possibility that mild subsurface deformation occurred. Mild



Figure 4.2.17 Subsurface Deformation of a typical worn unimplanted iron specimen. (lubricated test in air; load=400g; 12,000 rev.)



Figure 4.2.18 Subsurface deformation of a typical worn unimplanted titanium specimen. (lubricated test in air; load-400; 2,400 rev.)

deformation may not have been severe enough to cause a noticeable change in either the size of the grains or in the grain boundary angles. For example, Figure 4.2.19 shows a wear groove on an Al^+ implanted specimen. The grain is so large that only severe deformation would be measurable.

4.2.3 Chemical Analysis of the Al^+ Implanted Iron Surface

A chemical analysis of the Al^+ implanted iron disk was performed using Secondary Ion Mass Spectroscopy (SIMS) and Ion Scattering Spectroscopy (ISS). The unimplanted disk surface had a corrected Fe/Al ratio of 33.86, using ISS, while the Al^+ implanted iron disk surface had a ratio of 2.88. In the wear groove of the Al^+ implanted iron disk, after 12,000 revolutions of sliding and under a load of 400g in lubricated conditons, the Fe/Al ratio was 6.47. Note that this ratio only gives the relative concentration of aluminum. Their absolute values are meaningless unless compared with the unimplanted sample. Similarly using SIMS, the Fe/Al ratios were 1.52, .866, and 1.21 for the unimplanted iron, the Al^+ implanted iron, and the wear groove on the Al^+ implanted iron disk, respectively.

Aluminum was present on the unimplanted surface because the samples were polished with Al_2O_3 . These results still show, however, that in the wear groove, which is at a depth several orders of magnitude greater than the depth of the



Figure 4.2.19 Subsurface deformation of a typical worn Al³⁺ implanted iron specimen. (lubricated test in air; load=400g; 12,000 rev.)

implanted layer, over 1/3 of the aluminum implanted ions still remained.

5. HYPOTHESIZED MECHANISMS OF FRICTION AND WEAR OF METALS

5.1 FRICTION

For a variety of ion-substrate combinations various investigators observed that implantation to fluences of 10^{17} ions/cm² changes the chemical properties and hardness of the material in the near surface region (refer to chapter 3). The formation of a hard thin layer appears to be related to surface alloying. The existence of alloys in implanted layers has been reported by Poate [58]. He observed the formation of metastable solid solution and amorphous alloys in iron, nickel, and copper of high ion concentration.

Since specific alloyed surfaces show a substantial increase in hardness over the bulk material, it is important to understand how the change of these chemical and mechanical properties affect the tribological behavior of the surface. It is hypothesized that the formation of an alloyed surface, which produces a substantial change in the hardness, minimizes the friction coefficient. This in turn decreases surface and subsurface plastic deformation and thus inhibits the delamination wear process (i.e. crack nucleation caused by large subsurface plastic deformation, crack propagation, and eventual wear particle formation [6]).

The friction force is caused by three mechanisms: plowing of the surface, adhesion at the asperity contacts, and deformation of the surface asperities [10]. The initial dynamic friction for an initially smooth surface, described as stage 2 in the genesis of friction of Chapter 2, is primarily a result of plowing on either the pin or disk surface, except where the surface is free of contaminants. In this case adhesion becomes important. Experiments show that the plowing of the specimen surface results when "embedded wear particles", on the surface of the pin, dig into the specimen surface. The friction force attains a finite value as soon as there is any plastic deformation on either the pin or the disk, which occurs as soon as sliding begins.

The "embedded wear particles" that cause plowing, form as predicted by the delamination theory of wear and as modeled in Figure 5.1.1. Assuming a perfectly smooth surface, surface and subsurface deformation will occur as soon as the counterface slides over the surface. When the subsurface is sufficiently deformed cracks will nucleate below the surface and will eventually extend and propagate if the condition for propagation is satisfied. When these cracked surface layers finally shear to the surface, they will deform the surrounding material and will pile up against an obstacle which may be a surface layer about to delaminate. The resulting wear sheet is the "embedded wear

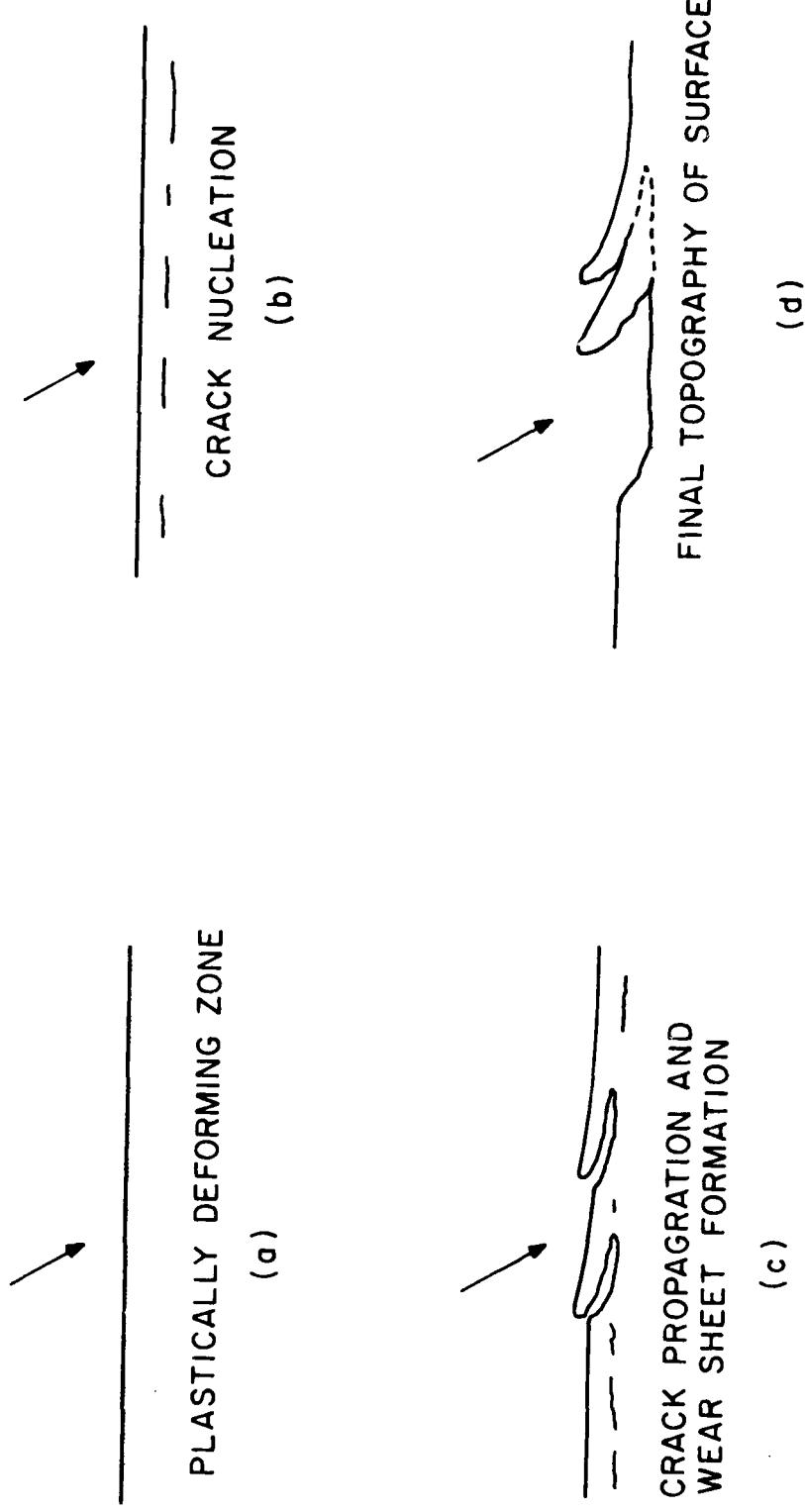


Figure 5.1.1 Schematic representation of wear particle formation during sliding on an initially smooth surface.

particle". Figure 5.1.2 illustrates the formation and piling of several wear sheets on the surface of an Al implanted slider after a sliding distance of several centimeters. These attached wear particles will serve as plowing tools. Note that the wear particle formed may break off from the bulk material and either become embedded elsewhere in the slider or specimen, or remain loose and act as an abrasive wear particle. In either case, it may continue to plow the surface.

If the specimen surface is hard enough to resist the forces exerted by the wear particle without undergoing large plastic deformation, penetration and thus plowing of the sliding surface by this wear particle will be minimized. Also if a smooth, hard, and thick layer can be created on the pin surface, it may not be plowed and hence the wear particles which plow the specimen surface may not exist. The delamination process by which the plowing tools are created will be slowed down, if the deformation of the pin surface can be reduced by a hard layer. If the plowing is reduced on either surface, the friction coefficient will be correspondingly reduced. This process is self perpetuating.

In the case of a "perfectly smooth" hardened pin surface, the specimen surface will not be plowed even if it is "softer" than the pin, if the surface remains perfectly smooth and if no plowing tools are created on the pin



Figure 5.1.2 Wear particle formation on the surface of an Al^+ implanted iron pin after 5 cm of sliding on a lubricated Al^+ implanted disk. (load=400g)

surface. When the surface is smooth, the stress is distributed over a larger contact area, whereas if the pin is rough the stress is distributed over a smaller contact area (a few high points). Hence the stresses are greater at these high points than in the former case. Conversely, if the hard layer is not smooth, the ridges on the surface will act as plowing tools and severe plowing of the specimen surface and thus high friction will result. Note that with an unhardened surface, the initial roughness will be of little importance in affecting friction and wear since particles which plow the surface will be readily formed after a short sliding distance. The initial friction coefficient may be slightly higher for the first few passes, since asperity deformation will be more predominant for a rough surface than a smooth one. This effect, however, will only be important for short sliding distances.

To recapitulate, if ion implantation creates a surface alloy which is harder than the bulk material, plowing may be reduced which leads to a reduction in the friction coefficient. We will see in the next section that the decrease in the friction coefficient is the governing factor in reducing wear.

Three different properties of the pin riding on a smooth specimen are considered.

- A hard rough pin

- A hard, smooth pin
- A soft, smooth or rough pin

In the first case, the plowing "tools" which cause plowing will be present, hence plowing may be severe on the specimen surface if it cannot resist the penetrating forces. With a smooth hard pin, however, plowing will be minimized on both surfaces, hence a low friction coefficient will result. In the latter case, even a smooth pin can cause plowing due to embedded wear particles which are formed by a pile-up process of delamination wear particles. Consequently the friction coefficient is high.

5.2 Wear: Subsurface Deformation

We saw in the previous section that the friction coefficient can be lowered in the presence of a hardened layer. It is important to note that plowing and friction are related phenomena. Friction is always present when plowing occurs. However, plowing does not have to occur when there is friction, although in most situations it does. Also, a reduction in the friction coefficient does not necessarily imply a decrease in plowing and vice versa. However, we will see that a decrease in the friction coefficient does necessarily imply a reduction in wear.

AD-101 173

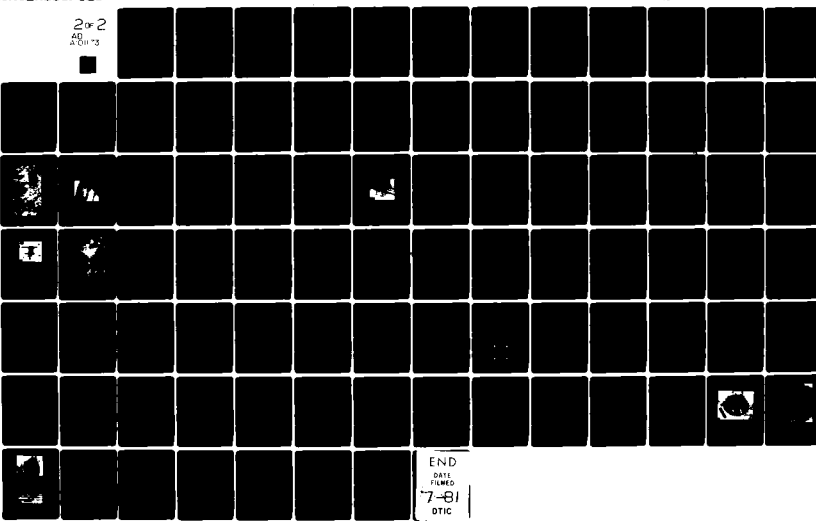
MASSACHUSETTS INST OF TECH CAMBRIDGE LAB FOR MFG AND ETC F/6 11/6
THE EFFECTS OF ION IMPLANTATION ON FRICTION AND WEAR OF METALS. (U)
MAY 81 N P SUM, S R SHEPARD

N00014-80-C-0255

NL

UNCLASSIFIED

2 of 2
AD-101-3



END
DATE FILMED
7-81
DTIC

As stated in Chapter 3, subsurface deformation is necessary for the delamination process to occur. Hence, the state of stress in and below the implanted layer must be investigated to see how ion implantation affects wear. An approximate solution for an isotropic linear elastic semi-infinite solid was modeled using the finite element method (FEM). This method of solution for the plane strain case, is described in Appendix C. Values of σ_{xx} , σ_{yy} , τ_{xy} and τ_{max} are determined for steady state sliding of an isotropic linear elastic semi-infinite solid against a rigid stationary plane as sketched in Figure 5.2.1. The maximum applied normal and tangential stresses at the contact are designated as p_0 and q_0 , respectively. The ratio of the tangential stress to the normal stress is defined as the friction coefficient, and half the contact length is defined by a length a . In order to describe the state of stress, p_0 and q_0 must be specified. E_1 and E_2 are Young's modulus for the thin layer of thickness d , and for the bulk material, respectively.

For the following analysis E_1/E_2 is approximately 2.5, and d is the thickness of the implanted layer (30). The contact length is assumed to be 20 μm . Using the FEM the following parameters will be investigated:

1. The effect of thickness of a hard layer on subsurface deformation.

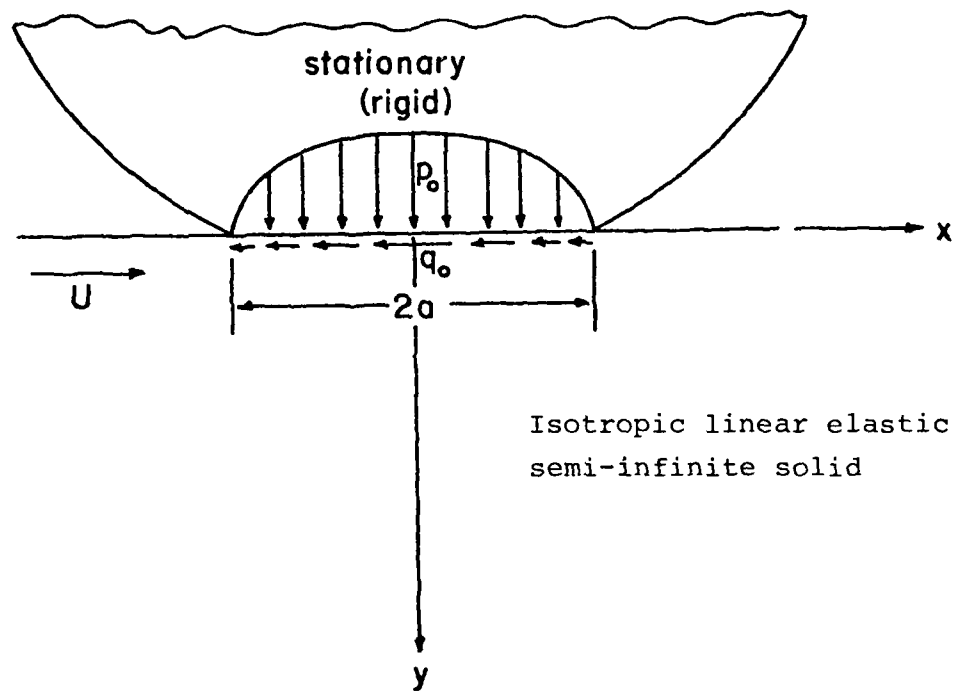


Figure 5.2.1 Model of a contact between a stationary rigid asperity and a sliding isotropic linear elastic semi-infinite solid. (reference 5)

2. The effect of the friction coefficient on subsurface deformation.
3. The effect of lowering p_0 on subsurface deformation

Before considering each of the above parameters, a condition for yielding must be defined in order to interpret the results. Using Tresca's yield criterion, yielding is predicted to occur when:

$$\sigma_y = \sigma_1 - \sigma_2 = \frac{H}{3} = 2k \quad \text{eq. (5.2.1)}$$

where:

k = shear stress at yielding

σ_y = yield stress of the bulk material

H = hardness of the bulk material

σ_1, σ_2 = principal stresses, where $\sigma_1 > \sigma_2$

When equation 5.2.1 is satisfied the condition for yielding is satisfied. Since the plastic deformation will alter the stress field obtained for an elastic solid, the solution is only approximate. However, it may provide a useful insight to the region of elasto-plastic transition.

1. The effect of a hard thin layer on subsurface deformation:

Figures 5.2.2-5.2.5, respectively, show the steady state σ_{xx} , σ_{yy} , τ_{xy} , and τ_{max} components for a $.2 \mu\text{m}$

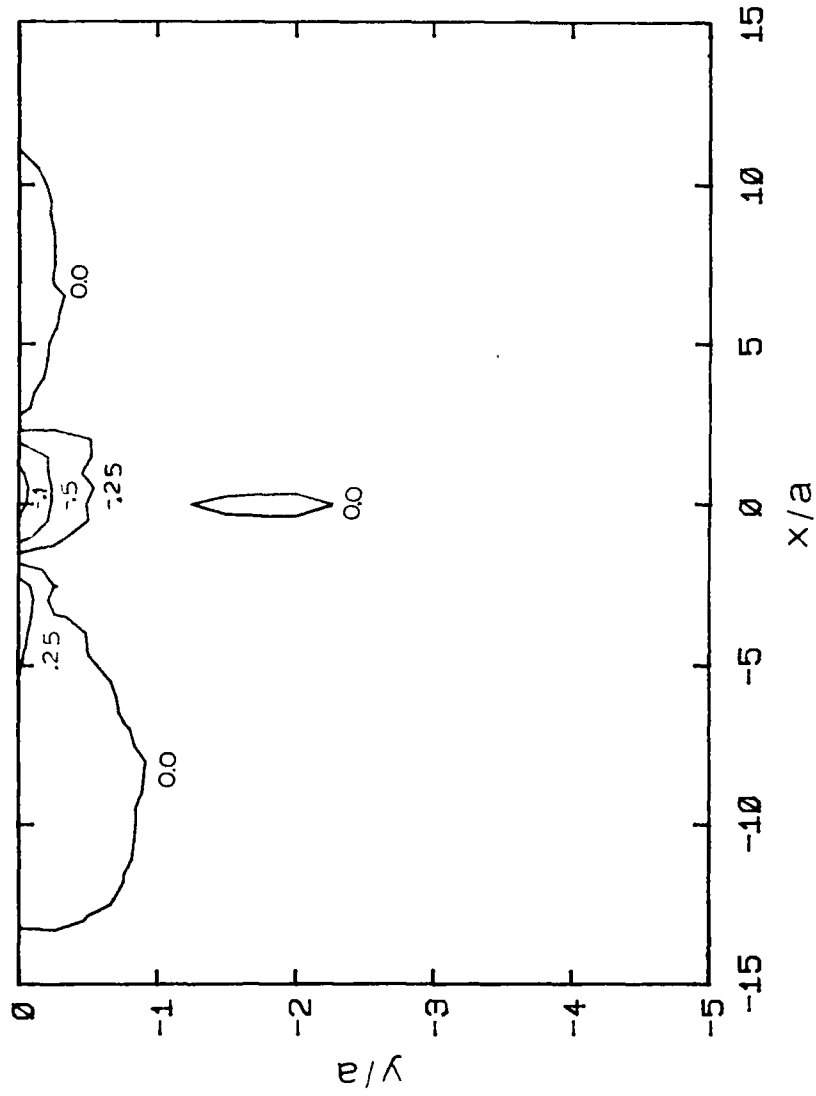


Figure 5.2.2 The steady state σ_{xx} component of the state of stress at different depths normalized with respect to the maximum applied normal stress, P_0 , for contact length, $a=20\mu\text{m}$, $\mu=1$, $E_1/E_2=2.5$, and $d=2\mu\text{m}$.

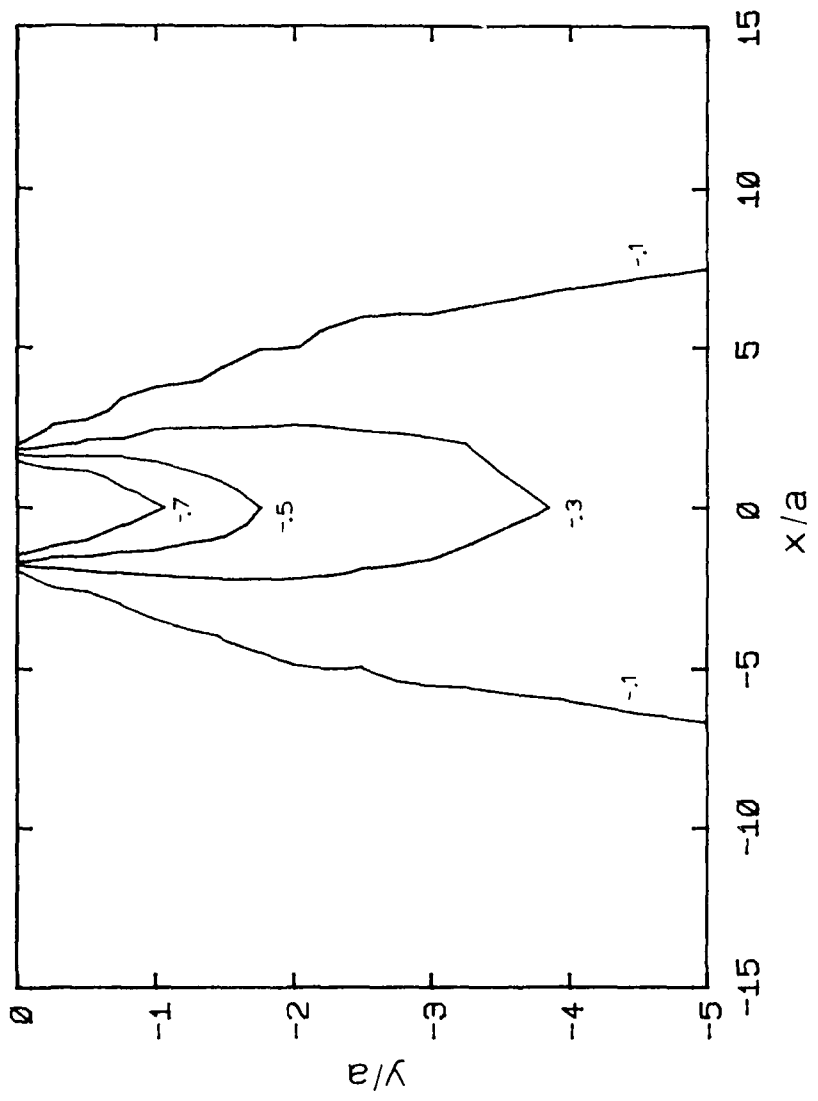


Figure 5.2.3 The steady state σ_{yy} component of the state of stress at different depths normalized with respect to the maximum applied normal stress, p_0 , for contact length, $a = 20\mu\text{m}$, $\mu = .1$, $E_1/E_2 = 2.5$, and $d = 2\mu\text{m}$.

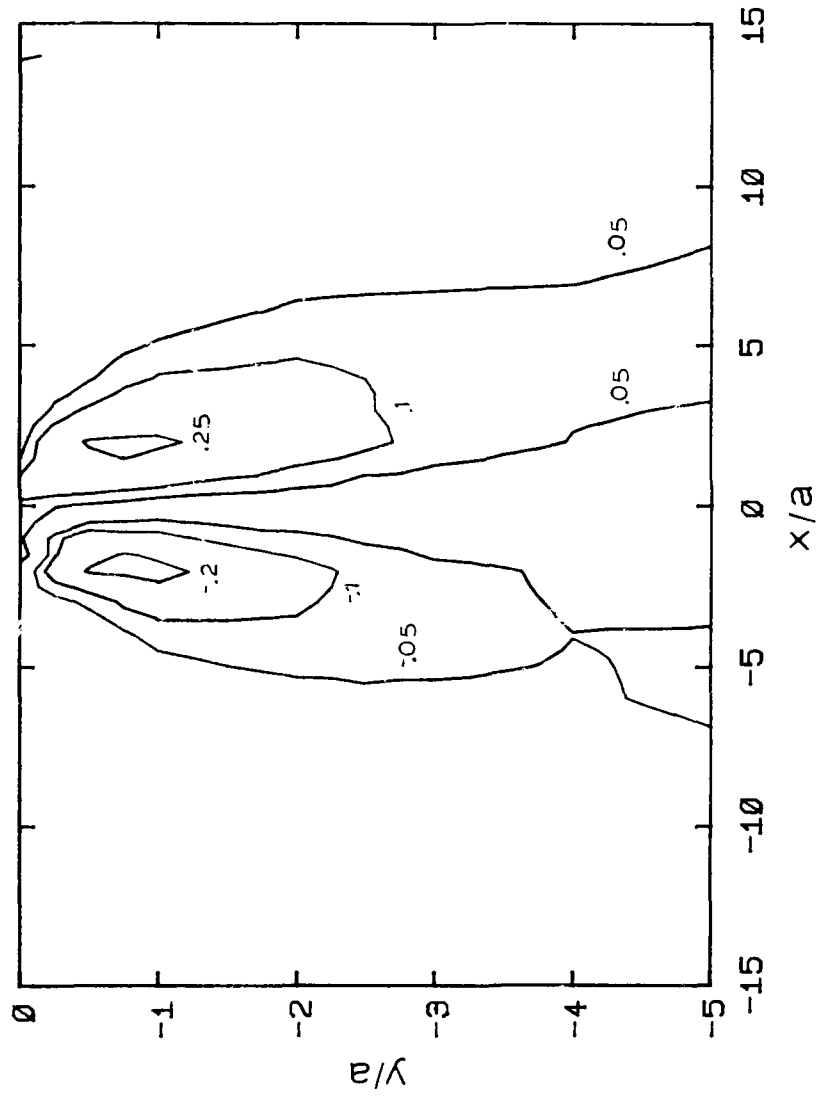


Figure 5.2.4 The steady state τ_{xy} component of the state of stress at different depths normalized with respect to the maximum applied normal stress, P_0 , for contact length, $a=20\mu\text{m}$, $\mu=0.1$, $E_1/E_2=2.5$, and $d=2\mu\text{m}$.

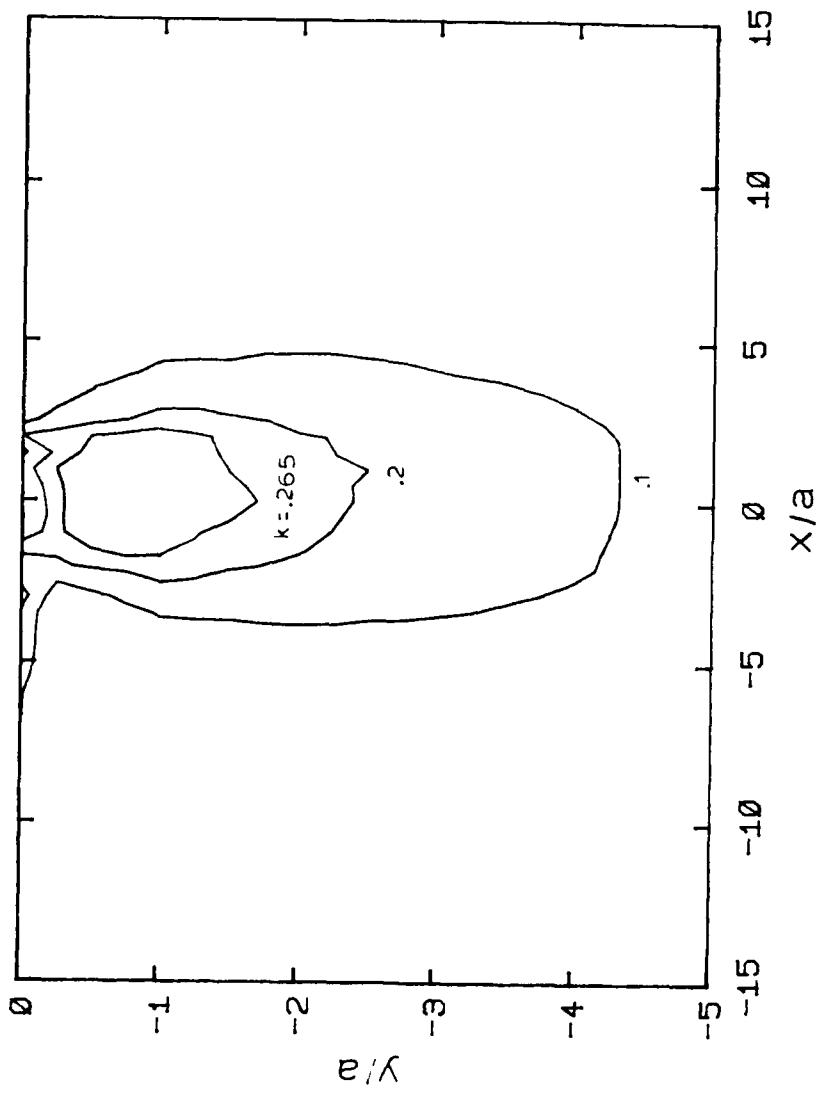


Figure 5.2.5 The steady state τ_{\max} component of the state of stress at different depths normalized with respect to the maximum applied normal stress, p_0 , for contact length, $a=20\mu\text{m}$, $\mu=1$, $E_1/E_2=2.5$, and $d=2\mu\text{m}$.

thick hard layer. The stresses have been normalized with respect to the maximum applied normal stress, p_0 , where

$$p_0 = \frac{4}{\pi} H$$

E_1/E_2 is approximately 2.5 and the friction coefficient is 0.1. Figures 5.2.6-5.2.9 show the same steady state σ_{xx} , σ_{yy} , τ_{xy} , and τ_{max} components with the same parameters except now for a hard layer depth of 1 μm , a depth 5 times larger than in the previous set of figures. Comparing these two sets of figures, the hard layer does not decrease the area at which the yield criterion is satisfied ($k > .265$) nor are the σ_{xx} , σ_{yy} , and τ_{xy} components significantly different. Even if no hardened layer is present i.e. $E_1/E_2=1$, the components of stress do not vary significantly (Figures 5.2.10, 5.2.11). Thus it appears that for a constant set of parameters, in particular a constant friction coefficient, the presence of a thin hard layer will not alter the wear rate since the subsurface stresses are not noticeably affected.

Note that this model is highly idealized since as seen in previous sections, a change in the thickness of the hardened layer can decrease plowing and hence friction. Despite this deficiency, the model does

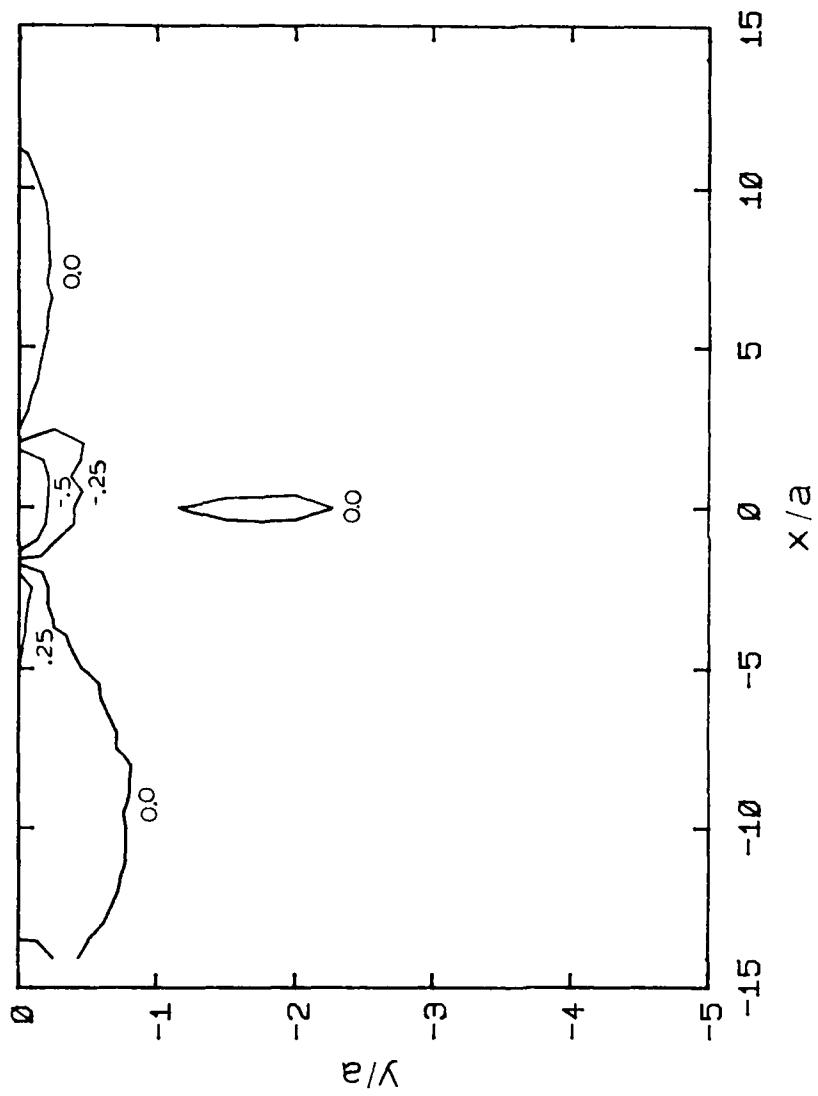


Figure 5.2.6 The steady state σ_{xx} component of the state of stress at different depths normalized with respect to the maximum applied normal stress, P_0 , for contact length, $a=20\mu\text{m}$, $\mu=.1$, $E_1/E_2=2.5$, and $d=1\mu\text{m}$.

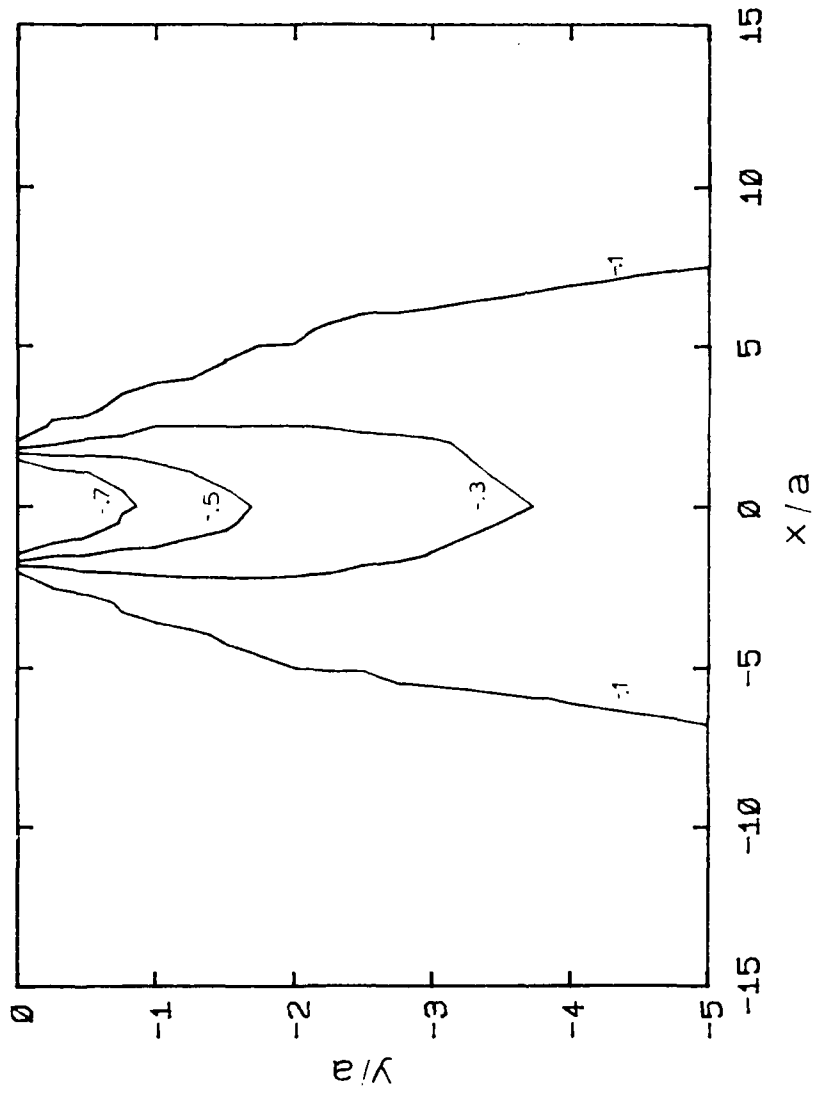


Figure 5.2.7 The steady state σ_{yy} component of the state of stress at different depths normalized with respect to the maximum applied normal stress, p_o , for contact length, $a=20\mu\text{m}$, $\mu=.1$, $E_1/E_2=2.5$, and $d=1\mu\text{m}$.

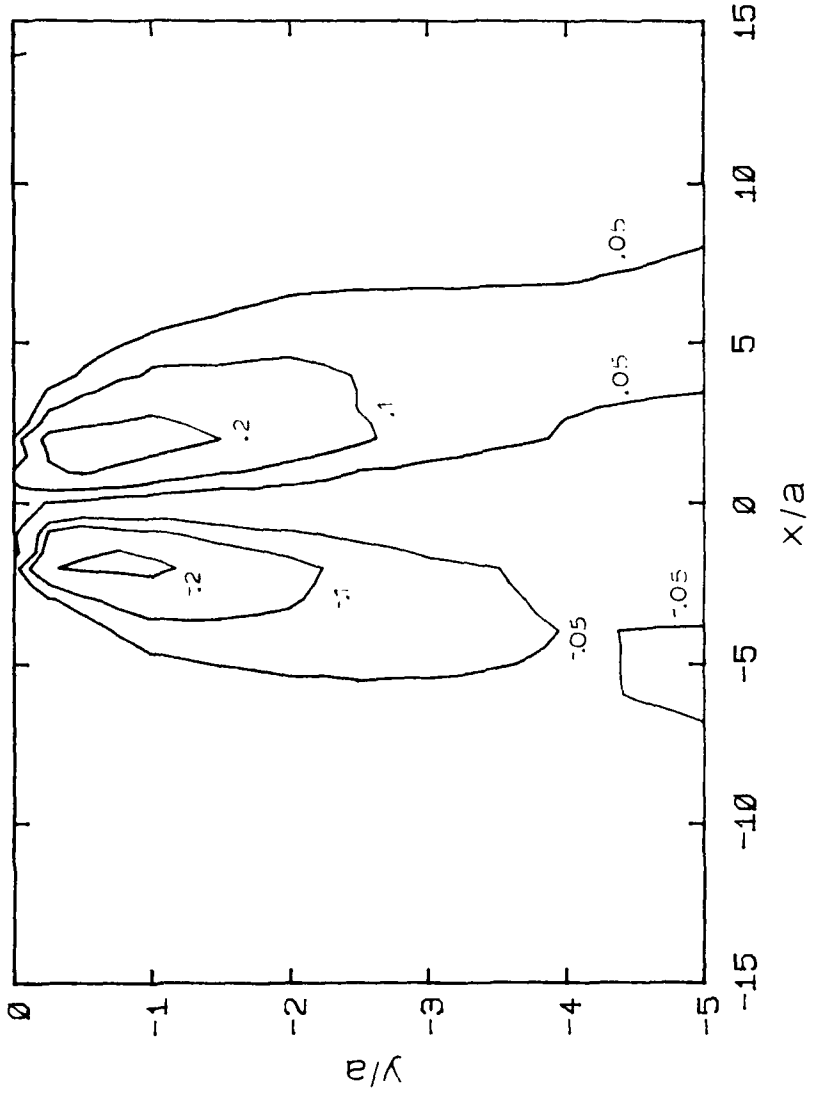


Figure 5.2.8 The steady state τ_{xy} component of the state of stress at different depths normalized with respect to the maximum applied normal stress, p_0 , for contact length, $a=20\mu\text{m}$, $\mu=0.1$, $E_1/E_2=2.5$, and $d=1\mu\text{m}$.

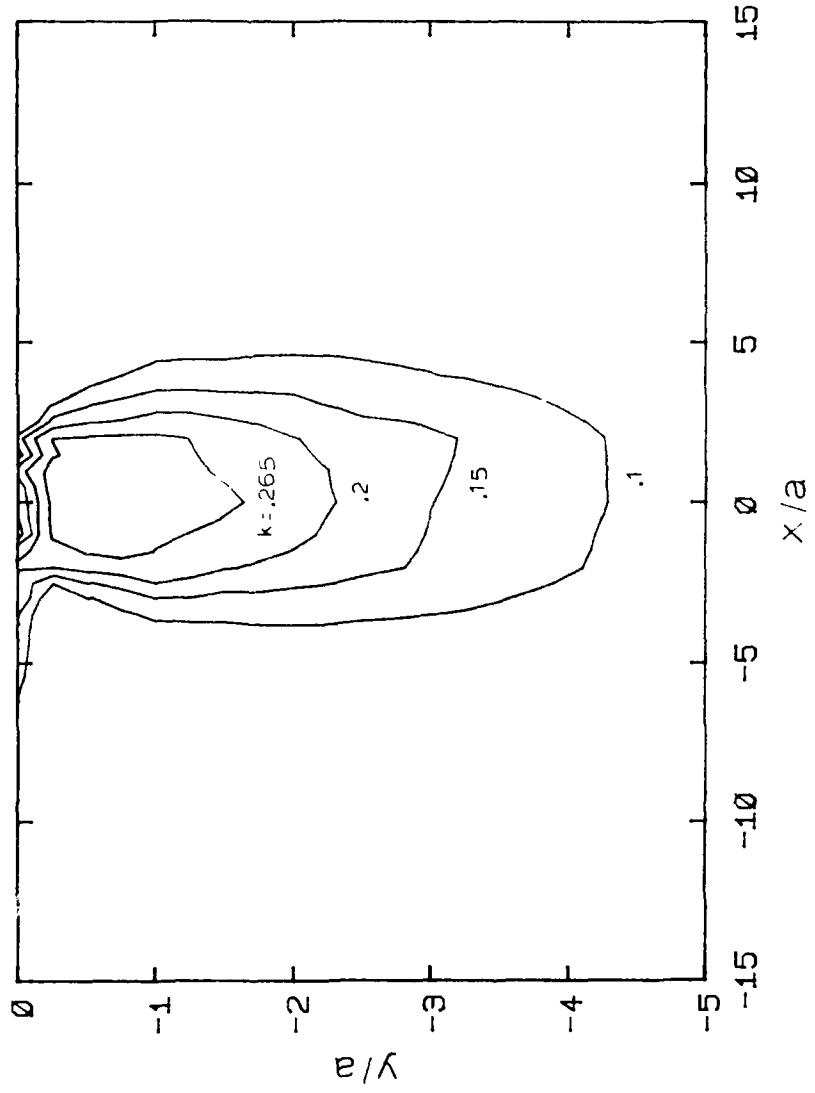


Figure 5.2.9 The steady state τ_{\max} component of the state of stress at different depths normalized with respect to the maximum applied normal stress, p_0 , for contact length, $a=20\mu\text{m}$, $\mu=.1$, $E_1/E_2=2.5$, and $d=1\mu\text{m}$.

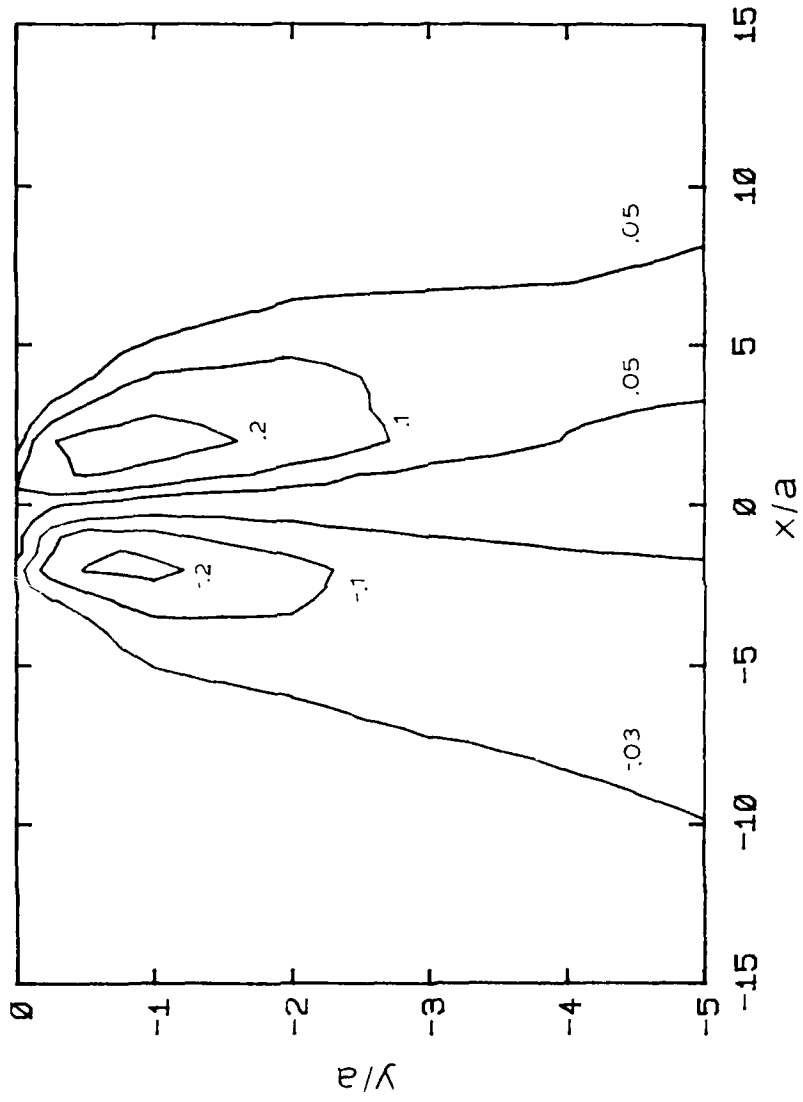


Figure 5.2.10 The steady state τ_{xy} component of the state of stress at different depths normalized with respect to the maximum applied normal stress, P_0' , for contact length, $a=20\mu\text{m}$, $\nu=.1$, $E_1/E_2=1$, and $d=.2\mu\text{m}$.

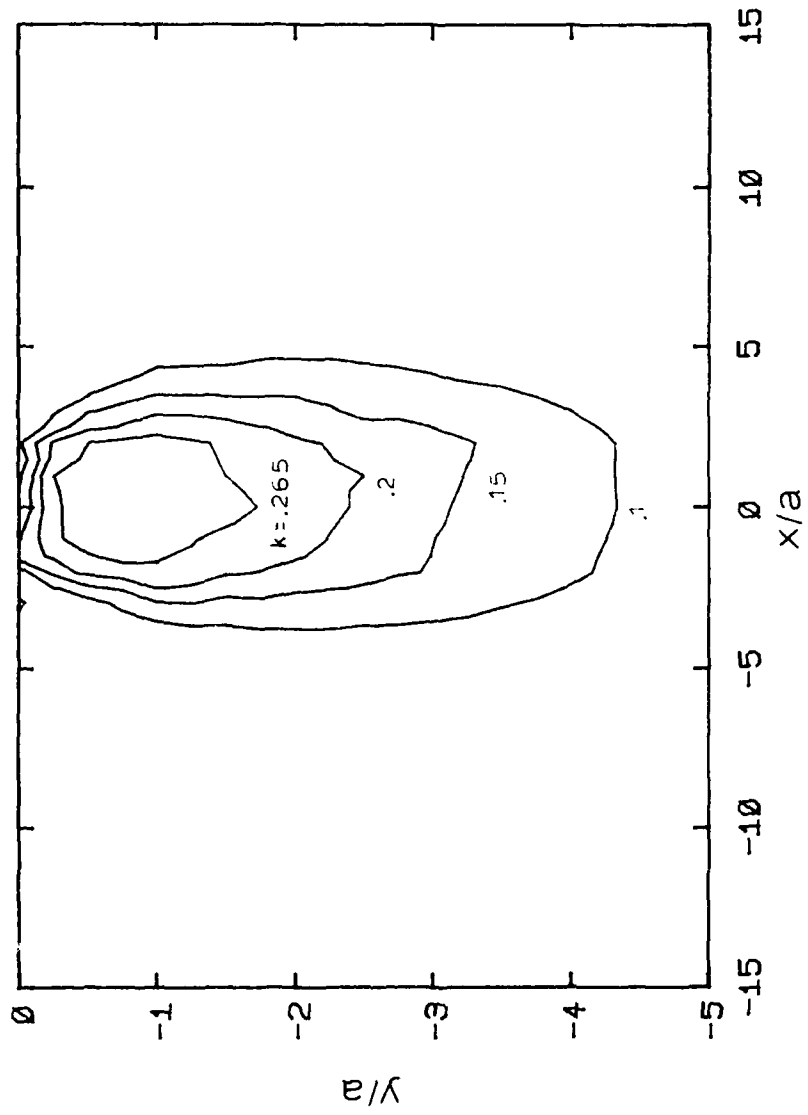


Figure 5.2.11 The steady state τ_{\max} component of the state of stress at different depths normalized with respect to the maximum applied normal stress, p_0 , for contact length, $a=20\mu\text{m}$, $\mu=1$, $E_1/E_2=1$, and $d=2\mu\text{m}$.

illustrate the inability of a very thin layer alone to alter subsurface deformation.

2. The Effect of the friction coefficient on subsurface deformation:

Figures 5.2.4, 5.2.5 and Figures 5.2.12, 5.2.13 show the τ_{xy} and τ_{max} stress components for $\mu=.1$ and $\mu=.47$, respectively (σ_{xx} and σ_{yy} components for each remaining solution in this section can be found in Appendix D). All other parameters remain constant between the two sets. When the friction coefficient is increased to .47 the stresses change substantially. The yield criterion is satisfied at the surface and to a depth of 20 μm . When $\mu=.1$, the yield condition is only satisfied in a small region below the surface. Also as the friction coefficient is increased the τ_{xy} component becomes substantially larger and the maximum stress shifts toward the surface. The σ_{xx} and σ_{yy} components are also increased. Thus, changing only the friction coefficient can substantially reduce subsurface deformation and stresses, and hence can reduce wear.

3. The effect of reducing p_0 on subsurface deformation:

The τ_{xy} stress component and maximum shear component for $p=1/2p_0$ and $p=3/4p_0$ are shown in Figures 5.2.14, 5.2.15 and Figures 5.2.16, 5.2.17, respectively. The

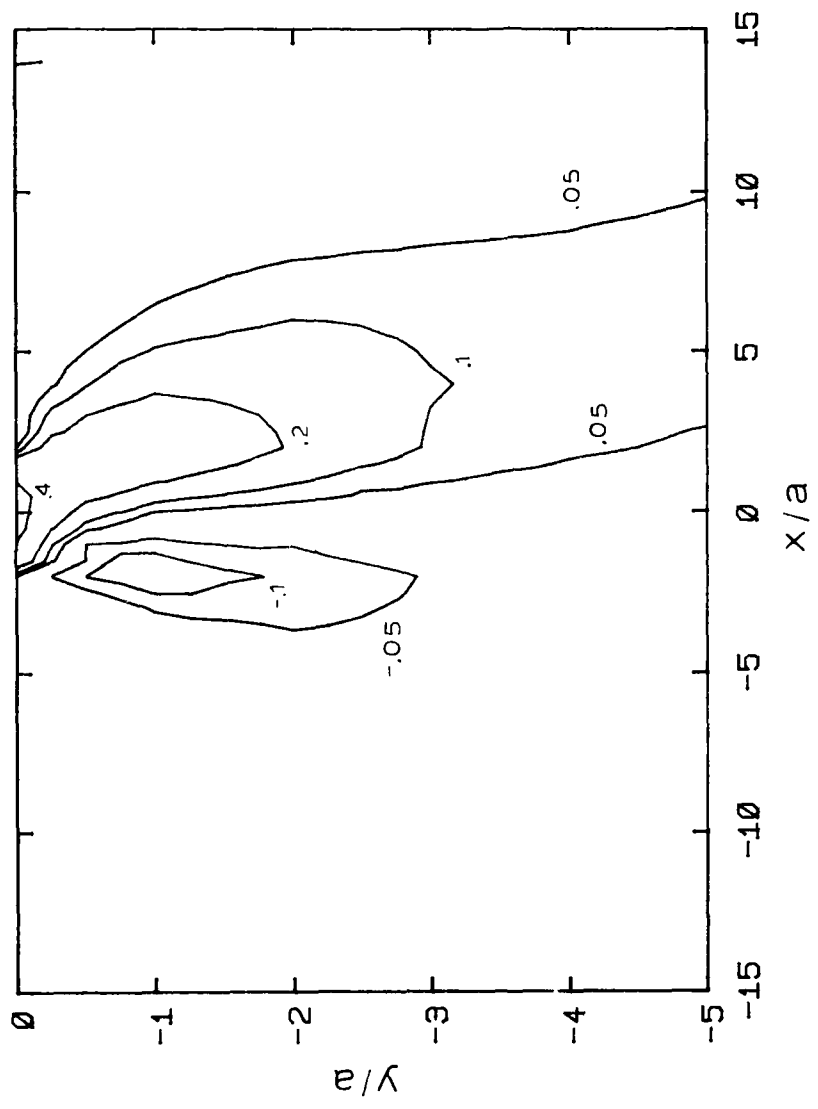


Figure 5.2.12 The steady state τ_{xy} component of the state of stress at different depths normalized with respect to the maximum applied normal stress, p_0 , for contact length, $a=20\mu\text{m}$, $\mu=.47$, $E_1/E_2=2.5$, and $d=.2\mu\text{m}$.

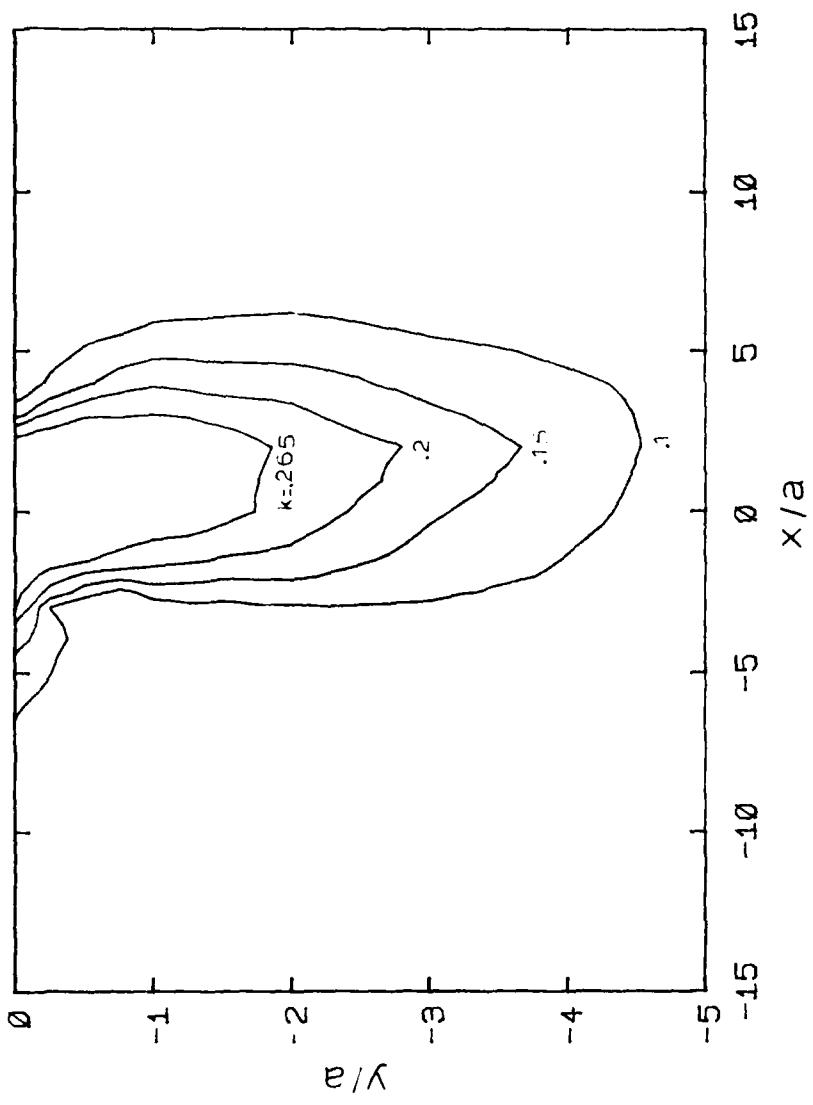


Figure 5.2.13 The steady state τ_{\max} component of the state of stress at different depths normalized with respect to the maximum applied normal stress, p_0 , for contact length, $a=20\mu\text{m}$, $\mu=.47$, $E_1/E_2=2.5$, and $d=.2\mu\text{m}$.

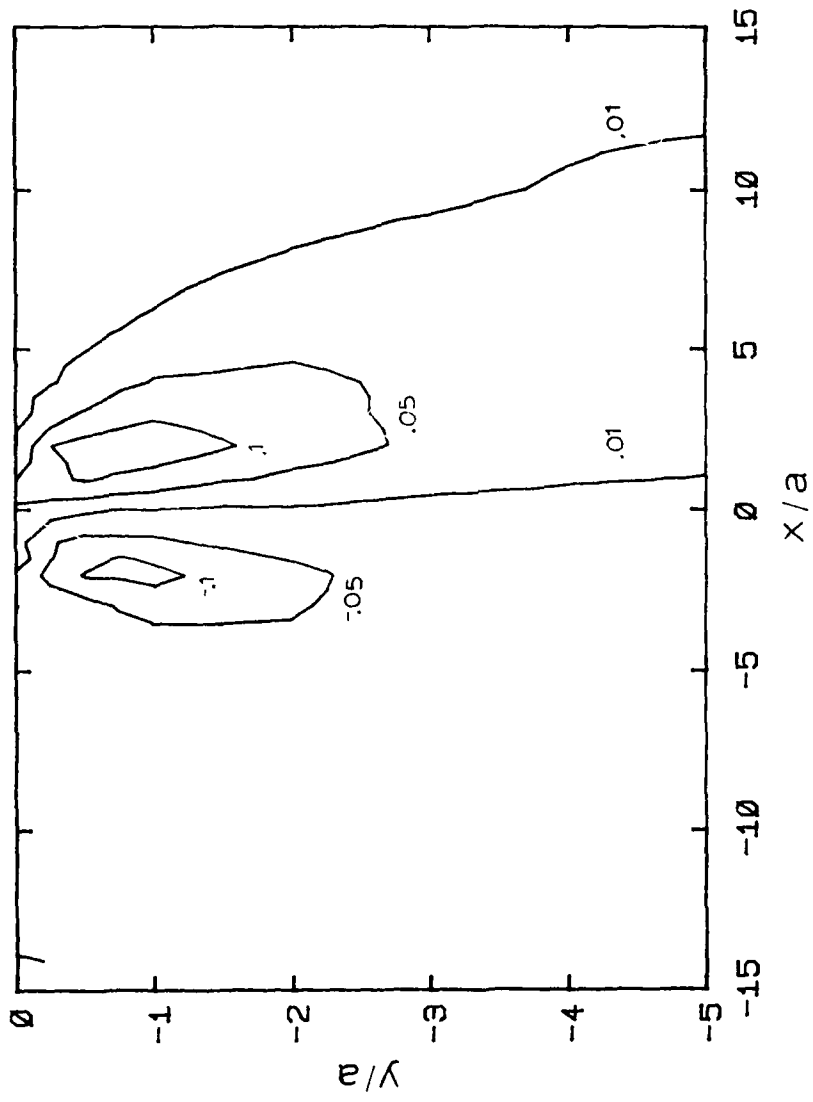


Figure 5.2.14 The steady state T_{xy} component of the state of stress at different depths normalized with respect to the maximum applied normal stress, p_o , for $p=1/2p_o$, $a=20\mu\text{m}$, $\mu=.1$, $E_1/E_2=2.5$ and $d=.2\mu\text{m}$.

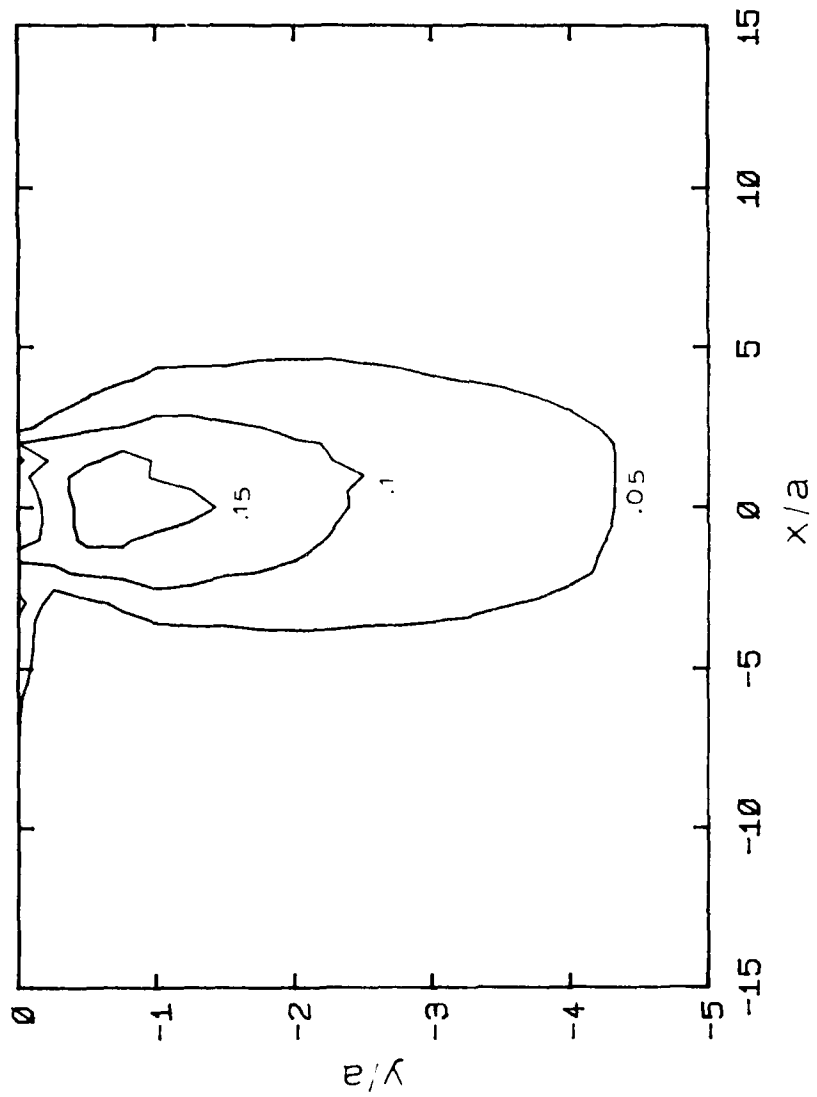


Figure 5.2.15 The steady state T_{\max} component of the state of stress at different depths normalized with respect to the maximum applied normal stress, p_0 , for $p=1/2p_0$, $a=20\mu\text{m}$, $\nu=.1$, $E_1/E_2=2.5$, and $d=.2\mu\text{m}$.

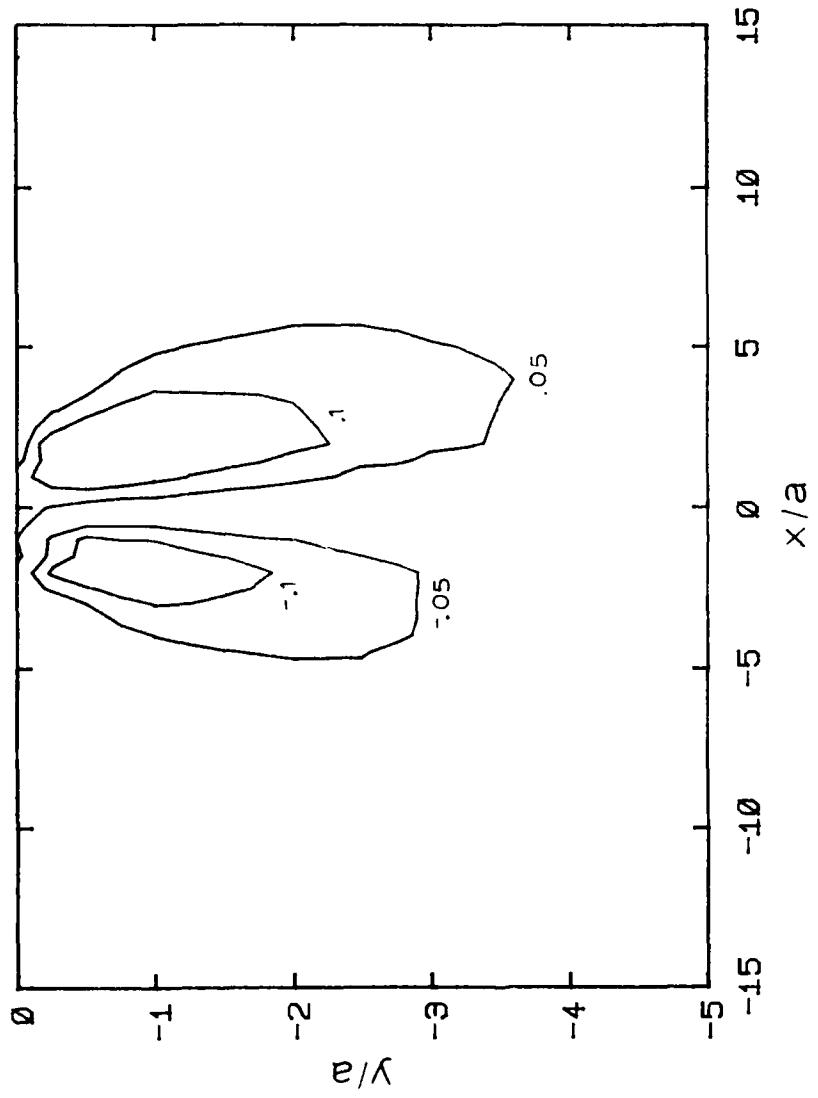


Figure 5.2.16 The steady state τ_{xy} component of the state of stress at different depths normalized with respect to the maximum applied normal stress, p_o , for $p=3/4p_o$, $a=20\mu\text{m}$, $\mu=1$, $E_1/E_2=2.5$, and $d=0.2\mu\text{m}$.

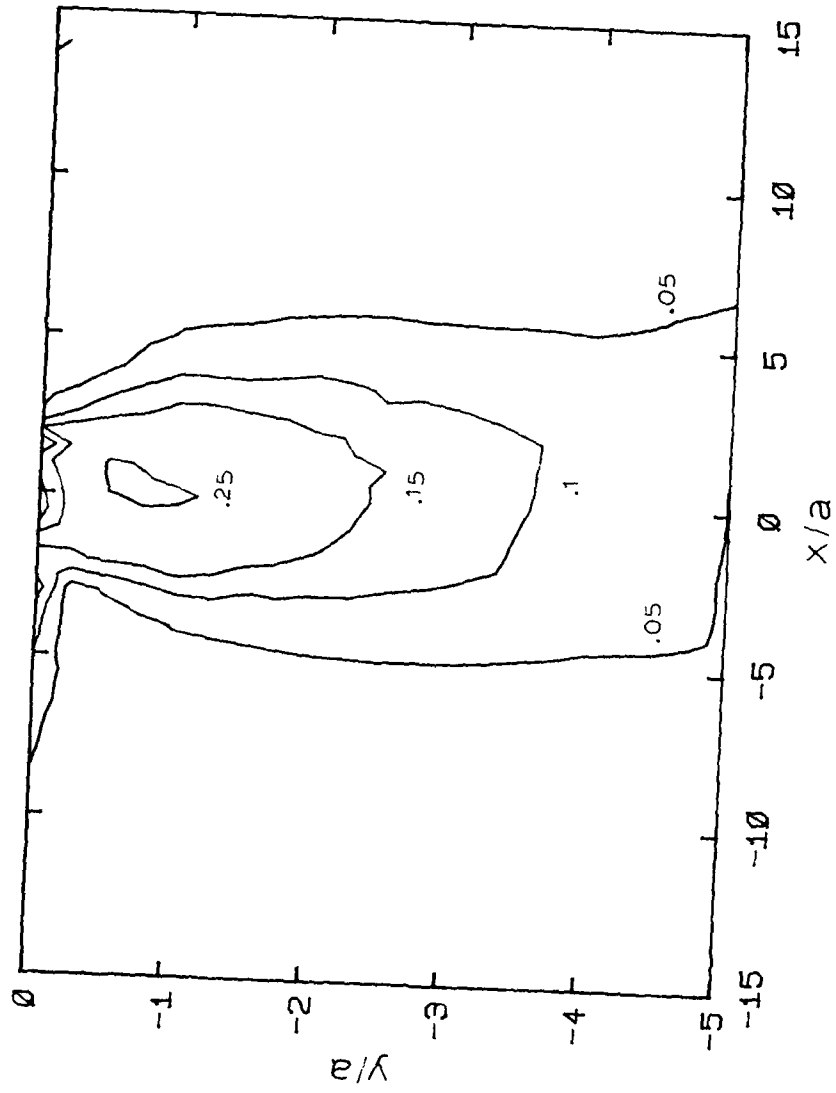


Figure 5.2.17 The steady state τ_{\max} component of the state of stress at different depths normalized with respect to the maximum applied normal stress, p_0 , for $p = 3/4 p_0$, $a = 20 \mu\text{m}$, $\alpha = 1$, $E_1/E_2 = 2.5$, and $d = 2 \mu\text{m}$.

friction coefficient is .1 and the depth of the hardened layer is .2 μm in both cases. Similar to case 2, the stresses are considerably reduced as p is reduced. In both cases the condition for yielding is not met, hence delamination wear will not occur. A similar series of results are shown in Figures 5.2.18 and 5.2.19, now only with $E_1/E_2=1$, ie. no hardened layer. Comparing these results with the previous results, it becomes apparent that the hardened layer has more of an effect on reducing the stresses as the normal pressure is reduced.

A summary of the above cases is as follows:

- A thin hardened layer alone has little effect on reducing subsurface deformation.
- Lowering the friction coefficient substantially reduces subsurface deformation
- If the contact pressure is reduced subsurface deformation may be eliminated.

It is also interesting to note that the shear stress is always positive in front of the contact area and negative behind the contact area. This result agrees with the work conducted by Jahanmir [5] for an elastic perfectly plastic solid.

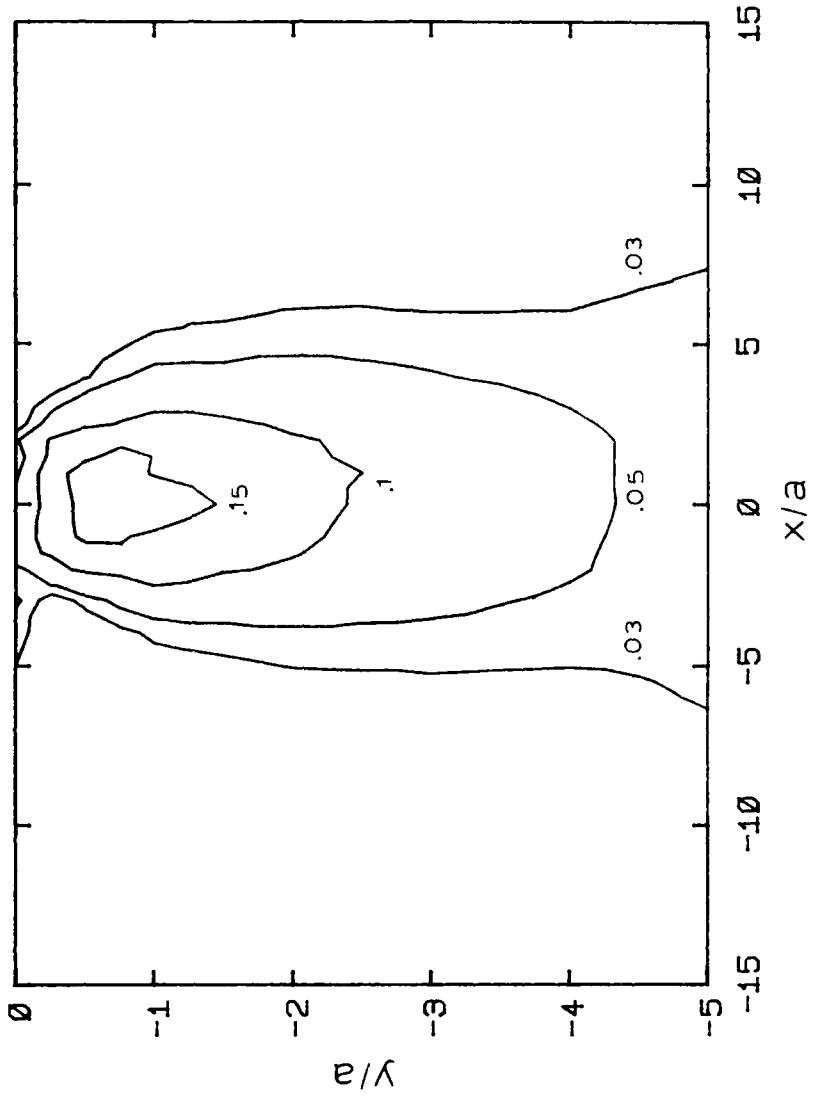


Figure 5.2.18 The steady state τ_{\max} component of the state of stress at different depths normalized with respect to the maximum applied normal stress, p_0 , for $p=1/2p_0$, $a=20\text{m}$, $\mu=1$, $E_1/E_2=1$.

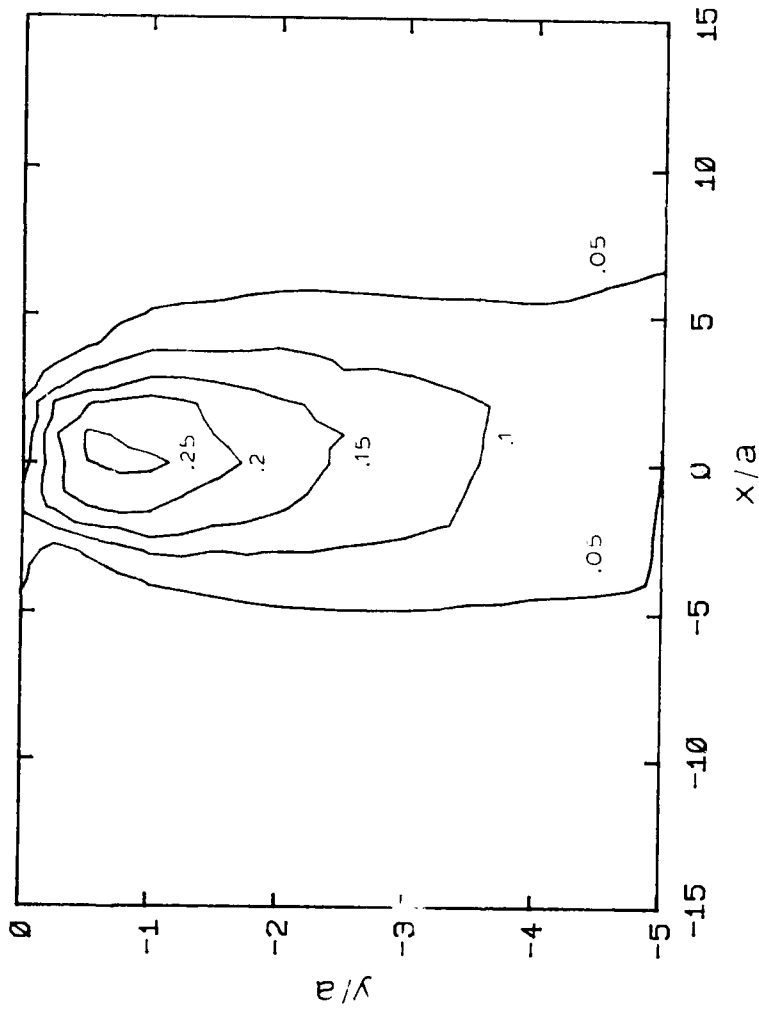


Figure 5.2.19 The steady state τ_{\max} component of the state of stress at different depths normalized with respect to the maximum applied normal stress p_o , for $p=3/4p_o$, $a=20\mu\text{m}$, $\mu=1$, $E_1/E_2=2.5$.

In conclusion, ion implantation will lower the wear rate substantially if the friction coefficient is reduced. For the work conducted here, the friction coefficient is primarily composed of the plowing forces since the tests were lubricated and the sliders and specimens were polished smooth. Because plowing is reduced by an increase in hardness of the surface material, implantation will be effective in reducing wear, if a hardened layer is created.

6. DISCUSSION OF EXPERIMENTAL RESULTS

6.1 Friction Coefficient and Wear

To minimize plowing and consequently friction, the number of embedded wear particles, either from the slider-specimen material or from the environment, must be minimized and/or a smooth hard surface used. In accordance with the model proposed, we found that those implanted specimens which showed a reduction in the friction coefficient (and wear) had a hard, thin layer on the surface. Figure 6.1.1 shows evidence of a hard layer on the N^+ implanted titanium pin surface. Under the applied load, the thin layer appears to have been "crushed in". The N^+ implanted iron pin, shown in Figure 6.1.2, also has this hard layer, signified by the sharp fracture lines along the edge of the plowing scars. A more ductile deformation occurs on the unimplanted surface.

The hard layer found on the N^+ implanted titanium and iron disks could be a result of one or both of the following phenomena:

1. Lattice distortion
2. Formation of hard compounds

In the former case, the increase in the internal stress may impede dislocation motion and hence produce a hardened layer. In the latter case, it is speculated that $Ti_xN_yO_z$



Figure 6.1.1 Typical N^+ implanted titanium pin surface. The surface layer appears to have been "crushed in" at the scar edge. (lubricated test in air; load=400g; 12,000 rev.)



Figure 6.1.2 Typical N^+ implanted iron pin surface after 25 cm of sliding. The brittle fracture lines illustrate the presence of a hard layer. (Load = 400 σ , lubricated test in air)

and $Fe_xN_yO_z$ is formed during the implantation of N^+ into titanium and iron, respectively. Oxygen has been included since it was present on the surface during implantation. Singer [72] found traces of Ti_xN_y in N^+ implanted titanium specimens, although the amount present was not clarified. The presence of $Fe_xN_yO_z$ could then account for the change of color of the implanted surface. The thickness of these layers are estimated (30) to be 2000 \AA ($2 \times 10^{-7} \text{ m}$) and 1375 \AA ($1.575 \times 10^{-7} \text{ m}$), respectively (Figure 6.1.3). The scarring of the N^+ implanted iron specimen varies from an unscarred surface to one with occasional plowing grooves. Only when wear particles or foreign matter are embedded into the pin or disk, are plowing grooves evident. Both implanted pin surfaces were worn, but, not to the extent of the unimplanted pins.

Due to a reduction in the number of plowing grooves on the specimen surfaces and the amount of material plastically deformed on the pin surfaces, it is expected that the friction coefficient will be correspondingly reduced. This is what was observed in both cases, thus supporting the model. Since the friction coefficient was reduced, the wear rate will also be reduced, as was also observed.

The N^+ implanted titanium surfaces showed superior wear resistance. Although this result was attributed to the presence of a hard layer, another mechanism described by

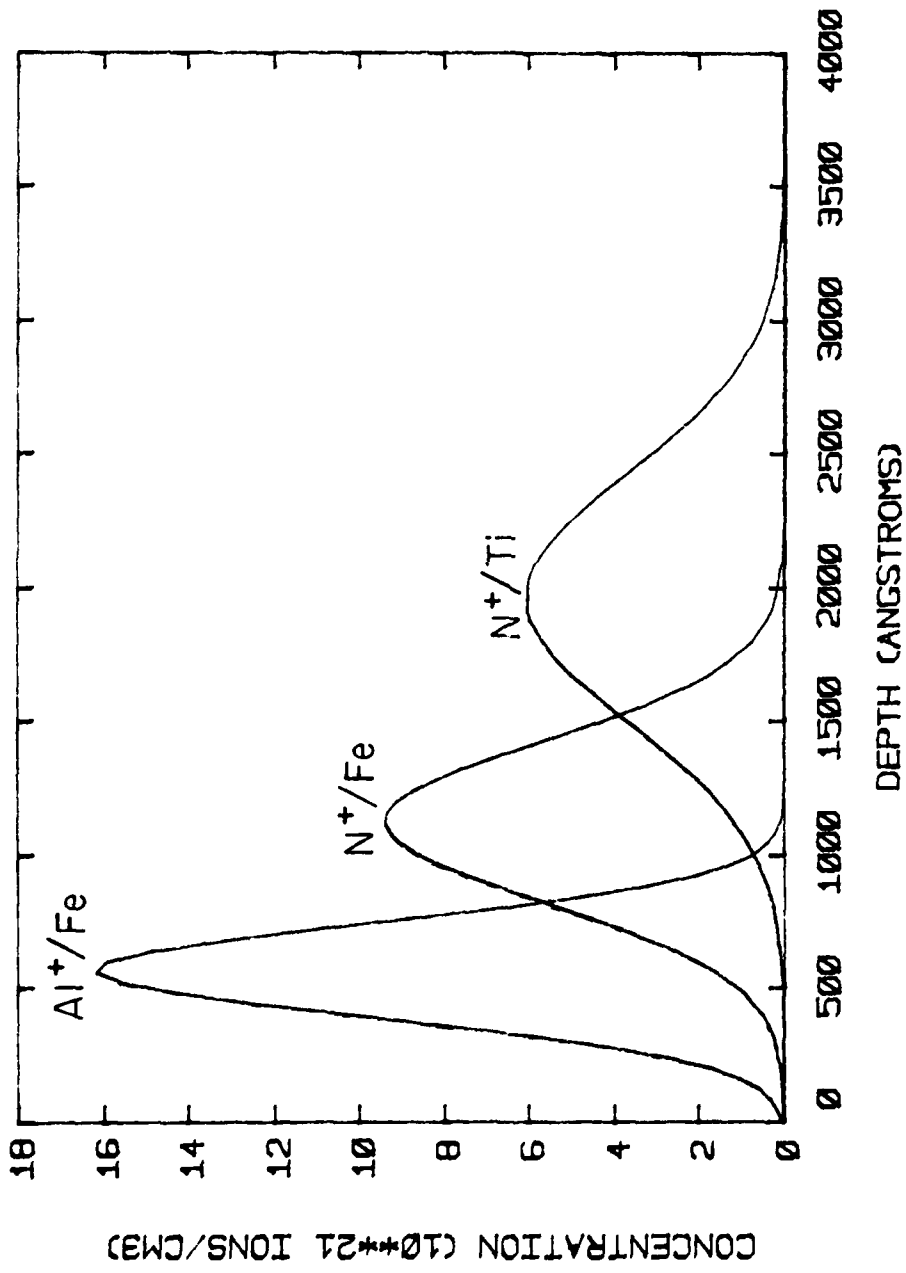


Figure 6.1.3 Predicted depth profiles of some implanted metals. Accelerating voltage = 100 kev; dose = 10^{17} ions/cm².

Buckley and Johnson [73] may also help explain the superior tribological behavior. They found that hexagonal titanium, with a c/a ratio of 1.585, has a high friction coefficient. This was because slipping occurred primarily in the {1010} planes where the critical resolved shear stress (stress required to shear plane) was approximately 5 kg/sq mm in compression. Cobalt on the other hand, has a c/a ratio of 1.625. Here, slipping occurred primarily on the basal plane where the critical resolved shear stress was only .675 kg/sq mm. They also found that when small amounts of alloying elements (oxygen, nitrogen, carbon, etc.) were added to titanium, the lattice ratio was increased and the friction and wear was reduced as slipping occurred primarily on the basal plane. Thus N^+ implanted into titanium might have caused the c/a ratio to increase thus providing better wear resistance.

Unlike the N^+/Ti or N^+/Fe specimens, the Al^+/Fe specimen is deformed and plowed in numerous areas of the wear track. These plowing grooves, however, are much shallower than those on the unimplanted specimen. This explains the reduction in the friction coefficient. As expected, after a sliding distance of several inches the Al^+ implanted iron pin forms embedded wear particles which cause the observed plowing. Although plowing occurs, loose wear particles were sparsely distributed in the lubricant and wear was not measurable even after 56 hours of continuous

sliding. The presence of aluminum on the surface and in the wear groove appears to increase the hardness of the near surface region which explains the increased wear resistance observed. It is speculated that the aluminum present was in the form of Al_2O_3 .

The persistent wear resistance and presence of aluminum at depths greater than that of the implanted layer in the Al^+/Fe specimens can be explained as follows: Plowing of the surface can occur by the plowing tool actually digging into the surface or by the asperity sliding on the top of the surface and pushing the layer down, which causes plastic flow of the material along the edges of the wear groove (Figure 6.1.4). In the latter case, as modeled in Figure 6.1.5, the pin is still sliding on a hardened layer even though plowing occurs. The presence of aluminum at depths much greater than the implanted layer, as shown using SIMS and ISS, cannot be explained in terms of the diffusion process, since predicted diffusion rates of aluminum into iron is only on the order of several atomic diameters for the testing time.

It is interesting to note that the friction coefficient of the Al^+ implanted iron system is half that of the N^+ implanted iron system even though the specimen surface of the Al^+/Fe specimen has a larger number of wear grooves. This can be explained by comparing the worn pin surfaces.



Figure 6.1.4 Typical Al^+ implanted iron specimen wear groove.
(lubricated test in air, load=400 α , 12,000 rev.)

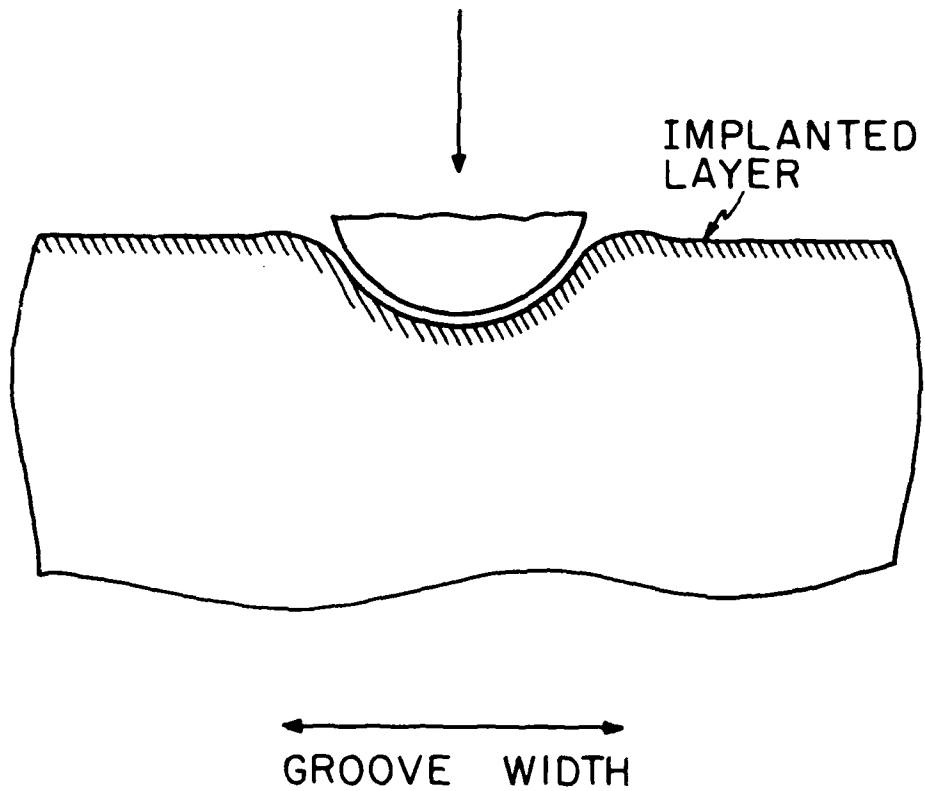


Figure 6.1.5 Model of contact between a rigid asperity and an Al^+ implanted iron surface. Sliding direction is normal to the plane of the paper.

It is speculated that the forces required to deform the N^+ /Fe pin surface are greater than those required in the case of the Al^+ /Fe pin surface, because a thicker hardened layer must be deformed. The thickness of the Al^+ implanted layer is only 750 \AA ($7.5 \times 10^{-8} \text{ m}$). Although the wear was not measurable on the Al^+ /Fe or N^+ /Fe specimen the model predicts that the N^+ /Fe specimen will have a higher delamination wear rate, if it occurs, since the friction coefficient is larger. No such comparison is feasible between the iron and titanium systems since the bulk properties are considerably different.

Plowing was not reduced on the Zn^+ implanted copper pin or specimen and hence, the friction coefficient was the same as that for the unimplanted copper. Zinc atoms usually substitute for copper atoms. Thus, the material hardness does not increase substantially since substitutional solid solution hardening has a relatively mild effect on hardness compared with other hardening methods (i.e. interstitial solid solution hardening). The absence of a hard layer to reduce plowing explains the observed severe subsurface plastic deformation and the unchanged tribological properties.

Although N^+ implanted into copper had no long term effects on the friction and wear behavior, there appeared to be a change in the chemical state of the near surface region

as observed by the formation of a blue film found only on the implanted surface. The implanted layer was either too thin or not hard enough to minimize plowing. If the former case is valid, then perhaps at lighter loads or under better lubrication there may be some application for the N^+ /Cu system. The layer thickness can also be increased by using a range of accelerating voltages and high doses as shown in Chapter 3. In general, most FCC metals do not show a substantial increase in hardness when alloying elements are added to the bulk material.

7. A COMPARISON BETWEEN ION NITRIDING AND ION IMPLANTATION

7.1 Introductory Remarks

It is important to compare the effects of ion implantation with other techniques used to alter the tribological behavior of surfaces in order to investigate the practical applications for implantation. One such process is ion nitriding. It is an inexpensive casehardening technique which uses the energy of a glow-discharge. The specimen becomes the negative electrode of a low pressure glow-discharge in a mixture of nitrogen and hydrogen gases. The nitrogen ions then bombard the specimen surface under the action of an applied voltage [74].

7.2 Advantages and Disadvantages of Ion Nitriding

Ion nitriding has been shown to increase wear resistance, fatigue life, corrosion resistance, and load-carrying ability. One of its major advantage over ion implantation is the cost of casehardening a part. Also the thickness of the hardened layer, approximately .076 cm, is much greater than that formed during ion implantation. As examined in Chapter 6, ion-implanted surfaces do not have any load carrying abilities, because the thickness of the

layer is so thin. Ion nitriding, however, is a time consuming process, taking 25-30 hours on the average, whereas ion implantation (at a dose of 10^{17} ions/cm²) takes between 15 minutes and several hours, depending on the beam current and substrate material. Also the surface finish from the implantation process is superior to the ion nitriding process. In many applications the ion nitrided surface must be finished after nitriding.

7.3 Experimental Procedure

The ion nitrided samples for the friction and wear tests were prepared in the same manner as the ion-implanted samples (see Chapter 4). The samples also were stored in isopropyl alcohol preceding and following nitriding. The nitriding process was conducted in a suitable atmosphere for 30 hours at 783 K. Both pins and disks were nitrided. The testing procedure and conditions were the same as for the implanted samples.

7.4 Experimental Results and Discussion

The friction coefficient of the ion nitrided samples is approximately .1 compared with .128 for the unimplanted iron sample. The friction coefficient of the N⁺ implanted iron sample, however, is approximately .065, still considerably smaller than the ion nitrided sample (Figure 7.4.1)

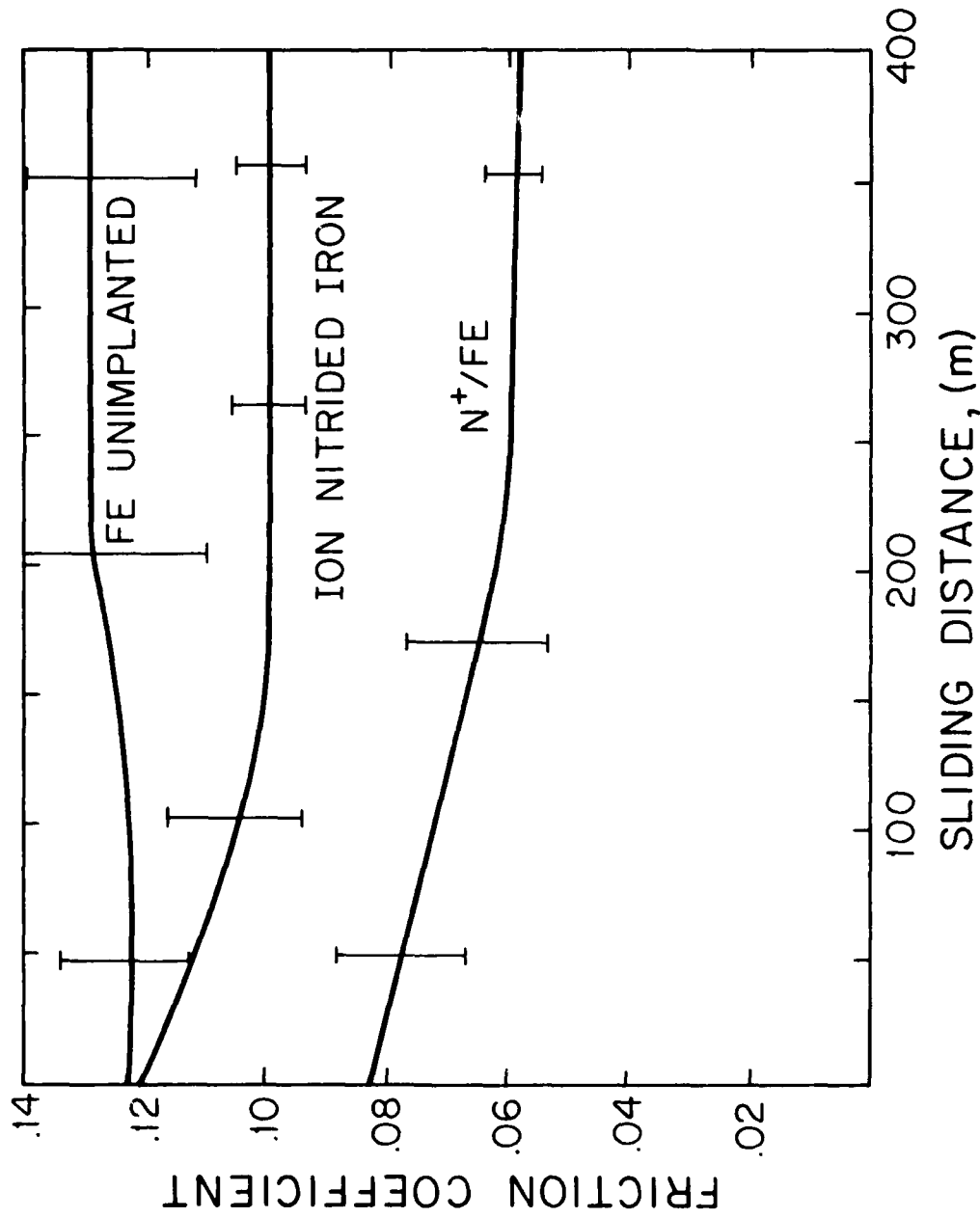


Figure 7.4.1 Change in friction coefficient with sliding distance of unimplanted Fe, ion nitrided Fe, and N^+ implanted iron systems. (lubricated tests in air; load=400g)

The nitrided specimen has a few shallow plowing grooves as seen in Figure 7.4.2. The pin surface, on the other hand, is severely scarred (Figure 7.4.3). The surface is also much rougher than the N^+ implanted pins. Note that the scarred area of the nitrided pin is smooth in the center and there is no evidence of delamination wear particles. Using a Vicker's hardness tester (25 g), the hardness of the nitrided surface was found to be over 3 times greater than the hardness of the untreated iron.

Although the friction coefficient of the ion nitrided surface was higher than the N^+ implanted surface, there is no evidence that the wear rate is higher in the ion nitrided sample. The model proposed in Chapter 5 may not be valid since the thickness of the ion nitrided surface is not known. The nitrided surface may have load carrying ability unlike the implanted surface. The nitrided pin surface is scarred, yet delamination is not evident, whereas on the N^+ implanted pin surface, delamination has occurred. Since subsurface deformation must occur, at depths corresponding to the width of contact (10 μm to 20 μm), for delamination particles to be formed, the depth of the nitrided hardened layer must be large enough to carry some if not all of the load. Hence subsurface deformation will be reduced.

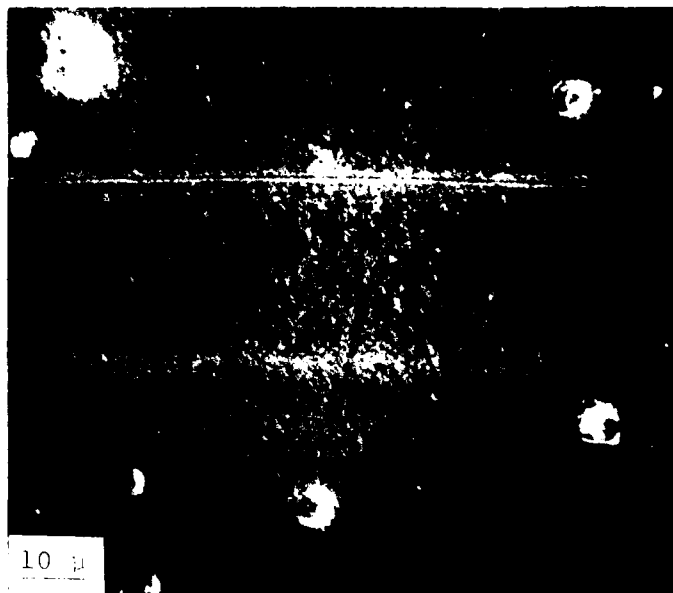


Figure 7.4.2 Typical wear track of an ion nitrided iron disk. (lubricated test in air, load=400g, 12,000 rev.)

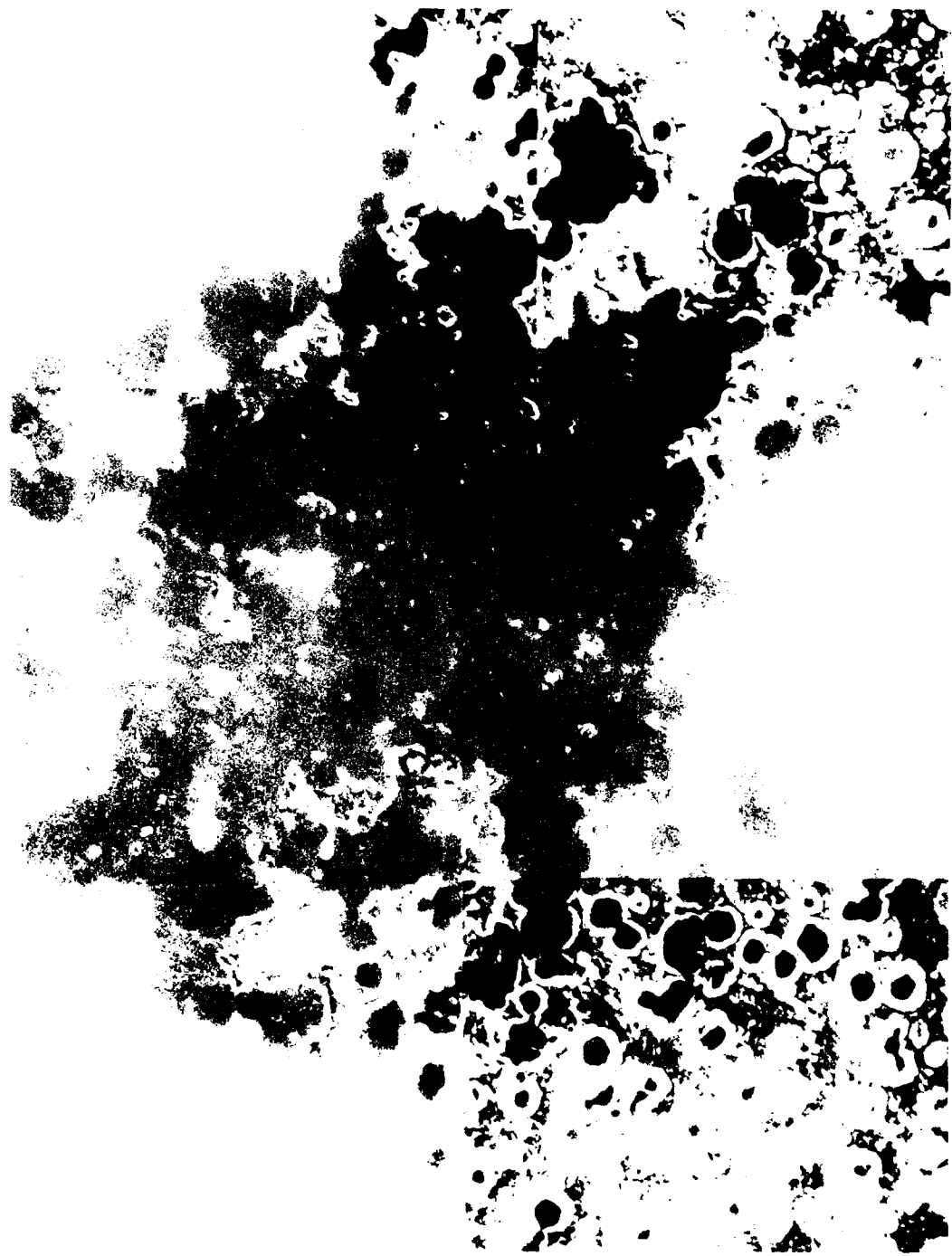


Figure 7.4.3 Typical wear scar on an ion nitrided pin.
(lubricated test in air, load=400g, 12,000 rev.)

The friction coefficient of the ion nitrided surface may be larger than the N^+ implanted surface as a result of the surface roughness. The asperity deformation component of the friction force will be larger in the case of a rougher surface.

There is one important point to note when comparing implantation with ion nitriding using pure iron as the bulk material. In conventional ion nitriding, the major hardening mechanism is attributed to the formation of nitrides with the impurities of the iron [75]. Using pure iron eliminates this hardening mechanism. This may also be the case with N^+ implanted iron except that the depth of the implanted layer is much smaller. Thus with less pure iron, the effects of ion nitriding and ion implantation on the tribological behavior may be superior to the results obtained with pure iron although the second phases may also become the source for crack nucleation.

7.5 Concluding Remarks

Ion nitriding inhibits the delamination wear process in pure iron since the thicker surface layer is able to resist the stresses resulting from surface tractions which reduces subsurface deformation. The wear observed for the testing conditions is approximately the same as that found for N^+ implanted pins and disks. There is evidence that the

thickness of the hardened layer is several orders of magnitude greater for the ion nitrided iron than the implanted iron. Thus the ion nitriding process may be superior to the N^+ implanted process for higher loads and under dry sliding. For lower loads, tribological properties of the N^+ implanted surface appears comparable to ion nitriding although it is unlikely that the mechanisms producing the favorable friction and wear properties are the same in both cases. Ion implantation is superior if the surface finish is of importance. Thus it does not appear that implantation will eliminate all applications for ion nitriding or vice versa. They both are useful surface treatments depending on the application.

8.CONCLUSIONS AND RECOMMENDATIONS

8.1 Major Conclusions

Experimental and theoretical investigations summarized in this report, explain the effect of ion implantation on friction and wear of metals. Improved tribological properties of implanted-metals are a result of the formation of a hardened layer in the near surface region. It is speculated that the hardening is created by changes in mechanical properties and surface chemistry caused by alloying effects. The thin hard layer does not serve to support the load, but rather to decrease the plowing component of friction.

The plowing component of the friction force is reduced when plastic deformation of the pin surface is reduced. When subsurface deformation of this surface is sufficiently lowered, the plowing tools created during the delamination wear process are not formed on the smooth pin surface and hence, the specimen surface is not plowed. This reduction in the plowing component occurs when a hardened layer is created on the surface of the pin. Also plowing can be reduced if this hard layer is present on the specimen surface.

Using FEM to model an isotropic linear elastic semi-infinite solid under contact of a stationary rigid asperity, it was found that changes in the friction coefficient substantially reduces subsurface deformation and hence wear. To summarize, when a hardened layer is created on the surface of a specimen and/or slider, the plowing component is reduced which lowers the friction coefficient. A reduction in the friction coefficient, in turn, reduces wear.

Of the ion-substrate combinations investigated, only the N^+ implanted titanium and iron systems, and the Al^+ implanted iron system showed an improvement in the friction and wear properties. Under the testing conditions, the Zn^+ implanted copper and the N^+ implanted copper had little affect on the tribological properties.

The effects of N^+ implanted into iron on the friction and wear behavior of metals was compared with those of ion nitriding. Ion nitriding appears to have load-carrying abilities, unlike implantation, because the thickness of the nitrided hardened layer is several orders of magnitude larger than that of the ion implanted layer. Consequently, under dry sliding conditions and for higher loads, ion nitriding would be superior to ion implantation. For lower loads under lubricated conditions the N^+ implanted iron surface appears comparable to ion nitriding, although the

mechanisms creating the superior tribological properties are most likely different. On the other hand, ion implantation would be preferred over ion nitriding under light loads, if the surface finish was of importance. The surface is roughened during the ion nitriding process. Clearly, if advances are made in the design of accelerators, ion implantation would be an economical and beneficial surface treatment for numerous applications.

8.2 Recommendations For Future Work

Because of the possible economic and technological impact ion implantation can have on commercial processing, it deserves a thorough investigation of its effects on friction and wear.

Further research needs to be conducted on the effect of varying dosage and thickness of the implanted layer. As with soft coatings, there may be optimum thickness for the hardened layer depending on the ions and bulk material. Also, as several investigators have observed, there is an optimum dose whereby the benefits of ion implantation on the tribological properties is maximized.

The postulated mechanisms of friction and wear of implanted-metals, presented in this report, provides only a fundamental foundation for implantation theory. Further theoretical analysis needs to be conducted in order to expedite or eliminate trial and error experimental research.

REFERENCES

1. Buckley, D.H., "Definition and Effect of Chemical Properties of Surface in Friction, Wear and Lubrication," Fundamentals of Tribology, Ed. Suh, N.P., Saka, N., MIT Press, MA, 1978, pp. 173-199.
2. Rabinowicz, E., Friction and Wear of Materials, Wiley, 1965.
3. Archard, J.F., and Hirst, W., "An Examination of the Mild Wear Process," Proc. Royal Soc. A, 238, 1956, pp. 515-527.
4. Rabinowicz, E., "Influence of Surface Energy on Friction and Wear Phenomenon," J. Appl. Phys., 32, 1961, pp. 1440-1444.
5. Jahanmir, S., "A Fundamental Study on the Delamination Theory of Wear," Ph.D Thesis, Department of Mech. Engr., MIT, 1976.
6. Suh, N.P., et al., The Delamination Theory of Wear, Elesevier, 1977.
7. Bowden, F.P., and Tabor, D., Friction and Lubrication of Solids, Oxford Univ., Part I 1950, Part II 1964.
8. Archard, J.F., "Contact and Rubbing of Flat Surfaces," J. Appl. Phys., 24, 1953, pp. 981-998.
9. Burwell, J.T., and Strang, C.D., "On the Empirical Law of Adhesive Wear," J. Appl. Phys., 23, 1952, pp. 18-32.
10. Suh, N.P., Sin, H.-C., "On the Genesis of Friction and Its Effect on Wear," Wear, 1981, to appear.
11. Lindhard, J., Scharff, J.M., and Schiott, H.E., K. Dan. Vidensk. Selsk. Mat. Fys. Medd., 33, No. 14, 1963.
12. Townsend, P.D., Kelly, J.C., and Hartley, N.E.W., Ion Implantation, Sputtering and their Application, Academic Press, NY, 1976.
13. Mayer, J.W., Ion Implantation in Semiconductors, Academic Press, NY, 1970.
14. Dearnaley, G., Freeman, J.H., Nelson, R.S., and Stephen, J., Ion Implantation, North Holland Publ.

Co., 1973.

15. Littmark, U., and Ziegler, J.F., Range Distributions For Energetic Ions in All Elements, 6, Ed. Ziegler, J.F., Pergamon Press, NY, 1980.
16. Dearnaley, G., Annual Review of Material Science, 4, Annual Review Inc., 1974.
17. Sartwell, B.D., "Surface Alloying by Ion Implantation: An Alternative to Cadmium Electroplating," Proc. of the Govn't Industry Workshop on Alternatives to Cadmium Electroplating, NBS, Gaithersburg, Md, Oct. 1977.
18. Morehead, F.F. Jr., and Crowder, B.L., "Ion Implantation," Sci. American, 228, no. 4, 1973, pp. 65-71.
19. Hirvonen, J.K., "Introduction," Treatise on Matl. Sci. and Technol., Academic Press, NY, 1980, pp. 1-15.
20. Ashworth, V., Grant, W.A., and Procter, R.P.M., "The Application of Ion Beams to Corrosion Science," Corrosion Science, 16, 1976, pp. 661-675.
21. Dearnaley, G., "Ion Beam Analysis Techniques in Corrosion Science," International Conf. on Ion Beam Surface Analysis, Karlsruhe, Plenum, 1975, pp. 885-899.
22. Dearnaley, G., et al., "Ion-Beam Analysis of Corrosion Films on 316 Steel," J. of Vac. Sci. and Technol., 12, No. 1, 1975, pp. 449-453.
23. Towler, C., Collins, R.A., and Dearnaley, G., "Impurity Effects on Corrosion of Aluminum," J. of Vac. Sci. and Technol., 12, No. 1, 1975, pp. 520-523.
24. Dearnaley, G., "The use of Ion Beams in Corrosion Science," Proc. of the Conf. on Appl. Ion Beams to Metals, Alburquerque, N.M., Plenum, 1973, pp. 63-85.
25. Ashworth, V., et al., "The Influence of Ion Bombardment on the Corrosion of Metals," Proc. of the International Conf. on Ion Implantation in Semiconductors and Other Materials, Yorktown Hgts., NY, Plenum, 1973, pp. 443-453.
26. Ashworth, V., Baxter, D., Grant, W.A., and Procter, R.P.M., "The Effect of Ion Implantation on the Corrosion Behavior of Pure Iron-III. Tantalum Ion Implantation," Corrosion Sci., 17, 1977, pp. 947-960.

27. Ashworth, V., Baxter, D., Grant, W.A., and Procter, R.P.M., "The Effect of Ion Implantation on the Corrosion Behavior of Pure Iron-II. Chromium Ion Implantation," Corrosion Sci., 16, 1976, pp. 775-786.
28. Ashworth V. Grant, W.A., Procter, R.P.M., and Wellington, T.C., "The Effect of Ion Implantation on the Corrosion Behavior of Pure Iron-I. Argon Ion Implantation," Corrosion Sci., 16, 1976, pp. 393-401.
29. Ashworth, V., et al., "The Effect of Ion Implantation on the Corrosion Behavior of Fe," Proc. of the International Conf. on Ion Implantation in Semiconductors and Other Materials, Osaka, Japan, Plenum, 1974, pp. 367-373.
30. Ashworth, V., Procter, R.P.M., Grant, W.A., "The Application of Ion Implantation to Aqueous Corrosion," Treatise on Materials Science and Technology, 18, Ed. Hirvonen, J.K., Academic Press, NY, 1980, pp. 176-256.
31. Dearnaley, G., "Ion Implantation for Improved Resistance to Wear and Corrosion," Materials in Engr. Application, 1, 1978, pp. 28-41.
32. Hayashi, H., Iwaki, M., and Yoshida, K., "Ion Implantation into Metals," Proc. of the 4th International Conf. on Prod. Engr., Tokyo, 1980, pp. 1051-1056.
33. Baumvol, I.J.R., Watkins, R.E.J., and Longworth, G., "Wear and Oxidation Studies in Iron Implanted with Tin," Inst. of Phys., 1980.
34. Kubaschewski, O. and Hopkins, B.E., Oxidation of Metals and Alloys, Butterworth and Co. Ltd., 1962, pp. 70-120.
35. Dearnaley, G., Goode, P.D., Miller, W.S., and Turner, J.F., "The Influence of Ion Implantation Upon High Temperature Oxidation of Titanium and Stainless Steel," Proc. of the International Conf. on Ion Implantation in Semiconductors and Other Materials, Yorktown Hgts, NY, Plenum, 1972, pp. 405-414.
36. Antill, J.E., et al., "The Effect of Surface Implantation of Yttrium and Cerium Upon the Oxidation Behavior of Stainless Steels and Aluminized Coatings at High Temperatures," Corrosion Sci., 16, 1976, pp. 729-745.
37. Antill, J.E. et al., "The Effects of Yttrium Ion

Implatation Upon the Oxidation Behavior of an Austenitic Stainless Steel," Proc. of the International Conf. on Ion Implantation in Semiconductors and Other Materials, Yorktown Hgts, NY, Plenum, 1972, pp. 415-422.

38. Dearnaley, G., "Thermal Oxidation," Treatise on Material Sci. and Technol., 18, Ed. Hirvonen, J.K., Academic Press, NY, 1980, pp. 257-319.
39. Hartley, N.E.W., "Tribological and Mechanical Properties," Treatise on Materials Sci. and Technol., 18, Ed. Hirvonen, J.K., Academic Press, NY, 1980, pp. 360-363.
40. Hirvonen, J.K., "Ion Implantation and Corrosion Science," J. Vac. Sci. Technol., 15, No. 5, Sept/Oct. 1978, pp. 1662-1668.
41. Hu., W.W., et al., "Surface-Related Mechanical Properties of Nitrogen-Implanted 1018 Steel," Scripta Met., 12, 1978, pp. 697-698.
42. Hirvonen, J.K., et al., "Improvement of Metals Properties by Ion Implantation," Thin Solid Films, 63, 1979, pp. 5-10.
43. Dearnaley. G., and Hartley, N.E.W., "Ion Implantation into Metals and Carbides," Thin Solid Films, 54, 1978, pp. 215-232.
44. Clayton, P., "The Relations Between Wear Behavior and Basic Material Properties for Pearlitic Steels," Wear, 60, 1980, pp. 75-93.
45. Lo Russo, S. et al., "Fatigue-Life Improvements by Nitrogen Ion Implantation on Steel: Dose Dependence," American Inst. of Phys., 1980, pp. 822-823.
46. Herman, H., "Surface Mechanical Properties- Effects of Ion Implantation," Albany, NY, 1980, to be published.
47. Kujor, A., Chakrabortty, S.B., Starke, E.A. Jr., and Leff, K.O., "The Effect of Aluminum Ion Implantation on the Fatigue Crack Initiation of Polycrystalline Copper," Proc. Mat. Res. Soc. Ann. Meeting, Cambridge MA, 1979.
48. National Mat. Advisory Board Committee on Ion Implantation and Competing New Surface Treatment Technologies, Ion Implantation as a New Surface Treatment Technology, Report NMAB-349, National Academy

of Sci., Wash. D.C., 1979.

49. Hartley, N.E.W., et al., "Friction Changes in Ion-Implanted Steel," J. of Mat. Sci., 8, 1973, pp. 900-904.
50. Hartley, N.E.W., et al., "Friction and Wear of Ion-Implanted Metals," Applications of Ion Beams of Metals, Ed. Picraux et al., Plenum, NY, 1973, pp. 123-138.
51. Hartley, N.E.W., "Surface Stresses in Ion-Implanted Steel," J. Vac. Sci. Technol., 12, No. 1, Jan./Feb., 1975, pp. 485-489.
52. Hartley N.E.W., "Ion Implantation and Surface Modification in Tribology," Wear, 34, 1975, pp. 427-438.
53. Hartley, N.E.W., "Tribological Effects in Ion-Implanted Metals," Applications of Ion Beams to Materials, Ed, Carter, G., Colligen, J., and Grant, W.A., Inst. of Phys., London, 1976.
54. Pavlov, A.V., et al., Proceedings of All Soviet Meetings on Ion Beam Phys., Kiev, 1974.
55. Suri, A.J., Nimmagadda, R., and Bunshah, R.F., "Application of Ion Implantation and Ion Plating on Stainless Steel, Titanium, and Aluminum," Report No. NADC-7928-60, Naval Air Systems Command, Dept. of the Navy, Wash. D.C., 1978.
56. Singer, I.L., Carosella, C.A., and Reed, J.R., "Friction Behavior of 52100 Steel Modified by Ion Implanted Ti," Proc. of the Ion Beam Modification of Mat. Conf., Albany, NY, 1980.
57. Myers. S.M., "Implantation Metallurgy- Equilibrium Alloys," Treatise on Materials Sci. and Technol., 18, Ed. Hirvonen, J.K., Academic Press, NY, 1980, pp. 51-84.
58. Poate, J.M., and Cullis, A.G., "Implantation Metallurgy- Metastable Alloy Formation," Treatise on Mat. Sci. and Technol., 18, Ed. Hirvonen J.K., Academic Press, NY, 1980, pp. 85-134.
59. Wolf, G.K., "Chemical Properties of Ion Implanted Materials," Treatise on Mat. Sci. and Technol., 18, Ed. Hirvonen, J.K., Academic Press, NY, 1980, pp. 373-414.

60. Mayer, J.W., et al., "High-Dose Implantation and Ion-Beam Mixing," Proc. of the Mat. Research Soc., Nov. 1979.
61. Tasur, B.Y., Lau, S.S., Liau, Z.L., and Mayer, J.W., "Ion-Beam-Induced Intermixing of Surface Layers," Thin Solid Films, 63, 1979, pp. 31-36.
62. Picraux, S.T., Myers, S.M., and Follstaedt, D.M., "Microalloy Layer Formation by Ion Implantation," Thin Solid Films, 63, 1979, pp. 1-2.
63. Hirvonen, J.K., Personal Communications.
64. Kanaya, K., Koga, K., and Toki, K., J. Phys. E: Instrum., 5, 1972, pp. 641-648.
65. Gabovich, M.D., Budernaya, L.D., Poritskii, V.Y., and Protsenko, I.M. Proc. of all Soviet Meetings on Ion Beam Phys., Kiev, 1974.
66. Takagi, T., Yamada, I., and Kimura, H., Proc. Int. Conf. on Ion Implantation in Semiconductors and Other Materials, Ed. Namba, S., Plenum, NY, 1974.
67. Fremlin, J.H., and Askouri, N.A., "Hardening of Tungsten Carbide by Irradiation," Nature, 249, May 1974, pp. 137.
68. Bolster, R.N., and Singer, I.L., "Surface Hardness and Abrasive Wear Resistance of Ion-Implanted Steels," Pres. at the ASME/ASLE Lubr. Conf., San Francisco, CA, Aug. 1980.
69. Rabinowicz, E., "Abrasive Wear Resistance as a Materials Test," Lubr. Engr., 33, 1977, pp. 378-381.
70. Rabinowicz, E., "Taper Sectioning, A method for the Examination of Metal Surfaces," J. Metal Industry, 76, 1950, pp. 813-886.
71. Torrance, A.A., "The Metallography of Worn Surfaces and Some Theories of Wear," Wear, 50, 1978, pp. 169-182.
72. Singer, I.L., Personal communications.
73. Buckley, D.H., Johnson, R.L., "Friction and Wear of Hexagonal Metals and Alloys as Related to Crystal Structure and Lattice Parameters in Vacuum," Pres. at an ASLE paper at Lubr. Conf., San Francisco, Oct. 1965, pp. 121-135.

74. Jones, C.K., Martin, S.W., and Sturges, D.J.,
"Glow-Discharge Nitriding in Production," Metals
Progress, Dec. 1973.
75. Bathe, K.-J., ADINA, A Finite Element Program for
Automatic Dynamic Incremental Nonlinear Analysis,
Report 82448-1, Sept. 1975.

APPENDIX A: SAMPLE MATERIAL AND PREPARATION

A description of sample preparation is given in chapter 4. A more detailed description of sample composition and sectioning is described herein.

A.1 Chemical Composition and Processing Methods

The materials were selected to represent a variety of crystalline structures; fcc, bcc and hcp. Also only single phase materials were used in order to reduce the number of design parameters. For example, the effect of carbon in iron considerably complicates the interpretation of results.

1. High Purity Iron (99.9999%)- A chemical analysis of the iron is given in Table A.1.1. The pin mateial was electron beam melted and cold fabricated to size under clean room conditions. The specimen material has inclusions due to the processing method.
2. Commercially Pure Titanium- The titanium was obtained commercially as hot rolled rods. The constituents (maximum) other than titanium include .05 N, .10 C, .015 H, .025 O, and .20 Fe.
3. O.F.H.C. Copper- The copper bars, 99.95% pure, were

Table A.1.1 Chemical Analysis of High Purity Iron

H	Li	Be	B	C	N	O	F	Na	Mg	Si	P
<1.00			12.0	10.0	60.0			1.60	0.87	<0.10	0.70
Al	S	Cl	K	Ca	Ti	V	Cr	Mn	Fe	Co	Ni
<0.10	2.60	0.80	1.80	0.80	1.40		1.60		MAJOR		<0.10
Cu	Zn	Ga	Ge	As	Zr	Nb	Mo	Rh	Pd	Ag	Cd
0.60	1.90	<0.10			<0.10	<0.10	<0.10			<0.10	<0.10
In	Sn	Sb	Te	Ta	W	Pt	Au	Pb	Bi		
<0.10	<0.10	<0.10		<0.10	<0.10	<0.10	<0.10	<0.10	<0.10		

cold rolled.

A.2 Sample Sectioning and Mounting

Prior to sectioning the samples, the surfaces were protected by a nickel coating. The specimens were vapor degreased, and rinsed in isopropyl alcohol prior to plating to insure strong bonding between the substrate and the nickel. The plating was done at low current to insure a smooth continuous layer.

The worn specimens, that were sectioned, were orientated as shown in Figure A.2.1. There is some distortion of the surface. Any rod shape inclusions lying parallel to the surface and perpendicular to the edge will appear thicker. Those lying parallel to the edge, however, will not be distorted. No direct strain measurements are taken from the SEM micrographs, consequently the problem of interpretation is bypassed.

Preceding polishing and cleaning, the samples were etched. The etchants used are as follows:

Iron- 1% nital

O.F.H.C. Copper- 100 ml H_2O ; 8 ml H_2SO_4 ; .5 ml HCl;
2 g potassium dichromate.

Titanium- 33% HF; 33% Chloric Acid; 33% H_2O ; by
volume.

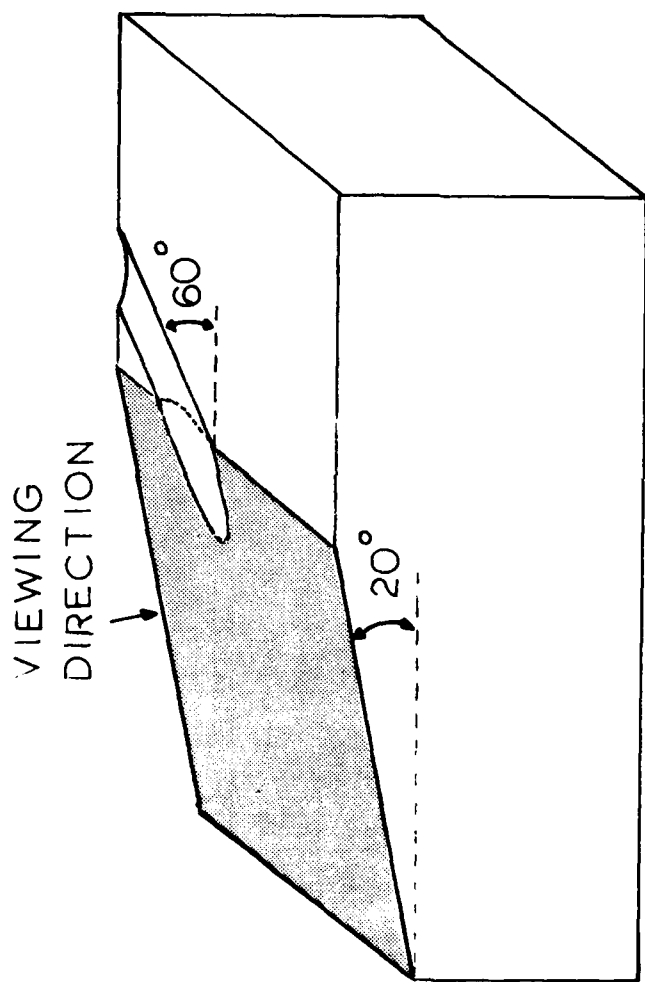


Figure A.2.1 The principle of Taper Sectioning. Viewing plane for examining subsurface deformation on worn track.

APPENDIX B: ESTIMATION OF WEAR VOLUME
USING TALYSURF TRACE

The Talysurf traces were taken at 0° , 90° , 180° , and 270° for each wear track. The area of the wear track is estimated for all four traces of a given track, as shown below. These areas are then averaged so that the wear volume can be estimated.

For this example assume the trace shown in Figure B.1 represents the "average" wear area.

The wear rate is given by:

$$V = \frac{2Ar}{s}$$

Where:

A= area of material worn on trace

r= radius of worn track

s= total sliding time

For this example

$$V = \frac{(1.856 \times 10^{-3} \text{ mm}^2 \times 2 \times 15.5 \text{ mm})}{3600 \text{ sec}} = 5 \times 10^{-5} \text{ mm}^3/\text{sec}$$

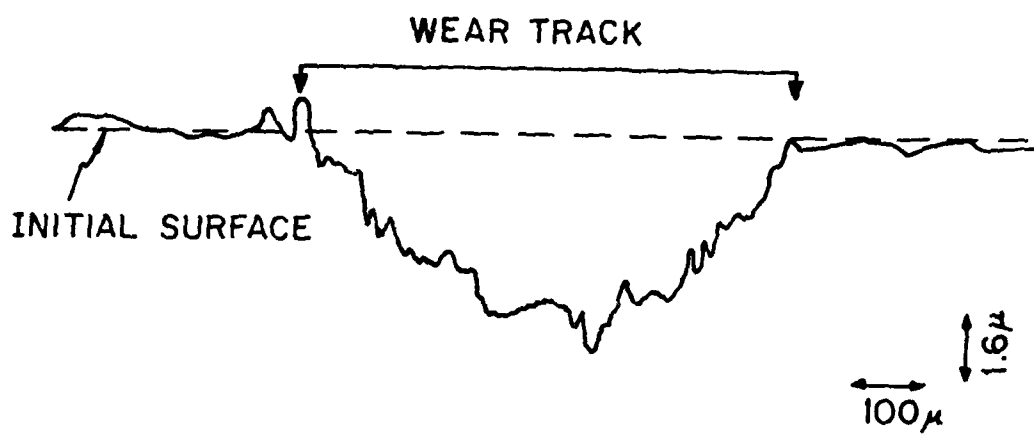


Figure B.1 A typical surface profile of a wear track.

APPENDIX C: FEM SOLUTION

Techniques used in deriving an approximate solution of surface and subsurface stresses for a linear elastic semi-infinite solid against a rigid plane is described below. The effect of a hard thin layer on top of a softer bulk material, as it occurs in some ion-implanted systems is examined. ADINA (Automatic Dynamic Incremental Nonlinear Analysis), a finite element computer program for the static and dynamic displacement and stress analysis of solids, fluid-structure systems, and structures, was used to solve the above problem. Two dimensional plane strain elements were used. Figure C.1 shows the mesh used in solving the problem, where d is the depth of the hardened layer with Young's modulus, E_1 , and Poisson's ratio, ν_1 .

Typical elements used in the mesh are shown in Figure C.2. For all elements, there were 8 input nodes. However, the output stress table includes 9 points (including one in the center of the element). In many cases a single node may be a point in several elements. For example, in Figure C.2, node 3 in element 1, (E_1), is also node 4 in element 2, (E_2), node 1 in element 3, (E_3), and node 2 in element 4, (E_4). The stress values of this point, vary within a few % from element to element because the equilibrium equations are continuously changing.

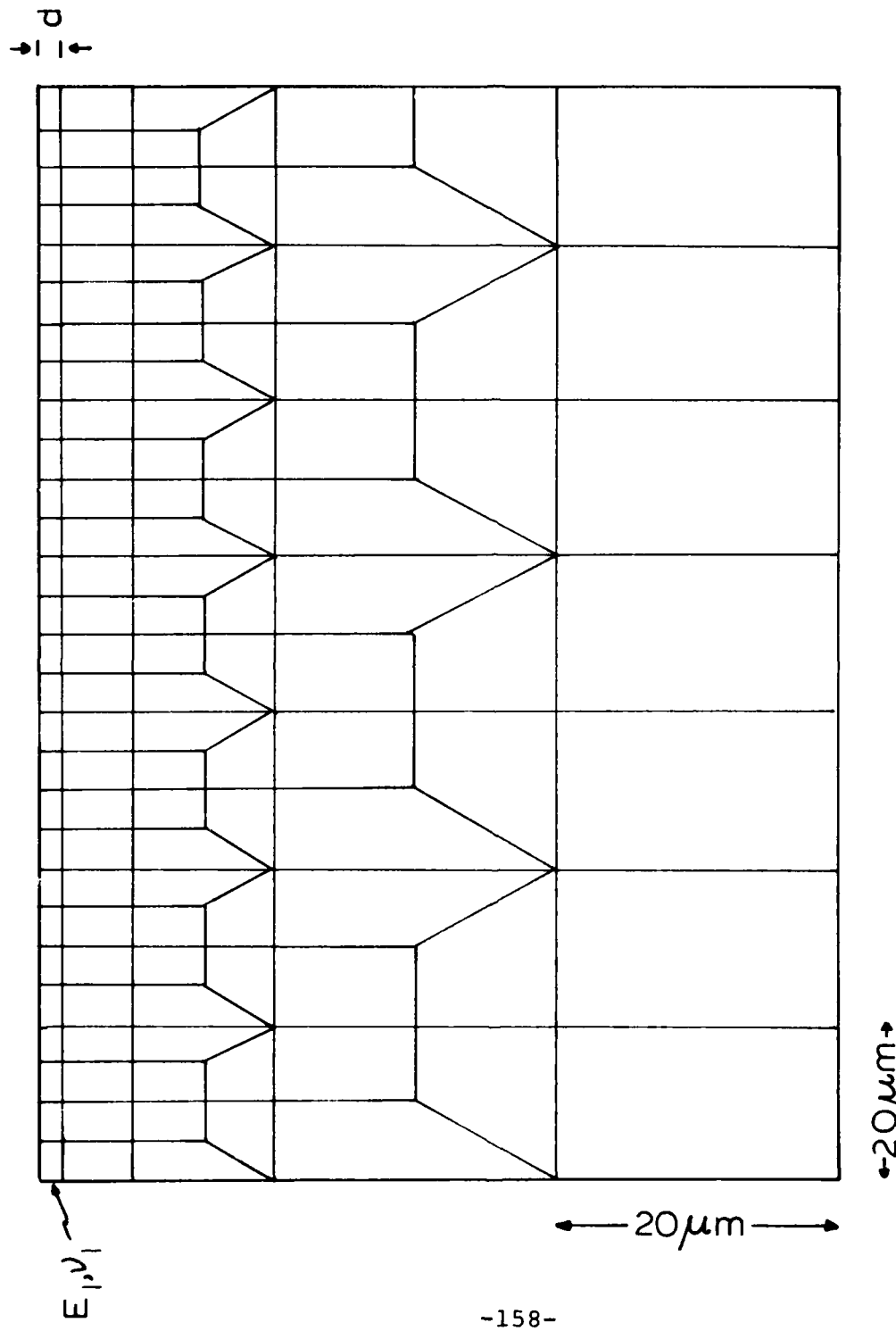


Figure C.1 Finite element grid used to represent a hard thin layer on a soft bulk material (E_1, v_1 for thin layer, E_2, v_2 for bulk material).

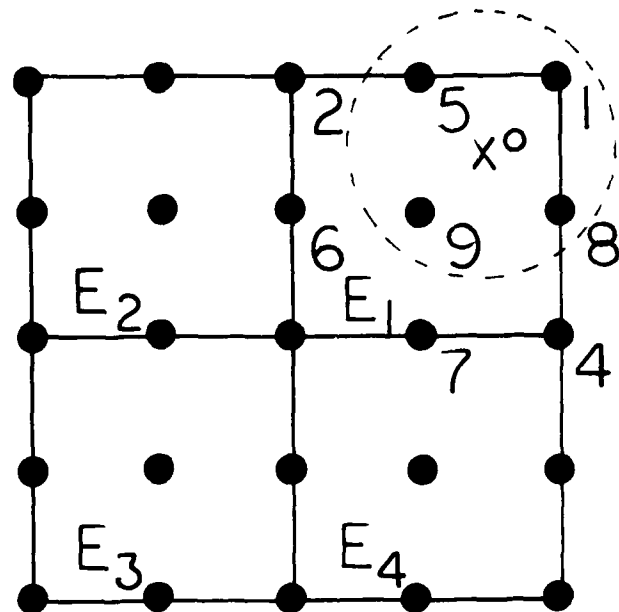


Figure C.2 Typical 2-D elements including nodal point configuration.

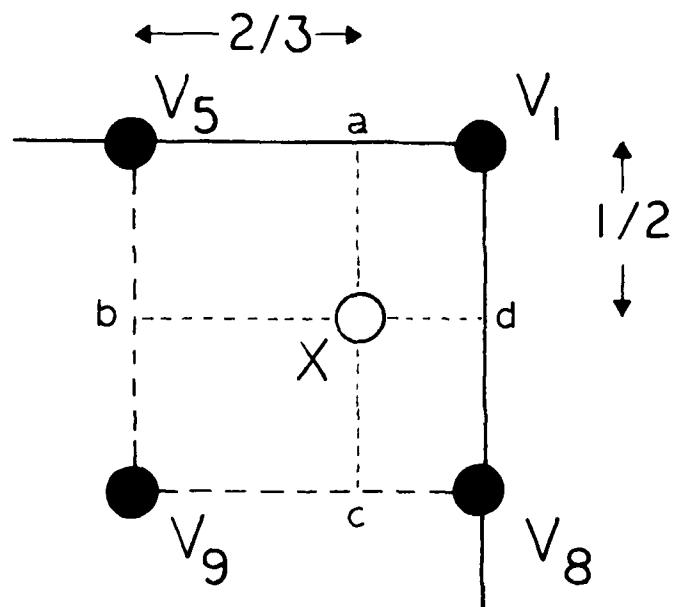


Figure C.3 Schematic for weighted average technique.

In order to plot the stresses, a single value for each node must be determined. The method used to determine these values, for the mesh described above is as follows:

1. The values for a given node are averaged. This is done for each node.
2. To plot the stresses, the values of interior points of the element are needed if the block size is changed. To find the stress values in an interior point of a given element a weighted average technique was employed using both vertical and horizontal nodes. For example, the value of point X in Figure C.3 would be determined as follows:

$$\begin{aligned} 2/3 v_1 + 1/3 v_5 & \text{ -value at point a } (v_a) \\ 1/2 v_1 + 1/2 v_8 & \text{ -value at point d } (v_d) \\ 1/2 v_5 + 1/2 v_9 & \text{ -value at point b } (v_b) \\ 2/3 v_9 + 1/3 v_8 & \text{ -value at point c } (v_c) \end{aligned}$$

Then the value at X is:

$$x = \left(\frac{2v_b + v_d}{3} + \frac{v_a + v_c}{2} \right) / 2$$

For more information concerning ADINA refer to reference 75.

APPENDIX D: SUBSURFACE STRESS DISTRIBUTIONS

The steady state σ_{xx} , σ_{yy} , τ_{xy} components of the state of stress at different depths normalized with respect to the maximum applied normal stress, p_0 , for contact length, $a=20 \mu\text{m}$, and for different E_1/E_2 ratios, friction coefficients and hard layer depths, are presented in this appendix.

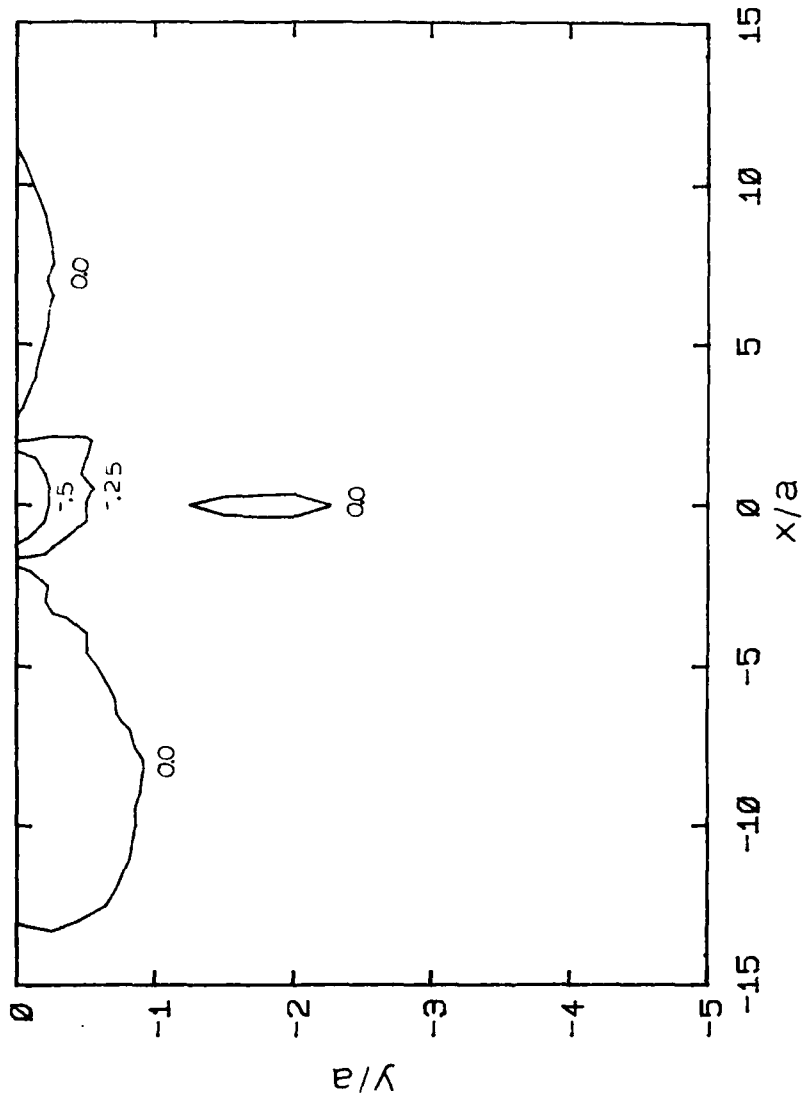


Figure D.1 The steady state σ_{xx} component of the state of stress at different depths normalized with respect to the maximum applied normal stress, p_o , for contact length, $a=20\mu\text{m}$, $\mu=.1$, $E_1/E_2=1$, and $d=2\mu\text{m}$.

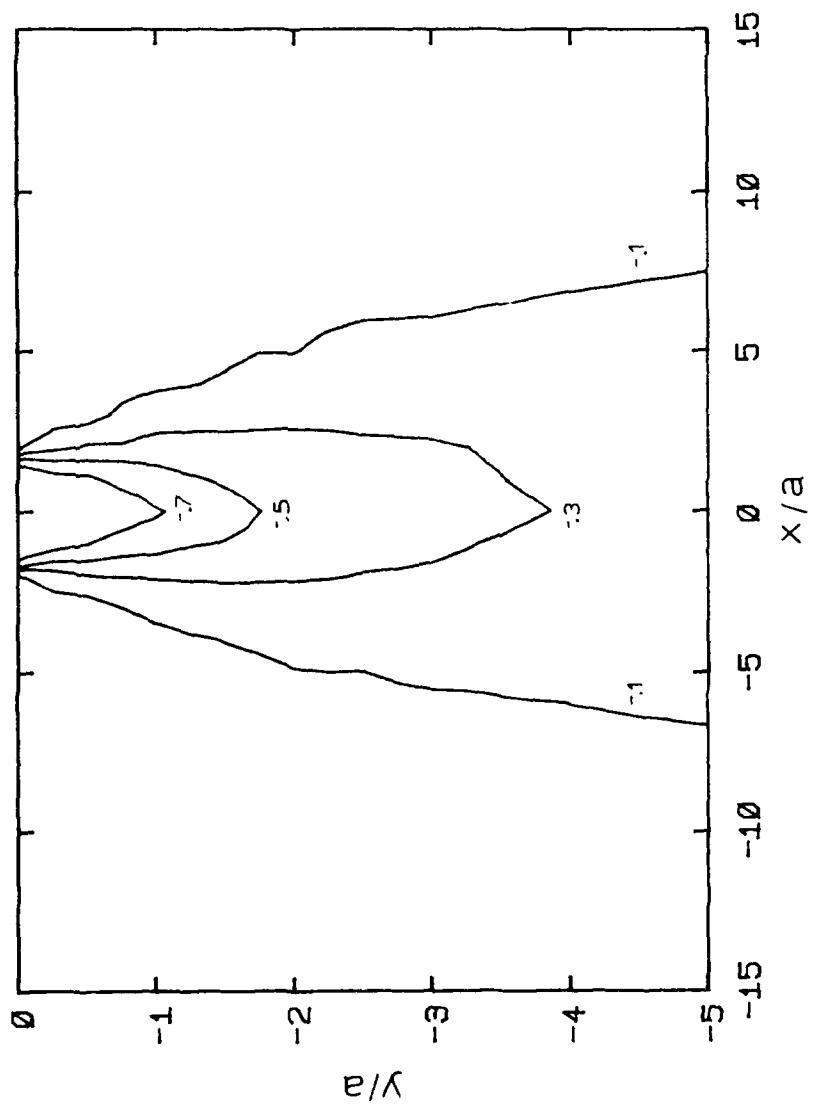


Figure D.2 The steady state σ_{yy} component of the state of stress at different depths normalized with respect to the maximum applied normal stress, p_0 , for contact length, $a=20\mu\text{m}$, $\mu=0.1$, $E_1/E_2=1$, and $d=2\mu\text{m}$.

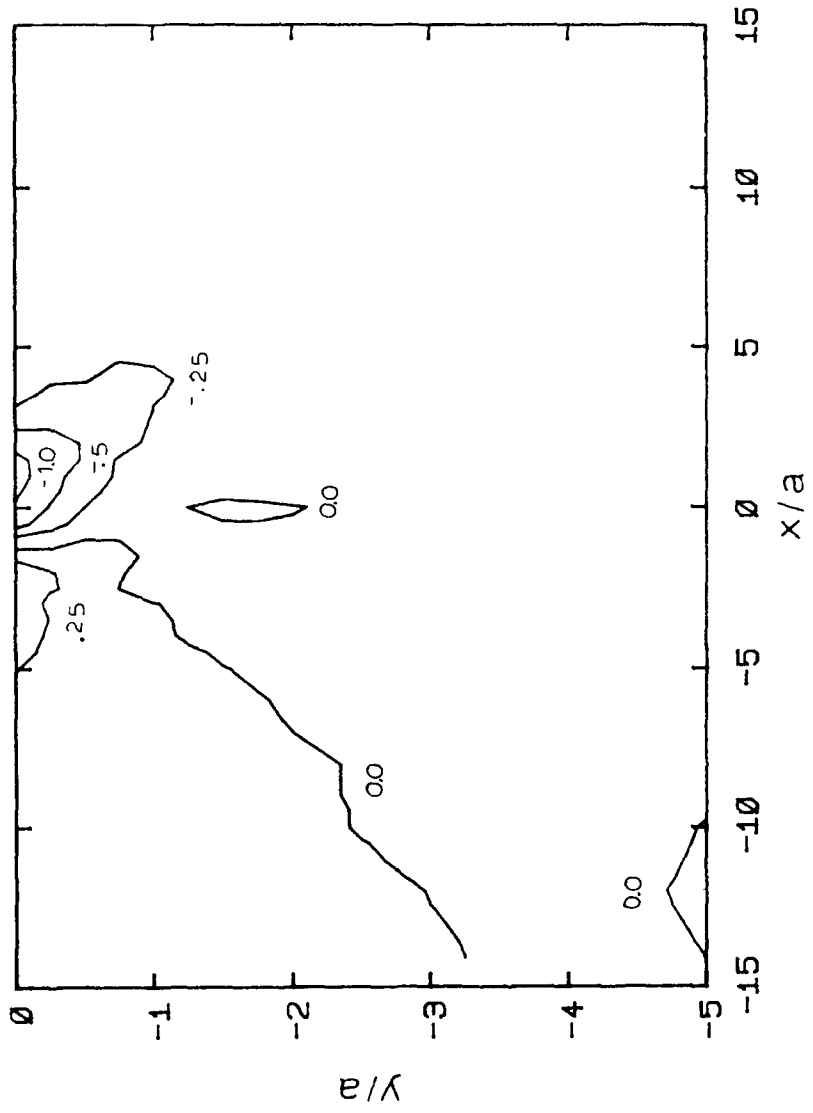


Figure D.3 The steady state σ_{xx} component of the state of stress at different depths normalized with respect to the maximum applied normal stress, p_0 , for contact length, $a=20\mu\text{m}$, $\nu=.47$, $E_1/E_2=2.5$, and $d=.2\mu\text{m}$.

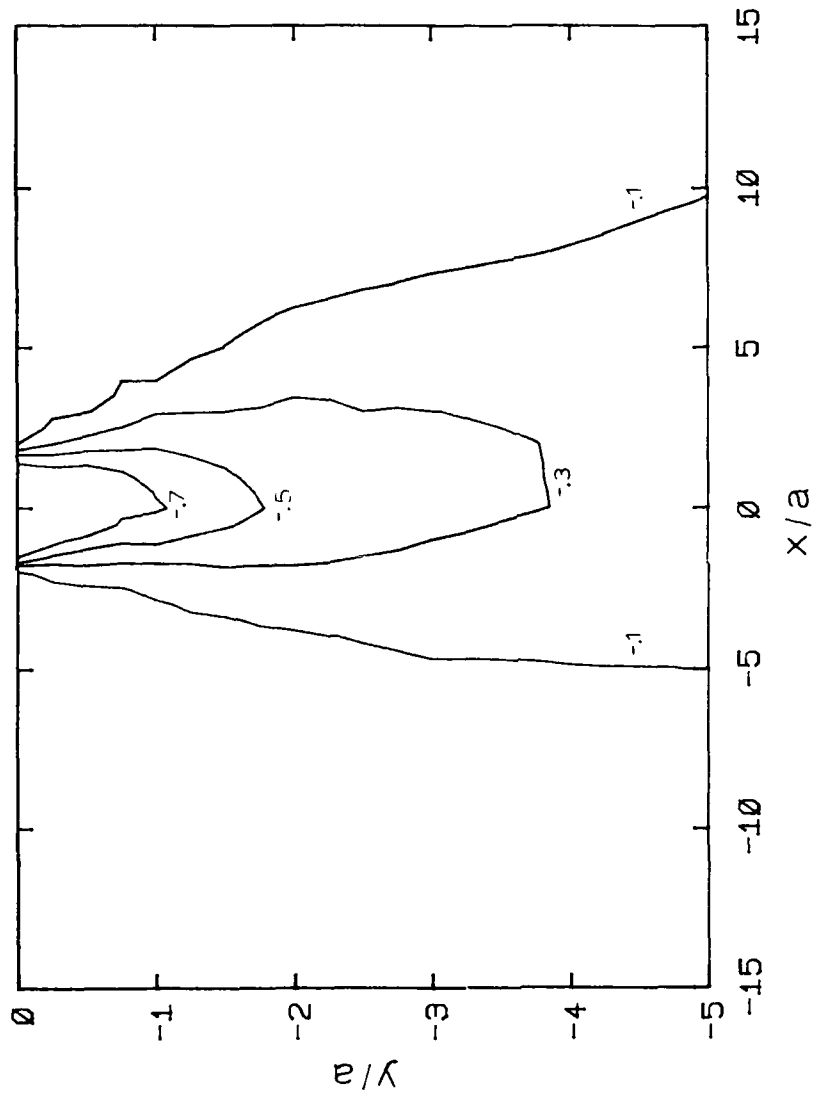


Figure D.4 The steady state σ_{yy} component of the state of stress at different depths normalized with respect to the maximum applied normal stress, p_o , for contact length, $a=20\mu\text{m}$, $\mu=.47$, $E_2/E_1=2.5$, and $d=.2\mu\text{m}$.

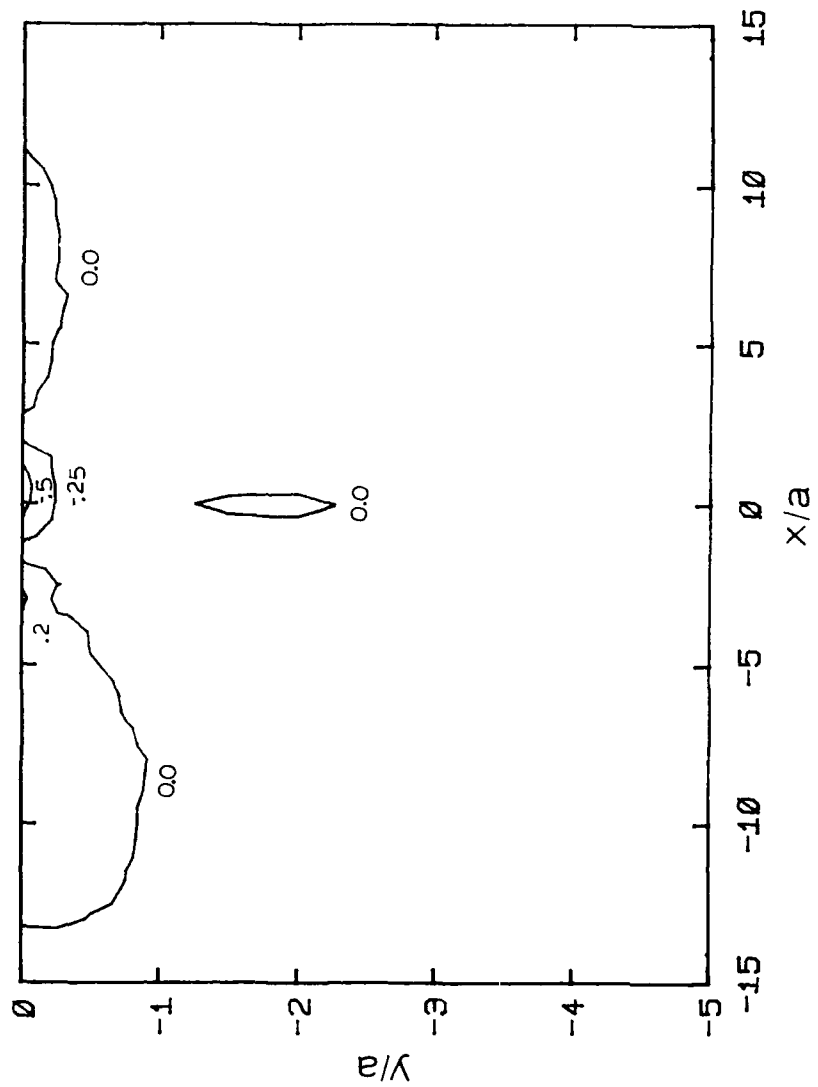


Figure D.5 The steady state σ_{xx} component of the state of stress at different depths normalized with respect to the maximum applied normal stress, p_0 , for $p=1/2p_0$, $a=20\mu\text{m}$, $\mu=1$, $E_1/E_2=2.5$, and $d=2\mu\text{m}$.

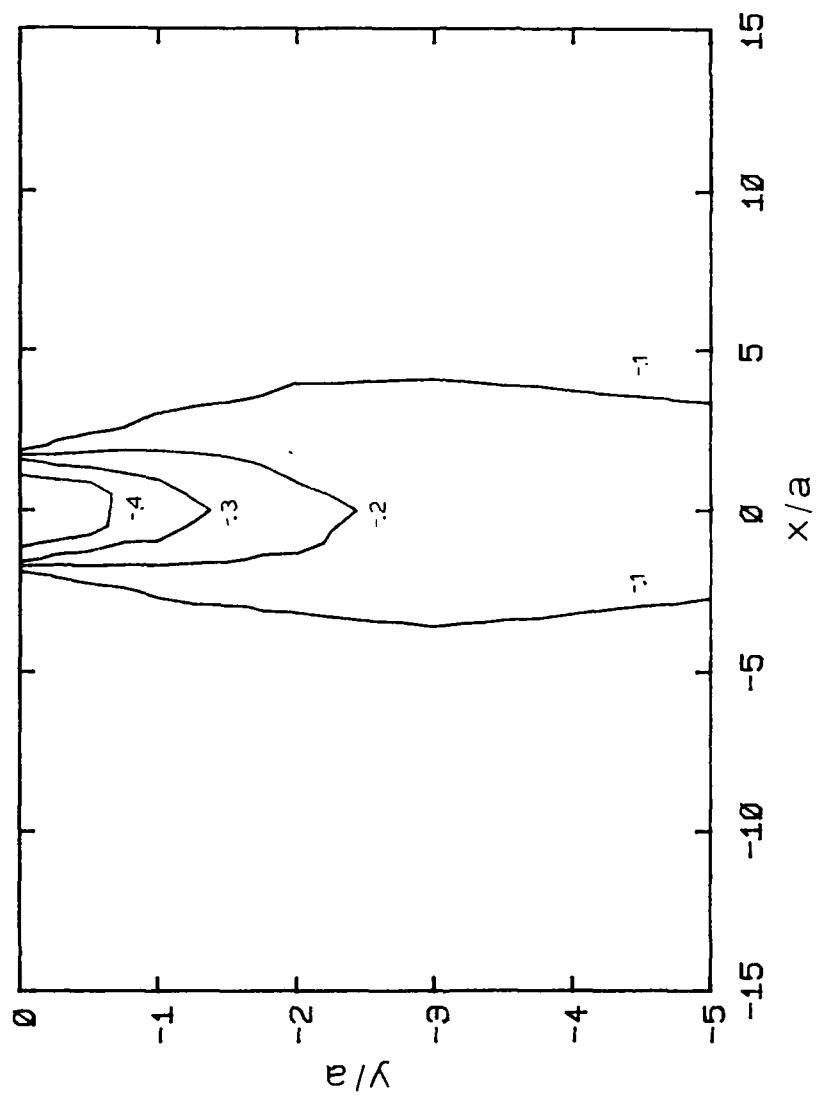


Figure D.6 The steady state σ_{yy} component of the state of stress at different depths normalized with respect to the maximum applied normal stress, p_0 , for $p=1/2p_0$, $a=20\mu\text{m}$, $\mu=.1$, $E_1/E_2=2.5$, and $d=.2\mu\text{m}$.

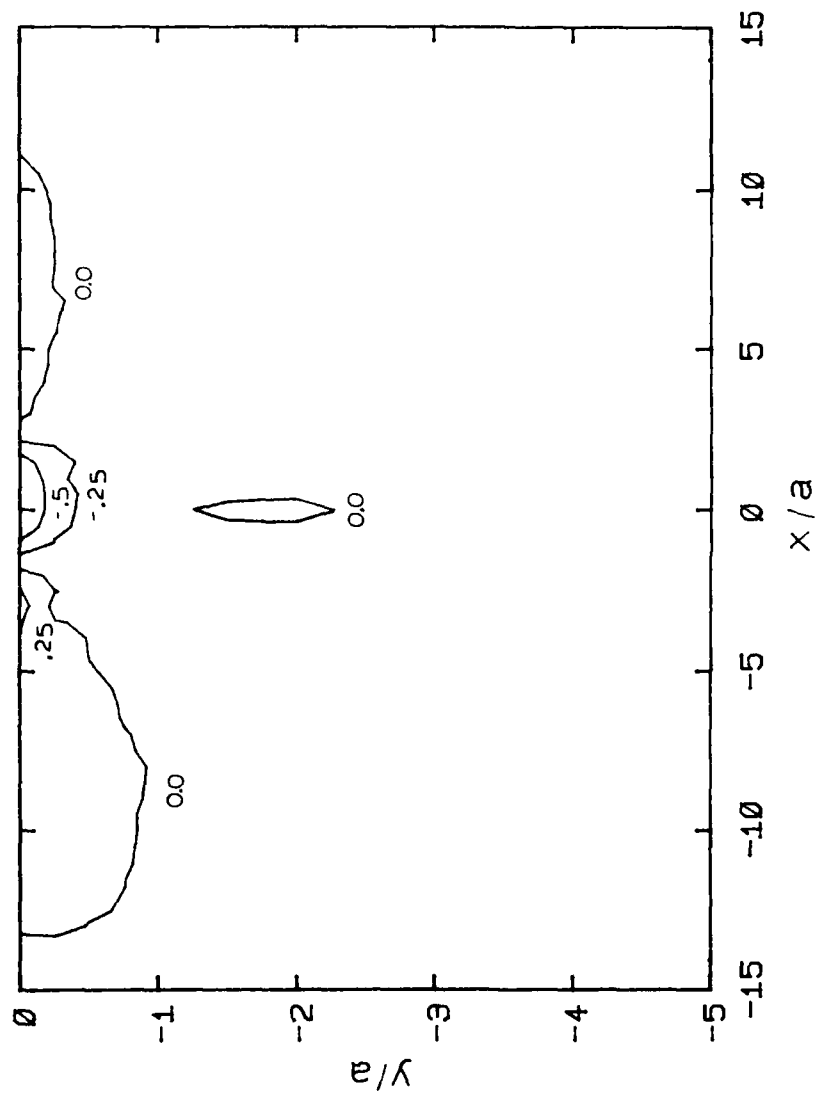


Figure D.7 The steady state σ_{xx} component of the state of stress at different depths normalized with respect to the maximum applied normal stress, p_0 , for $p=3/4p_0$, $a=20\mu\text{m}$, $\mu=1$, $E_1/E_2=2.5$, and $d=2\mu\text{m}$.

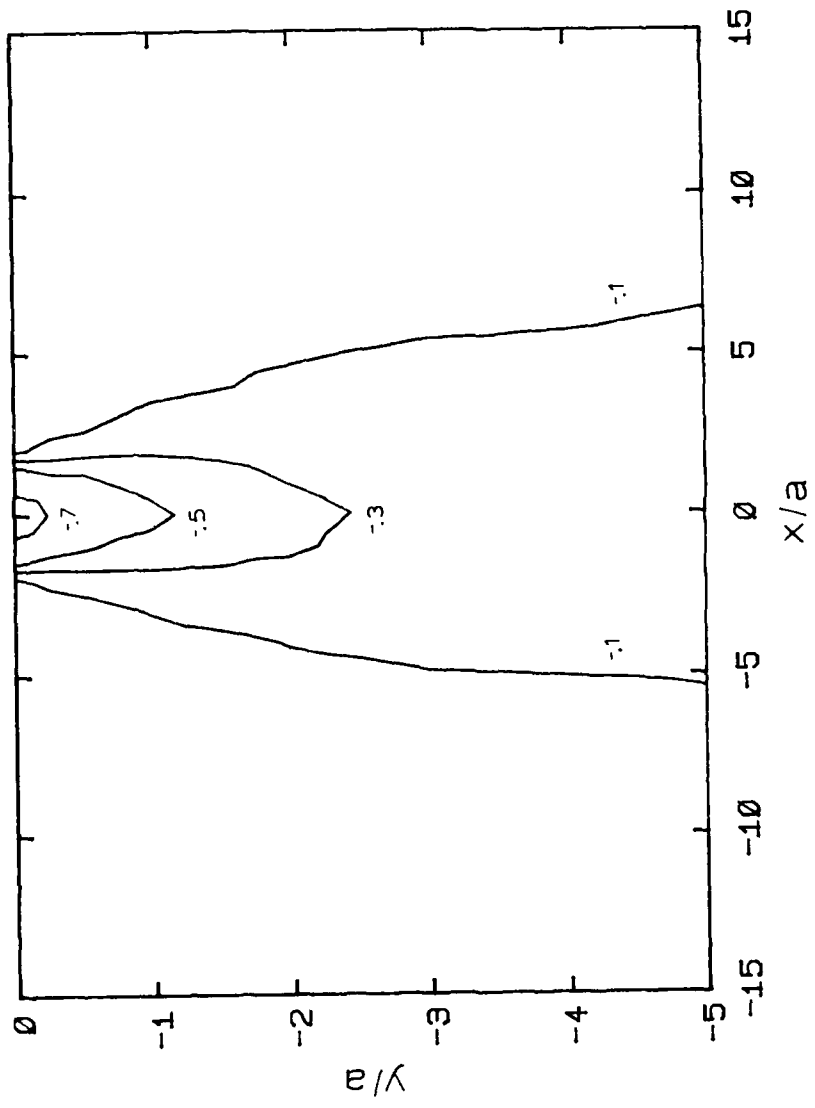


Figure D.8 The steady state σ_{yy} component of the state of stress at different depths normalized with respect to the maximum applied normal stress, p_0 , for $p=3/4p_0$, $a=20\mu\text{m}$, $\mu=1$, $E_1/E_2=2.5$, and $d=2\mu\text{m}$.

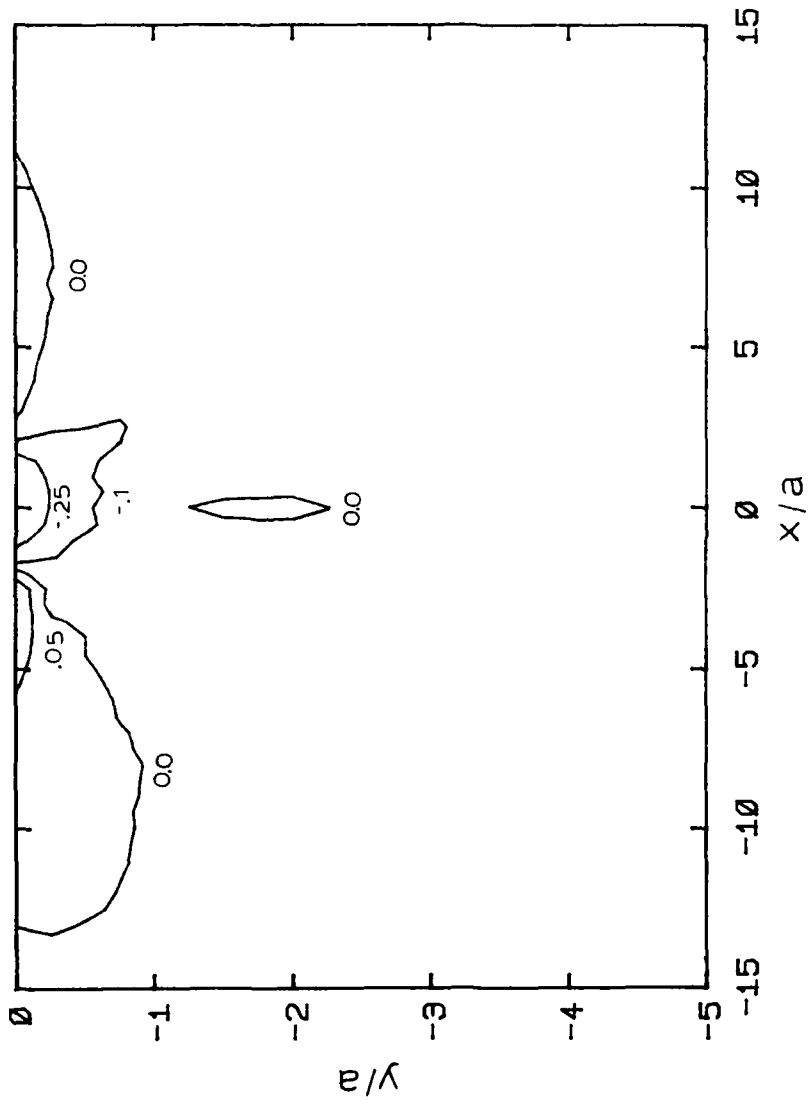


Figure D.9 The steady state σ_{xx} component of the state of stress at different depths normalized with respect to the maximum applied normal stress, P_0 , for $P = 1/2P_0$, $a = 20\mu\text{m}$, $\mu = .1$, and $E_1/E_2 = 1$.

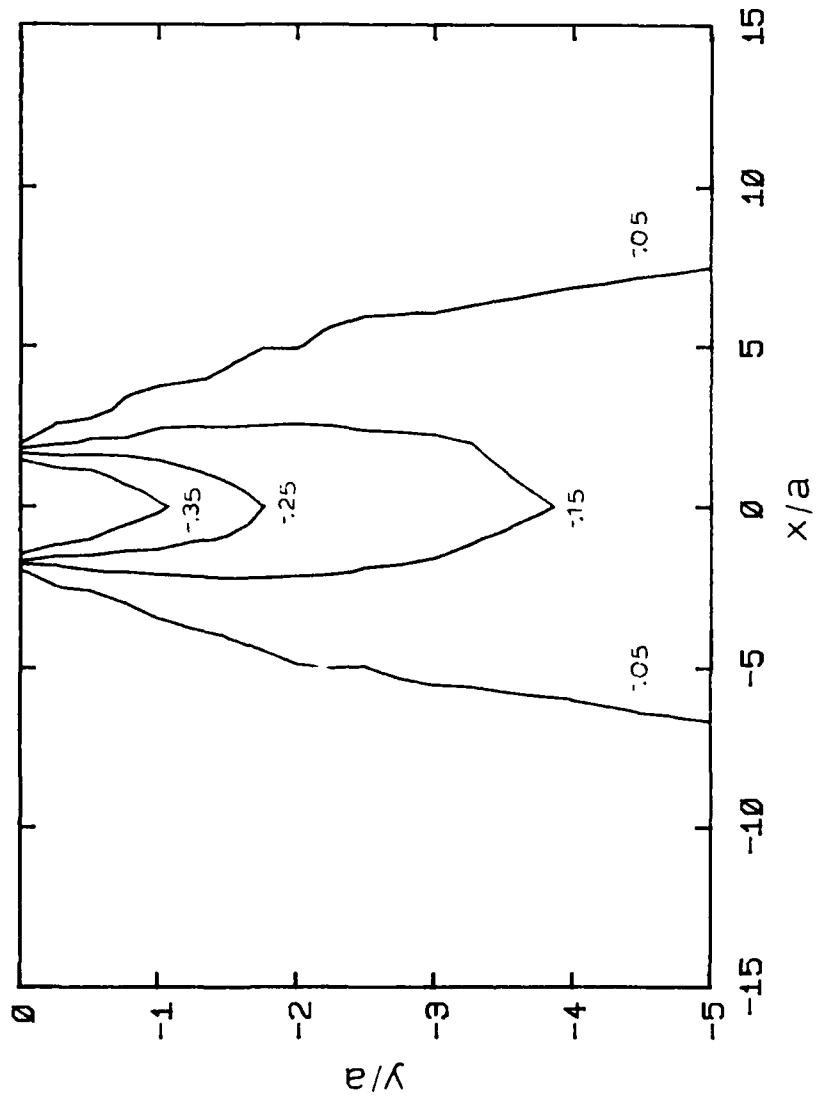


Figure D.10 The steady state σ_{yy} component of the state of stress at different depths normalized with respect to the maximum applied normal stress, p_o , for $p=1/2p_o$, $a=20\mu m$, $\mu=.1$, and $E_1/E_2=1$.

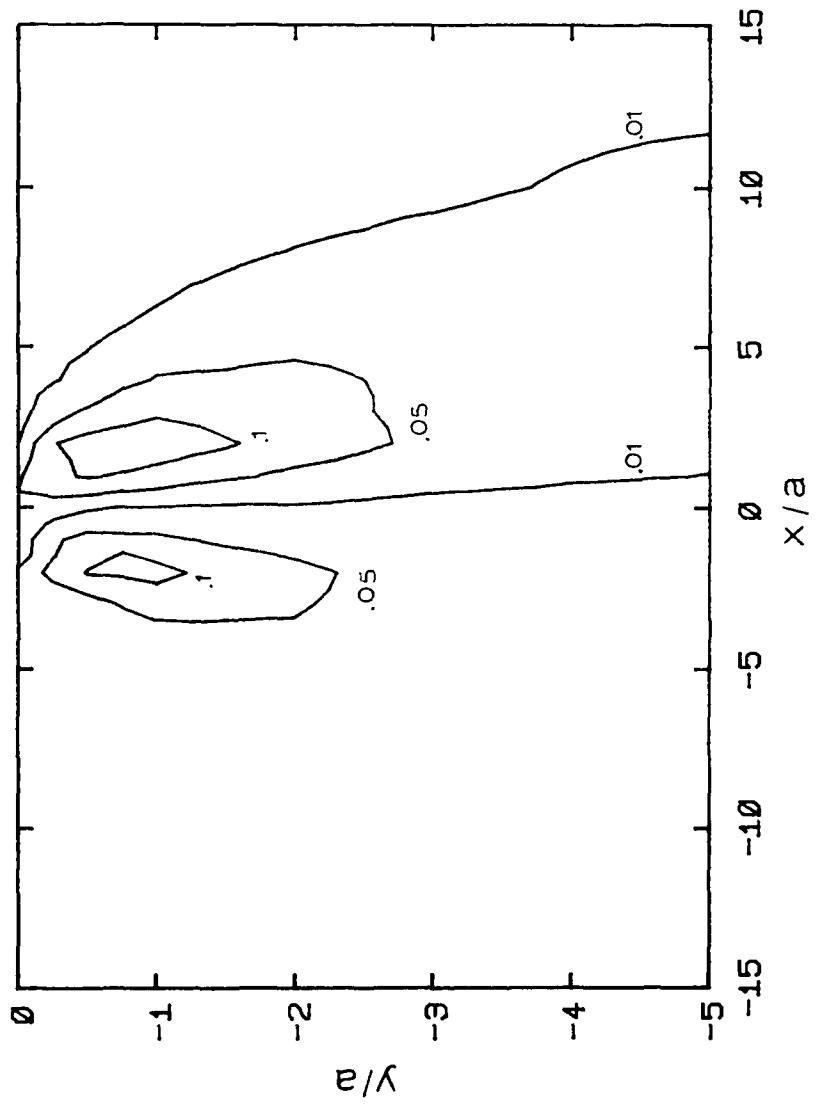


Figure D.11 The steady state τ_{xy} component of the state of stress at different depths normalized with respect to the maximum applied normal stress, p_0' , for $p=1/2p_0'$, $a=20\mu\text{m}$, $\mu=.1$, $E_1/E_2=1$.

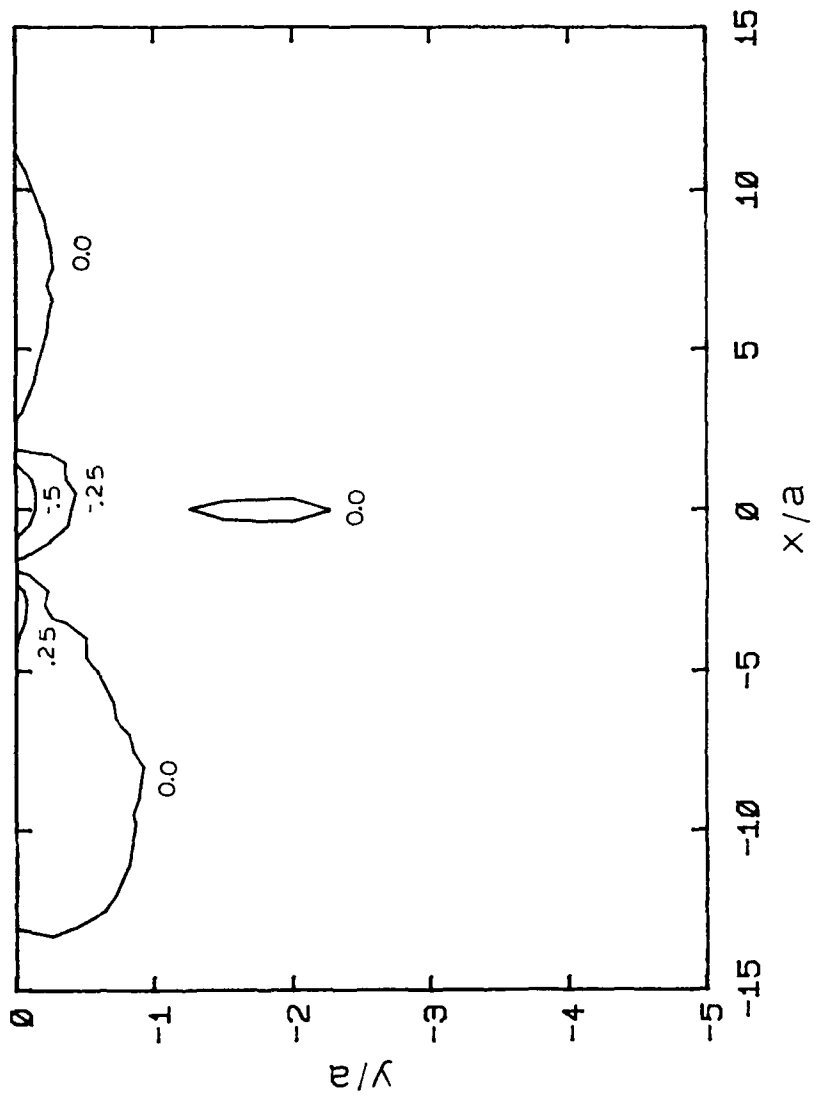


Figure D.12 The steady state σ_{xx} component of the state of stress at different depths normalized with respect to the maximum applied normal stress, p_o , for $p=3/4p_o$, $a=20\mu\text{m}$, $\mu=.1$, $E_1/E_2=1$.

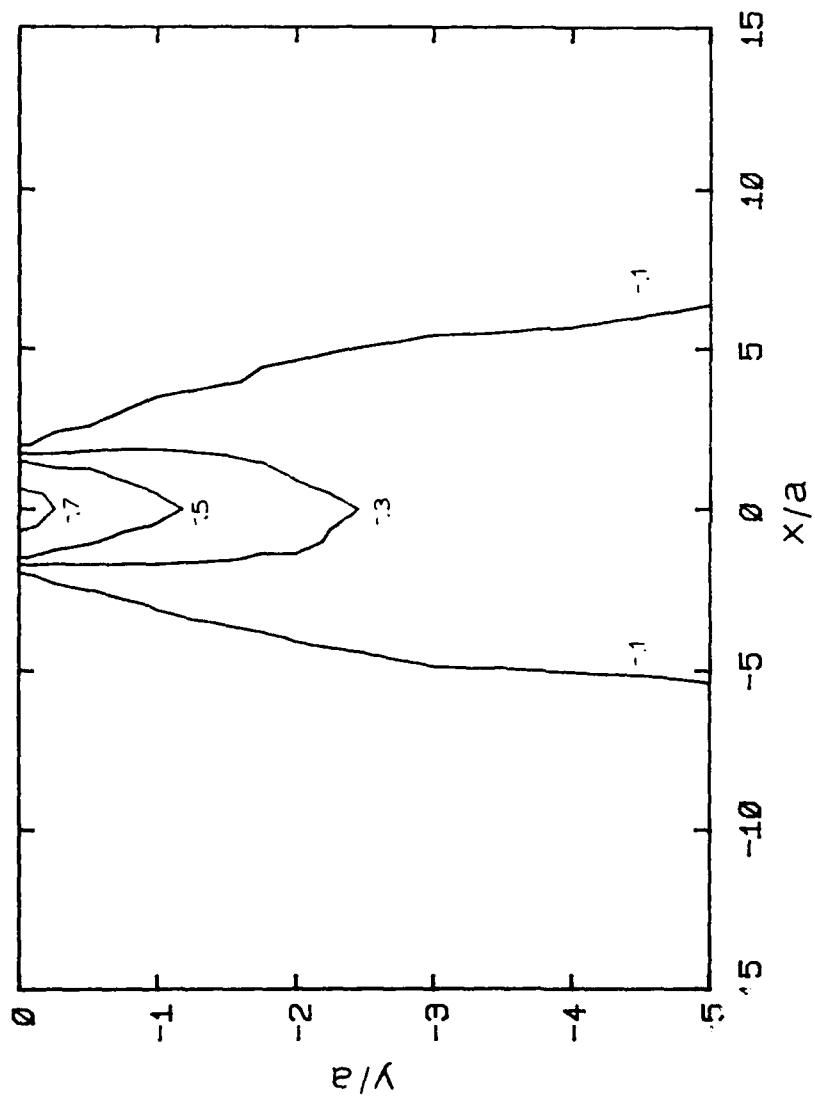


Figure D.13 The steady state σ_{xy} component of the state of stress at different depths normalized with respect to the maximum applied normal stress, p_0 , for $p=3/4p_0$, $a=20\mu m$, $\mu=0.1$, $E_1/E_2=1$.

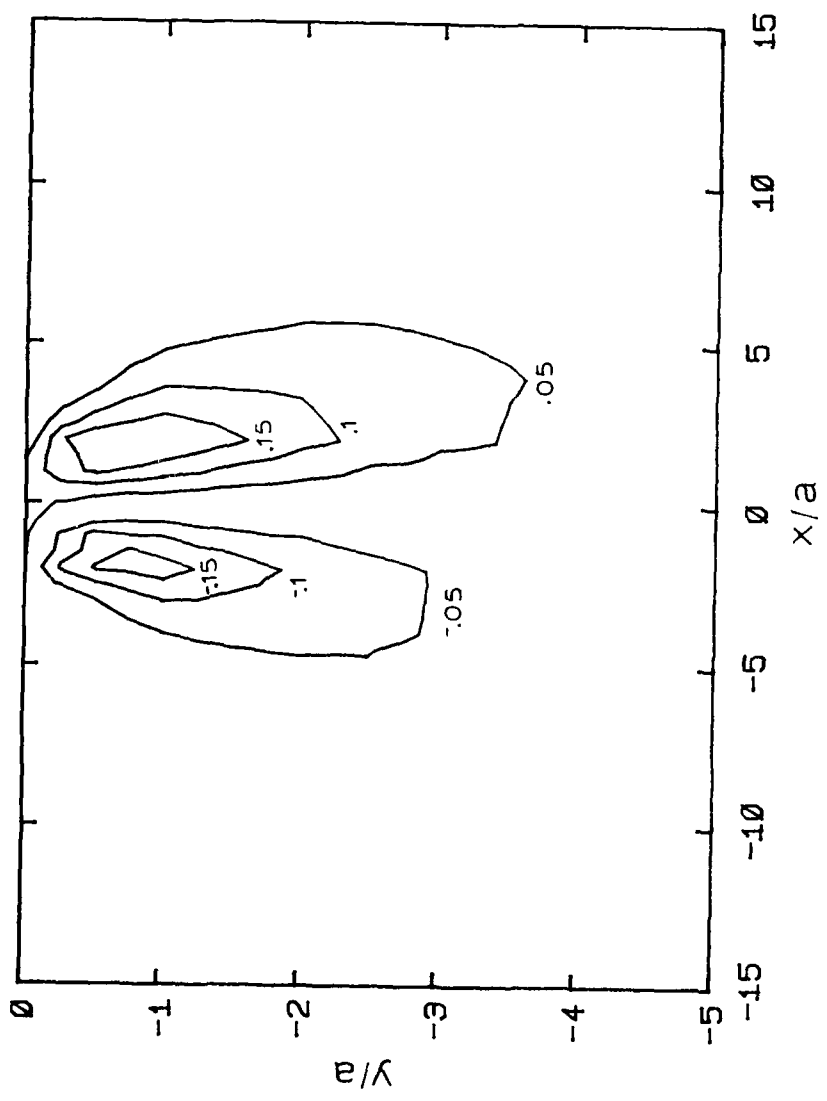


Figure D.14 The steady state τ_{xy} component of the state of stress at different depths normalized with respect to the maximum applied normal stress, p_o , for $p=3/4p_o$, $a=20\mu\text{m}$, $\mu=1$, $E_1/E_2=1$.

APPENDIX E: MICROGRAPHS OF WORN SURFACES

Micrographs of worn pins and disks of various implanted and unimplanted surfaces are illustrated in this appendix. They are supplementary to those found in Chapter 4.



Figure E.1 Typical wear scar on an Al^+ implanted iron pin after 5 cm of sliding on an Al^+ implanted iron disk. (lubricated test in air, load=400g)



Figure E.2 Typical wear scar on an unimplanted iron pin after 5 cm of sliding. (lubricated test in air, load=400g)



Figure E.3 Typical wear scar on a N^+ implanted iron pin.
(lubricated test in air, load=400g, 12,000 rev.)

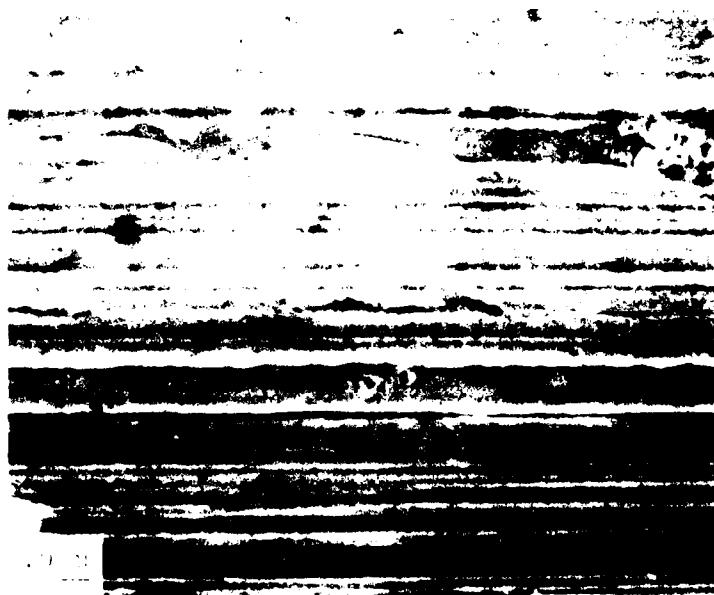


Figure E.4 Typical wear track on an unimplanted iron disk.
(lubricated test in air, load=400g, 12,000 rev.)

Distribution List

	<u>Number of Copies</u>
Aero Material Department Naval Air Development Center Warminster, PA 18974 Attn: Mr. M.J. Devine, Code 30-7	1
Air Force Aero Propulsion Laboratory Wright Patterson Air Force Base Dayton, OH 45433 Attn: Mr. C. Hudson	1
Air Force Materials Laboratory Wright Patterson Air Force Base Dayton, OH 45433 Attn: Mr. F. Brooks	1
Defense Documentation Center Building 5 Cameron Station Alexandria, VA 22314	12
National Bureau of Standards Department of Commerce Washington, D.C. 20234 Attn: Dr. A.W. Ruff	1
National Science Foundation Engineering Mechanics Division 1800 G Street Washington, D.C. Attn: Mr. M.S. Ojalvo	1
Naval Air Systems Command Washington, D.C. 20361 Attn: R. Schumaker, Code 340E	1
Director Naval Research Laboratory Washington, D.C. 20375 Attn: Technical Information Division Dr. L. Jarvis, Code 6170 Dr. R. Ravner	6
Naval Sea Systems Command Washington, D.C. 20362 Attn: Mr. M. Hoobchack	1
Naval Ship Research and Development Laboratory Annapolis, MD 21402 Attn: Mr. N. Glassman Attn: Dr. J. Dray	1 1

Office of Naval Research
800 N. Quincy Street
Arlington, VA 22217
Attn: Commander H.P. Martin, Code 470B 3

Office of Naval Research
800 N. Quincy Street
Arlington, VA 22217
Attn: Dr. R. Miller, Code 473 1

Mr. D. Anderson
Foxboro Analytical
P.O. Box 435
Burlington, MA 01803 1

Mr. N.L. Basdekas
Office of Naval Research
800 N. Quincy Street
Arlington, VA 22217 1

Mr. J.R. Belt, Code 28
David W. Taylor Naval Ship R&D Center
Annapolis, MD 21402 1

Dr. M.K. Bennett, Code 6176
Naval Research Laboratory
Washington, D.C. 20375 1

Dr. G. Bosmajian, Code 283
David W. Taylor Naval Ship R&D Center
Annapolis, MD 21402 1

Mr. M.A. Chaszeyka
Office of Naval Research - BRO
Chicago, IL 60605 1

Professor H.S. Cheng
Northwestern University
Dept. of Mechanical Engineering &
Aeronautical Sciences
Evanston, IL 60201 1

Mr. A. Conte Code 60612
Naval Air Development Center
Warminster, PA 18974 1

Mr. R.J. Craig, Code 2832
David W. Taylor Naval Ship R&D Center
Annapolis, MD 21402 1

Dr. J.F. Dill, Code SFL
Air Force Aero Propulsion Lab
Wright Patterson Air Force Base
Dayton, OH 45433 1

Mr. A.J. D'Orazio
Naval Air Propulsion Center
Trenton, NJ 08628 1

Dr. T. Dow
Battelle Columbus Lab
505 King Avenue
Columbus, OH 43201 1

Mr. E.C. Fitch
FPRC - Oklahoma State University
Stillwater, OK 74074 1

Dr. P. Genalis, Code 1720.1
David W. Taylor Naval Ship R&D Center
Bethesda, MD 20084 1

Dr. P.K. Gupta
Mechanical Technology Inc.
Latham, NY 12110 1

Mr. P.T. Heyl
Pratt & Whitney Aircraft
E. Hartford, CT 06108 1

Dr. D. Jewell, Code 1170
David W. Taylor Naval Ship R&D Center
Bethesda, MD 20084 1

Professor J.H. Johnson
Michigan Technical University
Houghton, MI 49931 1

Dr. J.P. King
Pennwalt Corp.
King of Prussia, PA 19406 1

Dr. M. Klinkhammer, Code 2832
David W. Taylor Naval Ship R&D Center
Annapolis, MD 21402 1

Mr. M. Kolobielski
U.S. Army MERADCOM
Ft. Belvoir, VA 22061 1

Dr. I.R. Kramer
David W. Taylor Naval Ship R&D Center
Annapolis, MD 21402 1

Mr. A.I. Krauter
Shaker Research Corp.
Ballston Lake, NY 12120 1

Capt. L. Krebes
AFOSR/NC
Bolling Air Force Base
Washington DC 20332

1

Mr. S.P. Lavelle
ROYCO Institute
62 Prospect St.
Waltham, MA 02154

1

Professor A.O. Lebeck
University of New Mexico
Mechanical Engineering Dept.
Albuquerque, NM 87131

1

Dr. M. Lee
General Electric Corp. Res. & Dev.
P.O. Box 8
Schenectady, NY 12301

1

Dr. L. Leonard
Franklin Research Center
20th & Race St.
Philadelphia, PA 19103

1

Mr. S.J. Leonardi
McBil R & D Corp.
Billingsport Rd.
Paulsboro, NJ 08066

1

Mr. W.E. Mayo
Rutgers College of Engineering
P.O. Box 909
Piscataway, NJ 08854

1

Dr. C.J. Montrose
Catholic University of America
Washington DC 20060

1

Dr. R.W. McQuaid, Code 2832
David W. Taylor Naval Ship R&D Center
Annapolis, MD 21402

1

Dr. P. Nannelli
Pennwalt Corp.
King of Prussia, PA 19406

1

Mr. A.B. Neild, Code 2723
David W. Taylor Naval Ship R&D Center
Annapolis, MD 21402

1

Mr. R.N. Pangborn
Rutgers College of Engineering
P.O. Box 909
Piscataway NJ 08854 1

Mr. M.B. Peterson
Wear Sciences Inc.
925 Mallard
Arnold, MD 21012 1

Professor E. Rabinowicz
Room 35-014
Massachusetts Institute of Technology
77 Massachusetts Avenue
Cambridge, MA 02139 1

Professor D. Rigney
Metallurgical Engineering Department
Ohio State University
Columbus, OH 43210 1

Mr. F.G. Rounds
General Motors Research Labs
F & L Dept.
12 Mile & Mound Road
Warren, MI 48090 1

Mr. W. Rosenlied
SKF Industries Inc.
King of Prussia, PA 19406 1

Dr. N. Saka
Room 35-014
Massachusetts Institute of Technology
77 Massachusetts Avenue
Cambridge, MA 02139 1

Professor N.P. Suh
Room 35-136
Massachusetts Institute of Technology
77 Massachusetts Avenue
Cambridge, MA 02134 1

Dr. J. Tichy
Rensselaer Polytechnical Institute
Troy, NY 12181 1

Dr. R. Valori
Naval Air Propulsion Center
Trenton, NJ 08628 1

Mr. V.D. Wedeven
NASA/ Lewis Research Center
Cleveland, OH 44135

1

Mr. P. Weinberg
Naval Air Systems Command
Washington DC 20361

1

Professor D. Wilsdorf
School of Engineering & Applied Science
University of Virginia
Charlottesville, VA 22903

Mr. A.D. Woods, Code 5243
Naval Sea Systems Command
Washington DC 20360

1

Dr. C.C. Wu, Code 6368
Naval Research Laboratory
Washington DC 20375

1

Mr. R. Lee
Joint Oil Analysis Program
Technical Support Center
Bldg. 780
Naval Air Station
Pensacola, FL 32508

1